



Fermilab

Fermi National Accelerator Laboratory
P.O. Box 500 • Batavia, Illinois • 60510

FERMILAB LINAC UPGRADE

CONCEPTUAL DESIGN

REVISION 3

JULY, 1989

OPERATED BY UNIVERSITIES RESEARCH ASSOCIATION, INC.
FOR THE UNITED STATES DEPARTMENT OF ENERGY

Fermilab Linac Upgrade

Table of Contents

1.	Introduction.....	1
2.	Impact of a 400-MeV Linac on Booster Performance.....	3
3.	The Linac Upgrade.....	7
3.1	Accelerating Structure.....	7
3.1.1	Structure Choice.....	7
3.1.2	Design Assumptions and Criteria.....	9
3.1.3	Segmentation of the Structure.....	15
3.1.3.1	Accelerating Modules.....	15
3.1.3.2	Bridge Coupler.....	16
3.1.3.3	Coupling Constant.....	19
3.1.4	Transverse Focusing.....	20
3.1.4.1	Lattice Design.....	20
3.1.4.2	Quadrupole Design.....	22
3.1.5	Transition Section.....	23
3.1.6	Prototype Accelerating Module.....	27
3.2	Radio Frequency Power System.....	28
3.2.1	Power Requirements.....	28
3.2.2	Rf Modulator.....	29
3.2.3	System Regulation.....	30
3.2.4	Amplitude and Phase Control.....	31
3.2.5	Prototype 12 MW RF System.....	33
3.3	Mechanical Systems.....	35
3.3.1	Construction and Tuning of Side-Coupled Structures.....	35
3.3.2	Temperature Regulation.....	38
3.3.3	Vacuum System.....	40
3.3.4	Support and Alignment.....	40
3.4	Linac Diagnostics and Control System.....	41
3.4.1	Momentum Measurement.....	41
3.4.2	Beam Steering.....	42
3.4.3	Beam Envelope Measurement.....	44
3.4.4	Transverse Emittance.....	44
3.4.5	Longitudinal Emittance.....	45
3.4.6	Delta-t Measurement.....	46
3.4.7	Linac Control System.....	46
3.5	Transfer and Injection to the Booster.....	47
3.5.1	Transfer Line.....	47
3.5.1.1	Technical Problems for the 400-MeV Upgrade.....	47
3.5.1.2	Magnets.....	49
3.5.1.3	Chopper and Septum.....	50
3.5.1.4	Transfer Line Optics.....	51
3.5.1.5	Transfer Line Diagnostics.....	52
3.5.2	Debuncher for Booster Injection.....	52
3.5.3	Injection into the Booster.....	53
3.5.3.1	Injection Septum and Orbumps.....	53

3.5.3.2	H ⁻ Stripping Foil.....	54
3.5.3.3	Injection Diagnostics.....	54
3.6	Installation and Commissioning.....	55
3.7	Conventional Construction.....	58
Appendix A	- Linac Schedule.....	63
Appendix B	- Linac Cost Estimate.....	65
Figures		

Fermilab Linac Upgrade

1. Introduction

The goal of the Tevatron Collider Upgrade program is to improve the Collider luminosity and the fixed-target intensity. The Linac portion of this project will increase the energy of the existing 200-MeV linac to 400 MeV in order to reduce beam emittance degradation in the Booster.

The critical parameters which limit the luminosity of the Tevatron Collider are the beam emittances, both longitudinal and transverse, at each stage in the acceleration sequence. Critical limitations occur because the beam emittance grows significantly during the first few milliseconds after injection into the Booster, during acceleration through transition in the Booster, at injection into the Main Ring, during acceleration through transition in the Main Ring, during rf bunch manipulation in the Main Ring, and finally, during injection into the Tevatron. Improvements are underway to significantly reduce the emittance growth which occurs in the Booster at transition and in all stages of Main Ring operation. The suspected cause of the emittance growth during the first few milliseconds after injection into the Booster is the tune spread caused by space charge and small errors in the magnetic guide field. The most practical way to eliminate this growth is to increase the energy of the Linac, thereby reducing the tune spread due to space charge. The increase in energy will not only help provide a smaller emittance beam for Collider operation, it will help provide higher intensity beams for fixed target operation.

By increasing the Linac energy from 200 MeV to 400 MeV, the phase space density limitation (defined by the ratio of the number of particles to the beam emittance) a few milliseconds after injection into the Booster can be increased by about $1 \frac{3}{4}$ times. Since the initial beam emittance will be smaller, the beam size will be smaller, and the effects of nonlinear field errors on emittance growth will be smaller. Further, at the higher magnetic guide field needed at 400 MeV, the strengths of the remnant and eddy current field errors will be proportionately smaller. The rf capture of the

injected beam will be improved because of the larger ratio of available bucket area to beam phase space area. These factors will make possible a more intense beam with a smaller emittance. A more detailed discussion of the effect of the Linac Upgrade on Booster performance appears in Section 2.

The Fermilab 200-MeV linac was designed in the late 1960's. A number of advances in linac technology have been made since that time including the ability to achieve higher accelerating gradients. In addition, more efficient rf power sources are available. (A particular difficulty of the present drift-tube linac operating at a frequency of 200 MHz is the availability of the final power amplifier tube which is obsolete. Replacements must be obtained by rebuilding tubes that have already failed in service.) The question of changing from the Alvarez drift-tube structure to a more efficient structure above 100 MeV was discussed at the time of construction of the Fermilab linac. For the sake of replication of components and simplicity, it was decided to continue the drift-tube structure to 200 MeV even though the side-coupled structure was known to be more efficient at higher energies. It seems reasonable now to consider replacing the higher energy cavities with more efficient accelerating structures operating at a higher gradient and thus increase the energy of the linac in the same available building space.

R and D, not related to this project, is currently underway to understand the growth in beam emittance that occurs between the ion source and the entrance to the linac. It is possible that this R and D will result in system improvements, such as the addition of a radio-frequency quadrupole (RFQ) structure between the ion source and the linac. The benefits of improving the beam quality at low energy in the system will allow the transition to a new structure at higher energy to be made more easily but will not change the design proposed in this report.

The Linac upgrade project provides for the replacement of the last four Linac drift-tube tanks with more efficient cavities having a higher accelerating gradient. These tanks, which accelerate from 116 MeV to 200 MeV, will be replaced with seven side-coupled cavity modules operating at a frequency of 805 MHz, four times the operating frequency of the present Linac structure. The higher frequency side-

coupled cavity structure is physically smaller, is constructed of single cells brazed together in a structure capable of high vacuum, and can be operated reliably at much higher accelerating gradients, i.e., 8 MV/m compared to 2.5 MV/m in the drift-tube structure. These seven side-coupled cavity modules, installed in the space made available by replacing the four drift-tube tanks and driven by seven 12 MW, 805 MHz klystron rf power supplies, will accelerate the beam from 116 MeV to 400 MeV. In addition, a special matching section will be added between the drift-tube and side coupled cavity structures to allow a proper match between these different Linac structures. The present injection and transport line to the Booster accelerator will be modified by replacing a few elements to accommodate the higher energy. A complete discussion of these aspects of the Linac Upgrade appears in Section 3.

2. Impact of a 400-MeV Linac on Booster Performance

With the advent of the proton-antiproton collider at Fermilab a change has taken place in the criteria by which performance of the Booster and Main Ring accelerators are judged. For both collider and fixed target operation the normal figure of merit is the luminosity, which is the proportionality constant between the interaction rate observed by an experimenter and the cross section for a particular process. In the collider mode of operation, luminosity depends directly on the density of particles (i.e. particles per unit transverse phase space area) circulating in the Tevatron, while for fixed target physics the luminosity depends only on the total number of particles extracted from the Tevatron. Thus in the collider era Booster performance is no longer judged simply by how many protons can be accelerated, but by what density of particles can be delivered. This distinction is important because it determines the strategy followed in attempting to upgrade the Booster performance. As we will show below, we have evidence that the beam density in the Booster is limited by incoherent space-charge effects at injection, while the total beam intensity is limited by the combination of space-charge and aperture. As we will further discuss below, the fundamental space-charge limitation can best be dealt with by raising the Booster injection energy.

Current Booster performance is summarized in Figures 1 and 2. The figures are based on measurements completed during the August 1986 startup and following the spring, 1987, Collider run. In Figure 1 the total amount of beam which can be accelerated in the Booster is plotted as a function of the number of injected turns. The Booster uses a multiple turn injection scheme in which H^- ions coming out of the Linac are stripped to form H^+ by passing through a thin foil. This injection procedure allows us to run up to 3.5×10^{12} particles in the Booster while only using 5×10^{11} particles per injected turn from the Linac (operating at 30mA). We see from Figure 1 that at low-to-moderate intensities the number of protons accelerated in the Booster increases almost linearly with the number of injected turns, while at high intensities it becomes impossible to accelerate more than about 3.5×10^{12} protons, independent of the number of injected particles.

An understanding of this limitation can be gained by looking at Figure 2 where we have plotted the normalized transverse emittance of the extracted Booster beam (i.e. the beam size) as a function of the number of protons accelerated. In the figure we have displayed both the vertical and horizontal emittances.* In principle, we might expect to be able to increase the phase space density of the beam to an arbitrarily large value because the multiple turn H^- injection allows us to lay subsequent turns exactly on top of each other. Figure 2 shows that this is not so. At low intensities, up to about 1.2×10^{12} , the extracted beam size is independent of the number of protons, that is the phase space density is increasing with the number of injected turns. However, at higher intensities the beam size starts to grow following the dashed line on the figure. The dashed curve is close to a contour of constant phase space density. It says that we are not able to achieve a density of more than $1.7 \times 10^{12} / 10\pi$ mm-mr total or $2.0 \times 10^{10} / 10\pi$ mm-mr/bunch in the Booster. This is about a factor of two lower than that proposed for the Collider Upgrade.

* The momentum spread in the beam is also displayed. Momentum spread and horizontal transverse emittance have been separately determined through measurements taken at points with similar beta functions but different dispersions.

The two figures present a self-consistent picture of what is going on in the present Booster: The Booster beam size is just what is delivered from the Linac as long as this does not produce a density higher than the limit cited above. At higher intensities the beam size blows up in such a way as to keep the phase space density at the prescribed limit. The limit on the total amount of beam which can be accelerated is reached when the beam size gets big enough to fill the available aperture.

As stated earlier we believe the observed limit on the charge density that can be produced in the Booster arises from the incoherent space-charge tune shift at injection. The physical mechanism is as follows: A proton located within a bunch in the Booster is subject to both electric and magnetic forces due to other protons within the same bunch. Since these forces depend on the transverse position of the proton, they provide additional focusing which changes the tune of a particle in a manner which depends on its oscillation amplitude. As a result an incoherent tune spread is introduced in the beam whose magnitude is given by¹

$$\Delta\nu_{s.c.} = \frac{3r_p N_t}{2B\beta\gamma^2\epsilon_N} \quad (1)$$

where r_p is the classical radius of the proton, N_t is the total number of particles in the accelerator, B is the ratio of average to peak current, β and γ are the usual kinematic factors, and ϵ_N is the normalized (95%) transverse emittance.** The kinematic dependence on β and γ arises because the electric and magnetic field contributions exactly cancel as β goes to 1. The strong kinematic dependence insures that in any accelerator complex the total tune spread within the beam is apt to be largest at injection into the lowest energy ring. The mechanism by which the incoherent tune spread limits beam intensity is presumably the restriction of tunes to lie in a resonance free region. One would expect that the best one could possibly hope to do would be to run with a space-charge tune spread of 0.5. In practice one might expect to be even more restricted. Examination of the above expression shows that for fixed kinematics the tune spread is

** The formula is modified slightly if horizontal and vertical emittances are unequal and/or the momentum spread is non-zero.

proportional to the phase space density of the beam. The dashed lines shown in Figure 2 represent contours of constant space-charge tune spread ($\Delta\nu_{s.c.} = 0.38$). We believe that the above described mechanism is providing a fundamental limit on the beam density which we can achieve in the Booster. Two additional observations lend further credence to this hypothesis. First, we have looked at beam profiles throughout the Booster acceleration cycle and have found that to within our measurement resolution (1.5msec) the blowup seen at high intensity occurs at injection. Second, we have observed incoherent resonance lines early in the acceleration cycle and have seen them broaden as the beam intensity is raised. These observations are in qualitative agreement with what we expect from the above described mechanism.

Given that we believe that the incoherent space-charge tune spread is providing the fundamental limit on the achievable beam density in the Booster, it is clear from the space-charge tune spread formula that the only good way to raise the phase space density of the beam delivered out of the Booster is to raise the injection energy. The only other options available, other than building a ring with a smaller circumference, are to increase the bunching factor during the initial stages of acceleration or to correct enough resonances to allow one to approach space-charge tune spreads of 0.5. Although we are currently experimenting with both of these options, it is unlikely that gains of greater than 10-20% can be achieved in these ways. Increasing the Linac energy from 200 MeV to 400 MeV increases the kinematic factor, $\beta\gamma^2$, in the denominator of (1) from .83 to 1.45. This will raise the fundamental limitation on the Booster phase space density by about 75% (Figure 3).

Below we summarize the expected benefits to the Booster of raising the injected beam energy to 400 MeV, including several effects not included in the above discussion.

1. Increase the achievable phase space density. The achievable phase space density should increase from about 2.0 to about $3.5 \times 10^{10} / 10\pi$ mm-mr/bunch.
2. Increase the total amount of beam deliverable. The effective aperture of the Booster will increase by about 50% in normalized

units due to increased adiabatic damping in the linac. Combined with the increased phase space density achievable this, in principle, would allow one to increase the total amount of beam delivered by a factor of 2.6. We don't really expect this to happen because we would expect the increase to be accompanied by other instabilities and difficulties in transmission of the larger beam current in the Main Ring. An increase in total delivered beam of 50%-75% is perhaps reasonable to expect in the long run however.

3. Better field quality at Booster injection. This will come about for two reasons. First, the higher injection fields will reduce the effects of remnant fields in the Booster magnets. And second, the smaller beam size out of the Linac will result in the beam being spread over a region of more uniform field than it is at present. It is hard to quantify the expected benefit from this effect.
4. Improved RF capture. The higher injection energy will result in a larger bucket area during the initial stages of acceleration as well as reducing the frequency swing during the acceleration cycle by about one third. This benefit is also hard to quantify.

3. The Linac Upgrade

3.1 Accelerating Structure

3.1.1 Structure Choice

The side-coupled accelerating structure (SCS) has been selected for the region above $\beta=0.456$ (116 MeV). The SCS was developed in the early 1960's for use on the LAMPF accelerator where a transition from the drift-tube structure to the SCS was made at 100 MeV. Since then the SCS has been used in many industrial and medical applications for electron and x-ray beams, on the LANL free electron laser for high intensity pulsed electron beams, and as the accelerating section in the racetrack microtrons at the NBS and the University of Illinois.

Other types of accelerating structures (Fig. 4) could be considered and some of these have been studied for use in the

LANL/NBS racetrack microtron.² SUPERFISH computer runs have been made for the disk and washer (DAW), annular-ring coupled structure (ACS), on-axis coupled structure (OAC), side-coupled structure (SCS), and the coaxial-coupled structure (CCS) at $\beta=.456$ (116 MeV). The particular properties considered for the upgrade application, included: (1) a high efficiency (high value of the shunt impedance ZT^2 , where Z is the ratio of the square of the accelerating field to the rf power dissipated per length in the structure, and T is the transit time factor) to minimize rf power consumption, (2) an ability to support high accelerating fields, (3) a mode spectrum without interfering modes close to the fundamental accelerating mode in the structure, (4) good cell-to-cell coupling to ensure good stability with long assemblies of many cells, and (5) good mechanical properties to allow simple fabrication, simplified tuning, and good pumping speed for high vacuum. Table 1 summarizes these preliminary results.

Table 1

Comparison of Shunt Impedance (ZT^2)
for Various Linac Structures
(at $\beta=.456$, KE=116 MeV)

Structure	ZT^2 (M Ω /m)	Remarks
DAW	38	Coupling 30-40%, good vacuum properties, most interfering modes
SCS	36	Good vacuum, satisfactory tuning, coupling typically a few % (<10%)
ACS	36	Poor vacuum, difficult tuning, good coupling. Dipole interfering mode
OAC	25	Poor vacuum, difficult tuning, moderate coupling
CCS	25	Poor vacuum, difficult tuning, good coupling

The DAW structure has been used for the higher energy (100 to 600 MeV) accelerating cavities in the Institute of Nuclear Research meson factory at the USSR Academy of Sciences, Moscow.³ There was

also a design for a DAW accelerating structure for a racetrack microtron.⁴ This USSR work has directly confronted the problem of interfering modes which has discouraged the use of the DAW structure in this country. The DAW structure has been considered also for accelerating cavities in the TRISTAN accelerator at the National Laboratory for High Energy Physics, KEK, Japan.⁵ The outstanding features of the DAW structure are the high efficiency for rf acceleration, the high stability resulting from the large coupling between cells, and good vacuum properties.

The option of using a DAW accelerating structure showed promise and was one of the principal focuses of our research and development program.⁶ It has been dropped from consideration for the Fermilab Upgrade on the basis of model tests which have shown the need for more development effort on both the mode spectrum and mechanical design than seems warranted for the project. At the present time the SCS is well understood and fully proven. From the LANL experience in the construction and operation of LAMPF and the NBS Microtron, we have available the information to give us confidence that our performance goals can be met. Cost estimates are based on the LANL experience with the SCS. The following reference design employs a SCS derived from that used for the LAMPF linac.

3.1.2 Design Assumptions and Criteria

Because the 400-MeV linac is to replace that part of the existing 200 MHz drift-tube linac which accelerates from 116.54 to 200 MeV, it must have a high gradient and make conservative use of space for matching, focusing, mechanical systems, etc. The 67 meters made available by removing the last four 200 MHz tanks must accommodate a transition section for matching the old and new accelerators, the 400-MeV linac itself, and about 2 m at the downstream end for changes to the Linac-to-Booster transport line. The other major design goals are to minimize power consumption and to keep all parameters within a range favoring dependable routine operation. Table 2 summarizes the principal design criteria and parameters.

Initial kinetic energy (T_i)	116.54	MeV
Final kinetic energy (T_f)	401.56	MeV
Length, including transition section	64.300	m
Frequency of rf (f)	805.0	MHz
Beam current averaged over pulse (\bar{I}_b)	50.	mA
Beam pulse length	< 100.	μ s
Repetition rate	15.0	Hz
Accelerating phase (φ_s)	-32.	deg
Average axial field (E_o)	8.04-7.07	MV/m
Maximum surface field (E_{max})	37.1	MV/m
Kilpatrick limit (E_K)	26.	MV/m
Number of modules	7	
RF power/module, typical	< 12.	MW
copper loss	7.1	MW
beam power	2.0	MW
reserve and control	2.9	MW
Number of sections/module	4	
Number of rf cells/section	16	
Total number of rf cells ($7 \times 4 \times 16$)	448	
Length of bridge couplers between sections	$\frac{3}{2}\beta\lambda$	
Transverse focusing scheme	FODO	
Transverse phase advance/FODO cell, average	79.	deg
Quadrupole magnetic length	7.0	cm
Quadrupole poletip field	5.26	kG
Quadrupole bore radius (r_q)	2.0	cm
Cavity bore radius (r_b)	1.5	cm

Table 2: Design Criteria and General Parameters for the 400 MeV SC Linac

Purely from the standpoint of gradient, power economy, power sources, etc. the choice of 805 MHz for the 400-MeV linac is toward the low frequency side of a broad optimum. However, the longitudinal emittance of the beam from the 200 MHz linac is large enough that a larger frequency ratio between structures risks degrading the performance by nonlinearity of the phase-energy oscillations (Section 3.1.5).

In a standing wave linac, the accelerating electric field seen by a synchronous particle is

$$E_z = E_0(z) \cos(\omega t + \phi_s) = E_0(z) \cos(\omega z/v_s + \phi_s), \quad (2)$$

where $E_0(z)$ is the field amplitude, v_s is the synchronous velocity and ϕ_s is the synchronous phase. The energy gain per unit cell length by a synchronous particle is

$$\Delta W/L = eE_0 T \cos \phi_s, \quad (3)$$

where

$$E_0 = \int_{-L/2}^{L/2} E_0(z) dz / L \quad (4)$$

is the average axial accelerating field, and

$$T = \int_{-L/2}^{L/2} E_0(z) \cos(2\pi z/L) dz / E_0 L \quad (5)$$

is the transit time factor which takes into account the temporal variation in the standing wave field as a synchronous particle crosses a cell.

To accelerate the H^- beam from 116 MeV to 400 MeV in the same length as the last four drift-tube tanks requires an average axial field E_0 of approximately 8 MV/m which is more than three times the average axial field used in the tanks to be replaced. This field is higher than used in any existing proton or H^- linac. However, to put this value in perspective requires a criterion for judging high fields. An examination of the constraints of conditioning times, x-ray levels and spark rates suggests that this is an achievable operating gradient at 805 MHz.⁷ Since no comprehensive study of maximum operating gradients exists in the literature, only power tests can ultimately determine if reliable operation is possible at this gradient. These three constraints are being experimentally studied using a special SC power test model (Figures 5 and 6).

Long conditioning times to reach a final operating gradient are unacceptable for an injector on which downstream accelerators rely. Conditioning times seem to be very dependent on vacuum and cavity surface conditions which differ greatly from one accelerator to another. The constraints of x-ray levels and spark rates on the operating gradient are only slightly better understood than conditioning times.

Historically, surface breakdown fields under cw conditions have been estimated with the empirical Kilpatrick criterion, established when untrapped oil diffusion vacuum pumps were used.⁸ The criterion can be written in the form

$$f = 1.643 E_k^2 \exp(-8.5/E_k), \quad (6)$$

where f is the frequency in MHz, and E_k is the Kilpatrick sparking limit in MV/m. At 805 MHz, E_k is about 26 MV/m. The axial accelerating field E_0 in a low energy standing wave structure is some fraction (typically 1/4 to 1/6) of the maximum surface field. For example, a maximum surface field of 40 MV/m ($\approx 5 E_0$) for the Linac Upgrade would correspond to approximately 1.5 times the Kilpatrick limit. The present drift-tube linac operates with a maximum surface field of about 1 E_k (≈ 15 MV/m) at 200 MHz.

The sparking rate per unit electrode area is a useful quantitative measure of sparking for different rf devices. The sparking rate is of course proportional to the electrode surface area (or specifically to that area in which the surface fields are within 90% of the maximum). It is a sensitive function of the pulse length T_p when $1 \text{ msec} > T_p > 10 \text{ } \mu\text{sec}$ with higher fields being supported at the shorter pulse lengths. The number of sparks/rf pulse is not very dependent on the pulse repetition rate f_{rep} when the duty factor ($f_{\text{rep}} \times T_p$) is less than 1%.

Since there is no comprehensive theory of rf sparking, experimental sparking rates can at best be fit to a function of certain parameters. The relatively complete data of Hutcheon et al⁹ suggests that the sparking rate per unit area, s , can be described by the exponential

$$s = a \exp[b(E_{\max}/E_k)^2], \quad (7)$$

where E_{\max} is the maximum surface field. The pulse length for the Fermilab linac is roughly 150 μsec . Using sparking data from Lehmann¹⁰ and Fermilab Linac operating experience yields the fit

$$s(T_p=150 \mu\text{sec}) \simeq 1.1 \times 10^{-12} \exp [1.88 (E_{\max}/E_k)^2] \text{ sparks/cm}^2/\text{rf pulse} \quad (8)$$

The high field nose cone tip area of the proposed side-coupled linac is 12 $\text{cm}^2/\text{nose cone} \times 896 \text{ nose cones} \simeq 10^4 \text{cm}^2$. Operation at 15 Hz (1.3×10^6 rf pulses/day) implies a sparking rate of about one spark/day if the maximum surface field is 1.5 E_k .

The documentation of x-ray emission (from field emitted electron bremsstrahlung) in high-gradient rf structures is more sparse than sparking-rate data. Generally x-ray emission rises exponentially with increasing electric fields and roughly linearly with increasing electrode surface area and duty factor. A dependence on the radio frequency can be hypothesized if the electron emission mechanism involves localized sites with frequency-dependent conduction characteristics (e.g. skin-depth effects). Excessive x-ray emission can be an operational constraint if it damages beamline organics (e.g. seals, insulation) resulting in significant downtime for repairs, drains expensive rf power or necessitates large amounts of shielding for personnel and peripheral equipment. Early 200 MHz drift-tube cavity studies at a 30 Hz repetition rate showed that x-ray emission of 400 R/hr occurred at a distance of one meter for surface fields of 36 MV/meter while for surface fields of 23 MV/meter x-ray emission was reduced to less than 4 R/hr.¹¹ Up to 6% of the rf power went into electron and x-ray emission at the highest fields.

A prototype SC structure was developed in collaboration with Los Alamos Scientific Laboratory and is being used in the first high power and peak field tests. It is illustrated in Figures 5 and 6. A second prototype featuring different mechanical details and tuning strategy is being developed at Fermilab.¹² Between the two accelerating sections shown in Figures 5 and 6 there is an offset rf coupler, called a bridge coupler, which is a suitable place to excite the structure and can be used also to provide space for a focusing quadrupole. To maintain synchronism between the rf and beam

particles these couplers must have length equal to an odd multiple of the elementary cell length $\beta\lambda/2$. Here β is the particle velocity divided by the speed of light, and λ is the free space wavelength of the rf. In the Linac Upgrade design the bridge couplers have a length $3\beta\lambda/2$.

The rf properties of SCS cells are determined from SUPERFISH calculations. The cell shown in Figure 7 is derived from the LAMPF linac; the bore radius has been reduced to 1.5 cm from 1.6 cm and the nose cone angle reduced from 30° to 20° to improve the shunt impedance. Cavity dimensions were calculated to maximize shunt impedance for all β . The program SUPERFISH has been used to calculate the transit time factor T, the effective shunt impedance ZT^2 and the ratio of the maximum surface field and average accelerating field E_{\max}/E_0 at several values of β corresponding to the energy range 116 to 400 MeV. Because this program is limited to azimuthally symmetric structures, it cannot account for the effect of the coupling slot and side cavity. Therefore, the calculated values of ZT^2 must be adjusted downward. Based on Los Alamos experience¹³ we expect ZT^2 to be 12.5% lower for the complete SC structure. Work done with the MAFIA¹⁴ three dimensional field codes provides a rough confirmation of this estimate. Additionally, some small adjustment should be made to account for surface imperfections and brazing artifacts. We assume a further 2.5% reduction of the SUPERFISH values of ZT^2 for these effects.

In Figure 8 the shunt impedance ZT^2 is plotted as a function of β from SUPERFISH results (not adjusted for slots and surface imperfections). In Figure 9 and 10 the transit time factor T and ratio E_{\max}/E_0 are plotted, respectively. For this optimization of the SCS, the power in each accelerating cavity is the same whereas the gradient E_0 drops somewhat as the energy increases. The smooth curves in Figures 8 through 10 are third order fits to the SUPERFISH results. These fits are employed to calculate the length and number of cells needed to reach the design energy subject to the constraints on peak field and power dissipation.

Because the introduction of the coupling slot also reduces the resonant frequency of an ideal, closed SC cavity, all of the SUPERFISH calculations were done for cavities resonant at

approximately 820 MHz rather than 805 MHz. The higher offset frequency was determined by previous Los Alamos experience and aluminum cavity models with 5% coupling (Section 3.3.1). A SC cavity constructed with the dimensions predicted by SUPERFISH at this offset frequency will actually resonate at approximately 805 MHz when the slot is cut. The offset frequency was adjusted in the SUPERFISH calculations by changing the gap length G between the nose cones. The half gap length as a function of β used SUPERFISH calculations is shown in Figure 11.

3.1.3 Segmentation of the Structure

3.1.3.1 Accelerating Modules

The division of the Linac into seven independently excited rf modules results from three principal considerations, namely the practical size for 805 MHz klystrons, the shunt impedance of the structure, and the existence of suitable penetrations from the equipment gallery into the linac vault for the waveguides. Uniform distribution of the rf power favors feeding the modules from the center, so there is a coupler at that location which can accommodate a quad also. Rf defocusing requires that the quads of a FODO channel be less than two meters apart in the first modules. Symmetry with respect to the rf feed point requires an even number of sections per module. These conditions are satisfied by dividing the modules into four sections separated by $3\beta\lambda/2$ bridge couplers (Figure 12). The transverse and longitudinal beam envelopes for this subdivision of the structure are shown in Figure 13.

The required number of accelerating gaps and the manner of dividing them up between modules is determined iteratively from the structure calculation. The ratio of the maximum surface field E_{\max} to the average axial field E_0 is known as a function of β from the SUPERFISH results. The number of accelerating gaps required to raise the energy from 116 MeV to 400 MeV is calculated subject to the condition $E_{\max} = 44$ MV/m in every cell from $E_0(\beta)$, $T(\beta)$, and $Z_{\text{sh}}(\beta)$ as represented by the third order fits. The cells are then divided into seven groups of equal dissipation including loading from a 50 mA beam current. Each of the seven modules are subdivided into four sections with the same number of cells. The acceleration is then

recalculated iteratively to determine a constant cell length $\beta\lambda/2$ for each section where β is the β corresponding to the average energy in the section for a particle that enters and leaves the section with the correct phase ϕ_s . To arrive at a regular segmentation with uniform power requirements a few more cells are used and the gradient is reduced somewhat so that the maximum surface field is in fact 37 MV/m in the resulting design. The reference design calls for seven modules of 4 sections each with 16 gaps per section. In each of the 28 sections the accelerating cells are of fixed length. The parameters for each section of the linac are given in Table 3.

3.1.3.2 Bridge Coupler

For the bridge coupler, we have adopted the five-post design developed at LANL for the LAMPF accelerator¹⁵ (Figure 14). It is a right circular cylindrical cavity with flanged ports at its ends which connect to the side cavities of the accelerating sections. The middle bridge coupler of a module has a flanged iris coupled waveguide port for matching to the klystron source. Five metal posts are installed on the bridge coupler cavity for fine resonant frequency adjustment, spectrum control as well as field flatness adjustment and frequency adjustment during the iris cutting process for couplers with waveguide ports. Two of the posts are placed along the central axis of the coupler in its end plates. Three posts are positioned along the cylindrical surface of the coupler. The center post has a rotatable notch for field flatness adjustment.

The three dimensional rf computer code, MAFIA¹⁴ was used to design the bridge coupler (Figure 15) meeting the requirements outlined above with the following conditions:

1. The bridge coupler must have the correct dimensions and post adjustment range to resonate within a few kHz in its TM₀₁₀ mode at the frequency of the accelerating mode (805 MHz) when attached to its adjacent accelerating sections. In addition to insure proper tuning range, the possible side cavity port impedances were simulated with shorted and opened waveguides of zero and quarter wavelengths. For couplers with waveguide ports this was repeated with the addition of an iris coupled waveguide port.

Table 3: Parameters of the 400 MeV linac listed for each accelerating section

Module /Sect.	Grad. [MV/m]	KE _{out} [MeV]	L _{rf} [m]	L _{sep} [m]	P _{Cu} [MW]	P _{beam} [MW]	Δv _{x,y} [deg]	Δψ _z [deg]
(Transition Section)								
0								
1	4.95	116.5	0.4254	0.3927	0.28	0.00		
2	3.16	116.5	0.2552	0.9751	0.07	0.00		
			0.0000	1.5748				
			0.6806	2.9426	0.35	0.00		
			3.6232		0.35			
1	8.04							
1		125.1	1.3814	0.1418	1.72	0.43		
2		133.8	1.4215	0.2628	1.84	0.44	77	109
3		142.8	1.4606	0.2703	1.89	0.45		
4		152.1	1.4987	0.2775	1.88	0.46	78	106
			5.7621	0.9524	7.33	1.78		
			6.7145		9.11			
2	7.82							
1		161.2	1.5353	0.2846	1.69	0.46		
2		170.6	1.5704	0.2912	1.81	0.47	80	103
3		180.2	1.6046	0.2977	1.85	0.48		
4		190.0	1.6380	0.3041	1.84	0.49	80	101
			6.3482	1.1776	7.19	1.90		
			7.5258		9.09			
3	7.63							
1		199.7	1.6700	0.3102	1.67	0.48		
2		209.5	1.7008	0.3161	1.79	0.49	81	98
3		219.6	1.7308	0.3218	1.83	0.50		
4		229.8	1.7600	0.3273	1.82	0.51	81	96
			6.8616	1.2754	7.11	1.98		
			8.1370		9.09			
4	7.46							
1		239.9	1.7881	0.3327	1.64	0.51		
2		250.1	1.8151	0.3379	1.77	0.51	81	94
3		260.5	1.8414	0.3428	1.81	0.52		
4		271.1	1.8670	0.3477	1.80	0.53	80	92
			7.3115	1.3611	7.02	2.07		
			8.6726		9.09			
5	7.32							
1		281.5	1.8917	0.3524	1.64	0.52		
2		292.1	1.9155	0.3570	1.75	0.53	80	90
3		302.8	1.9386	0.3614	1.80	0.53		
4		313.6	1.9612	0.3657	1.77	0.54	79	89
			7.7069	1.4364	6.96	2.12		
			9.1434		9.08			
6	7.18							
1		324.4	1.9829	0.3698	1.62	0.54		
2		335.2	2.0039	0.3738	1.74	0.54	79	87
3		346.1	2.0244	0.3777	1.77	0.55		
4		357.1	2.0443	0.3815	1.76	0.55	78	85
			8.0555	1.5028	6.89	2.18		
			9.5583		9.07			
7	7.07							
1		368.1	2.0635	0.3852	1.61	0.55		
2		379.1	2.0821	0.3887	1.73	0.55	77	84
3		390.2	2.1002	0.3921	1.76	0.56		
4		401.5	2.1179	0.3955	1.75	0.56	76	82
			8.3636	1.5614	6.85	2.22		
			9.9251		9.07			
Grand Total			51.0901	12.2098	49.70	14.25		
			63.2998		63.95			

2. The bridge coupler mode spectrum must be clean with no other resonances too near the desired $\pi/2$ mode frequency at its TM010 resonance. Adjacent resonances must be equally spaced around the TM010 resonance. This must be accomplished by adjusting the tuning posts while still satisfying condition (1) above. Table 4 lists the resonant frequencies and mode types of the nine lowest resonances found by MAFIA for a bridge coupler appropriate at 200 MeV. The open wave-guide port condition, the most perturbing, was used for these computer runs and demonstrates that the conditions (1) and (2) above can be simultaneously met.

3. To insure proper field flatness throughout a module, the field level of the bridge coupler must be adjustable. The flatness requirement is plus or minus 1%. A study of LAMPF experience indicates a possible field variation of 5% between sections. MAFIA results and the LAMPF experience indicates that rotation of the notched center tuning post provides adequate adjustment while satisfying conditions (1) and (2).

Table 4: 200 MeV Bridge Coupler Dimensions and Mode Spectrum

Main Cavity Radius = 13.462 cm
 Main Cavity Length = 45.725 cm
 Post Tuners Radius = 3.175 cm
 Center Post Extent = 5.0 cm
 End Tuners Extent = 1.6 cm
 Adjacent to Center Post Extent = 4.8 cm

<u>Mode Type</u>	<u>Frequency (MHz)</u>	<u>Remarks</u>
TM010	804.360	Desired $\pi/2$ mode
TM011X	814.042	Peak E field in X direction
TM011Y	935.193	Peak E field in Y direction
TE111Y	770.739	Peak E field in Y direction
TE112Y	929.269	
TE113Y	1093.27	
TE111X	641.292	Peak E field in X direction
TE112X	793.009	
TE113X	969.215	

3.1.3.3 Coupling Constant

The coupling constant k between accelerating and side cells in side-coupled structures has typically been chosen in the neighborhood of 5%. A value of 4.8% was chosen for the Linac Upgrade with the expectation that some variation in the coupling will occur over the Linac. A 5% coupling slot reduces the shunt impedance by about 12.5% relative to an unslotted accelerating cell. Higher couplings reduce the shunt impedance unacceptably with experience indicating $(\Delta ZT^2/ZT^2)/(\Delta k/k) = -0.13$. Smaller couplings lead to an excessive power flow amplitude droop and phase shift in long chains of coupled accelerating cells.¹⁶ Amplitude droops exceeding a few percent and phase shifts greater than a few degrees can be deleterious for linac beam dynamics and regulation.

The power flow amplitude droop is the change in field amplitude observed N_a accelerating cells from the rf drive port due to resistive wall losses. For small couplings, the amplitude droop is

$$\Delta A/A = 2N_a^2/k^2Q_aQ_c \quad (9)$$

where Q_a and Q_c are the resonant widths of the accelerating mode for accelerating and coupling cells. Side-coupled cavity models and SUPERFISH calculations indicate that Q_a will vary from 2×10^4 to 2.4×10^4 and Q_c from 1.4×10^4 to 1.7×10^4 between 116 MeV and 400 MeV in the Linac Upgrade. With the rf drive at the central bridge coupler of a module, the number of equivalent accelerating cells to the end of a module is $N_a = 2 \times 16$ accelerating cells + 1.5 equivalent cells for the bridge couplers = 33.5. For 5% coupling, $\Delta A/A$ varies over the range 0.3% to 0.2% between the low and high energy ends of the SC linac.

The power flow phase shift is a measure of how far the operating frequency shifts to distribute power in a structure which has a stopband. Since accelerating cells and coupling cells never have exactly the correct frequency to close the stopband at the $\pi/2$ accelerating mode in a coupled chain, every real side-coupled structure will have a small stopband, typically of order 100 kHz for an 805 MHz structure. For small couplings, the power flow phase shift is

$$\Delta\phi = 4N_a^2\Delta f_s/k^2Q_a f_{\pi/2} \quad (10)$$

where Δf_s is the stopband, and $f_{\pi/2}$ is the accelerating mode frequency. For 5% coupling and a 100 kHz stopband, $\Delta\phi$ varies over the range 0.6 to 0.5 degrees between the low and high energy ends of the SC linac.

3.1.4 Transverse Focusing

3.1.4.1 Lattice Design

The rf power distribution scheme results in a symmetric arrangement of accelerating sections with a coupler at the midpoint. The further segmentation required to provide for transverse focusing can be established by calculation of the growth of the beam envelope from a waist in the structure to a proposed quad location. The rf defocusing has its greatest strength relative to the focusing quads at the low energy end of the linac where the unnormalized transverse emittance and tune spread arising from bunch width are highest. The overall character of the focusing scheme follows from the appropriate distance between elements established for the first module, the lattice type selected, and the sequence of module lengths resulting from the requirement for the same rf power per module. The circumstance that the power distribution is optimized with an equal number of accelerating gaps in each module results in module length increasing smoothly with energy. The focusing is naturally strongest at the low energy end because the maximum of the transverse β -function (envelope width function) depends primarily on the length of the focusing cells and only weakly on the strength of the focusing quadrupoles.

For each choice of quad spacing there is a particular β_{\min} , the width Twiss parameter at the waist, for which the beta function at the quad, β_{\max} , has its minimum value. The values β_{\min} and β_{\max} can be used as fitting conditions at the beam waists along the structure to determine the required quad strengths. Because the optimum power distribution for the optimized SC structure leads to a fixed number of cells per section, the section lengths increase smoothly with energy, and the same β_{\min} , β_{\max} pair can be used for all focusing

cells. Alternatively by choosing the same quad strength throughout the linac one obtains a β_{\max} that increases slowly with energy while the transverse oscillation phase advance increases slightly. The beam envelope shrinks, however, because of the inverse dependence of transverse emittance on momentum. For 8 cm long quads with a 2 cm aperture and pole tip fields of approximately 5 kG the phase advance is in range 77 to 80 degrees and β_{\max} is minimized at the low energy end. Because the low energy modules are shorter, four sections per module are sufficient to get the required quad spacing at low energy. The same subdivision suffices at higher energy because the rf defocusing decreases sufficiently.

Figure 13 shows the initial beam ellipses, final beam ellipses and the beam envelopes along the linac in all the planes on the basis of the parameters in Table 2. This figure and the β_{\min} , β_{\max} values were calculated by the program TRACE 3-D which takes account of rf defocusing and space charge in a linear approximation.¹⁷ Particle dynamics calculations have been made which verify the TRACE 3-D results. Some results of the dynamics calculation for the linac and transition section are presented in Section 3.1.5 where the transition section is described.

The possibility of using quad doublets or triplets instead of the FODO scheme has been examined. Because couplers dissipate some rf power and take up scarce space, it is appealing to reduce the number of couplers by focusing in both planes at each break in the accelerating structure. However, the beam spreads too fast to be contained by multiplets only between modules. Therefore, the center coupler must contain a multiplet. The bridge couplers to accommodate a doublet or triplet would be $5\beta\lambda/2$ in length. There are significant difficulties with a multiplet focusing design. The longer focusing periods would have transverse phase advances of more than 90 degrees, exceeding a stability limit for beams under the influence of space-charge.¹⁸ Also in order to keep the longitudinal phase oscillation within the linear region of the rf bucket, the cell length should be changed within a section. Another disadvantage is that the quadrupoles for a multiplet are much stronger than the FODO quads and would be considerably more difficult to make.

3.1.4.2 Quadrupole Design

A pulsed quadrupole with a 2 cm pole tip radius and core length of 7 cm is being designed for use with the SC linac and transition section. Final details of the endpack and mechanical scheme will establish an overall length of about 8 cm. To the extent that the length exceeds 8 cm it will be necessary to shorten a steering coil and beam position monitor in the first accelerating module. Such adjustment is feasible and is probably preferable to reducing the quadrupole core length. The electromagnetic properties are given in Table 5 and an octant cross section with field lines calculated by the POISSON program are shown in Figure 16. The highest fields in the iron are about 14 kG, and the gradient is uniform to better than 0.1% at the beampipe radius. The magnet is to be excited with a half sine wave of about 2 ms giving a duty factor of 1.5% at 15 Hz. These requirements can be satisfied by the existing linac quadrupole power supplies should it be economical to use them.

Aperture radius (r_p)	0.02	m
Beampipe radius (r_b)	1.5	cm
Magnetic length (l_{eff})	0.07	m
Physical length	~ 0.08	m
Gradient (B')	263.	kG/m
Gradient error at r_b	0.04	%
Number of turns per pole	24	.
Current for $B'(\hat{I})$	175.	A
Resistance (R)	445.	m Ω
Inductance (L)	1.36	mH
Pulse length, half sine wave	~2.	ms
Peak voltage (\hat{V})	413.	V
Stored energy	25.	J
Duty factor at 15 Hz	1.5	%
Peak real power ($\hat{P} = \hat{I}R$)	1351.	W
Eddy current loss in iron	31.	W
Eddy current loss in copper	1119.	W
Average power (\bar{P})	39.1	W

Table 5: Quadrupole Parameters

A sketch of the cross section showing some structural details is given in Figure 17. The quadrupole halves are joined by bolted flanges to permit installation around the beam pipe in the tightly packed spaces between the lower energy acceleration sections. The alignment keys passing through the core are designed to permit unlimited mounting and dismounting without loss of field quality. The low duty factor permits cooling by a water circuit inlaid in the outer surface of the core.

3.1.5 Transition Section

The 200 MHz drift tube linac operates with stronger transverse focusing and weaker longitudinal focusing than the SC linac which follows it. Therefore, six-dimensional phase space matching is required to preserve the brightness of the input beam in its new electromagnetic environment. The matching requirements are summarized in Table 6. We know approximately the transverse emittance from measurements at 10 MeV and 200 MeV. However, the parameters of the 116 MeV transverse phase space beam ellipses are known only from PARMILA simulation. The simulation shows the beam to be rather poorly matched at the end of drift-tube tank 5, but one can expect to retune quads for matched conditions once the space is available to make good beam measurements. Therefore, the design of the transition section proceeds from nominal ellipse parameters but provides flexibility to handle a range of conditions that the simulation indicates could occur.

The longitudinal emittance is inferred from bunch width and momentum spread measurements at 200 MeV. If these two numbers have been measured correctly, ϵ_l in Table 6 is an upper limit, because the beam is assumed to be uncorrelated. The quoted value is, however, a factor of two or more less than earlier estimates. Although the bunch length measurement is somewhat difficult, it is not likely that the error in the measurement is as large as a factor of two. The consequences of an underestimate of this magnitude are not major. The beam would still fit reasonably within the approximately linear portions of the rf waveform. The debuncher in the 400 MeV line (see Section 3.5.2) would be better positioned in an alternate location, however.

Kinetic energy	116.54	MeV
Beam current, averaged over pulse	50.	mA
Longitudinal emittance ϵ_L (90 %)	2.6	$\times 10^{-5} \pi$ eVs
Transverse emittance $\epsilon_{x,y}$ in (90 %)	13.4	π mm mrad
Drift tube linac		
frequency	201.25	MHz
effective gradient E_0T (exit)	1.77	MV/m
accelerating phase φ_s	-32.	deg
FODO half-cell (exit)	67.9	cm
exit aperture	2.0	cm
116 MeV beam (nominal)		
β_x	0.52	m
β_y	2.26	m
β_φ @ 805 MHz	0.0502	deg/keV
Coupled cavity linac		
frequency	805.0	MHz
effective gradient E_0T (entrance)	6.81	MV/m
accelerating phase φ_s	-32.	deg
FODO half-cell (entrance)	164.0	cm
entrance aperture	1.5	cm
matched waist		
β_x	1.06	m
β_y	8.65	m
β_φ @ 805 MHz	0.0131	deg/keV

Table 6: 116 MeV Matching Requirements

The longitudinal matching is effected by placing a five-cell 805 MHz buncher immediately after drift-tube tank 5. For a given ΔE , $\Delta\phi$ beam ellipse there is a unique combination of buncher gradient and down-stream drift resulting simultaneously in an upright ellipse and the bunch width matched to the first accelerating section of the SC linac. However, the precise beam parameters are not known a priori and may be expected to vary somewhat day-to-day. Because there are two parameters to be matched and because the drift distance is not a convenient tuning variable, a three-cell vernier buncher is located about one third of the way along the bunching drift space to provide the needed second variable parameter.

The transverse matching requires at least four quadrupoles to control the phase ellipse parameters α and β in both horizontal and vertical coordinates. A fifth quadrupole is desirable to provide an extended range of matching capability and to help control the width of the beam envelope in the transition section. The smoothest transverse matching would be accomplished by extending the FODO sequence of tank 5 with matching quads spaced increasingly far apart to interpolate between the length of the last FODO half-cell in the drift-tube linac and the first one in the SC linac. For this consideration it is unfortunate that the bunching drift is far too short to accommodate five quads according to this prescription. The most regular disposition of the quadrupoles within the transition section is obtained by using the last three quads of tank 5 for transverse matching; the final two matching quads are spaced so that there is a sequence of five linearly increasing inter-quad spaces before the first accelerating section. This spacing requires lengthening the debunching drift by about ten percent above the calculated nominal, but the effect is easily compensated by the vernier buncher.

The result of a TRACE-3D calculation for the transition section is given in Figure 18. One can see that the transverse envelopes are somewhat irregular despite the effort to optimize quad spacing. This distortion is accounted for primarily by the fact that the betatron phase advance per FODO period is considerably less in the drift tube linac than in the SC linac. Therefore, the transverse matching must include an adjustment of the ratio of $\beta_{\max}/\beta_{\min}$, i.e., the aspect ratio of the x-y beam ellipse. The matching depends upon simultaneous horizontal and vertical plane phase advances not characteristic of a regular FODO channel. The parameter values for the components indicated in Figure 18 appear in Table 7.

To test the effectiveness of this transition section, numerical simulations were performed using the codes PARMILA and DDYN to track the beam through the transition section and the final seven side-coupled modules. The SCS parameters from Table 3 were used in this simulation. The results are shown in Figures 19-22. Figure 19 shows the rms bunch z-radius expressed in rf degrees along the length of

Table 7: Transition Section Parameters

Component	Length [m]	B' [T/m]	E ₀ T [MV/m]
Linac quad, half	0.0823	9.00	
Linac gap	0.5119		1.77
Linac quad	0.1646	-13.40	
Linac gap	0.5144		1.77
Linac quad, modified	0.1646	19.97	
Drift	0.1500		
SC buncher section	0.4254		4.95
Drift	0.2213		
T. Sec. quad	0.0800	-27.90	
Drift	0.6738		
SC buncher section	0.2552		3.16
Drift	0.1500		
T. Sec. quad	0.0800	29.67	
Drift	1.3190		
SC linac quad	0.0800	-23.00	
Drift	0.1018		

Note: New quad physical and magnetic length arbitrarily set to 8.000 cm

the 805 MHz structure. The effect of the transition section in reducing the bunch z-dimension is shown. Residual damped synchrotron oscillations are evident. These oscillations are created by the debunching in the drift regions between sections that provide space for quads and beam diagnostics. Figure 20 shows the variation of longitudinal emittance along the new linac. No evidence of z-plane dilution is seen at the design current of 50 mA.

Figures 21 and 22 show the x-plane beam radius and normalized emittance, respectively for a 90% beam envelope, through the transition section and the 28-section acceleration system. The radial excursions in the transition section are seen not to be severe. Predicted transverse emittance growth was typically 10% to 20% for the 90% beam envelopes at the 50 mA design current.

3.1.6 Prototype Accelerating Module

With the design parameters of the side-coupled linac and transition section specified as in Table 3, the definition of a suitable prototype structure for the Linac Upgrade was undertaken. The prototype must answer essentially all questions regarding the fabrication, tuning, temperature regulation, vacuum requirements, support and alignment for side-coupled accelerating structures. It must also serve as a test of the machining and brazing sequence which will be needed to sequentially assemble the seven accelerating modules.

The proper alignment of four accelerating sections on a support girder to make a module is critical for the beam dynamics. The overall tuning of the four sections and three bridge couplers will determine the quality of the accelerating fields in a module. The above considerations suggested that a complete accelerating module would be an appropriate prototype structure (designated Prototype R). This prototype is intended to correspond mechanically and electrically to Module 1 of the SC linac (Figure 23) for several reasons.

The space between sections for quadrupoles, steering dipoles, beam position monitors, wire monitors, toroids, valves, bellows and flanges is the least in Module 1 ($L_{sep} = 3\beta\lambda/2 = 26.3$ to 27.8 cm) and proper mechanical sizing of components is critical here. Engineering studies indicate that appropriate combinations of these components can be accommodated in the space between sections and modules (Figures 24-27). The first module is the shortest (6.5 meters) and lightest (8000 lbs including girder) and involves the least amount of copper for accelerating cells. Full power testing would require less overall x-ray shielding. If Prototype R is successful, it would be used as the first accelerating module representing a significant advancement in schedule of the Linac Upgrade.

The accelerating and coupling cells will be brazed together using the segmented construction originally used on the 805 MHz LAMPF linac (Figure 28). In this construction, the side-cells consist of two-halves (clam shells) brazed together to form a coupling cavity.

This is then brazed into an accelerating segment which is two half accelerating cells machined back to back out of a solid copper cylinder. The complete segments are then stacked, tuned and brazed into an accelerating section (see Section 3.3.1).

3.2 Radio Frequency Power System

3.2.1 Power Requirements

The 805 MHz Linac Upgrade requires seven high power klystron and modulator systems to increase the output energy of the Linac to 400 MeV. Table 3, for the 400-MeV linac shows the copper loss P_{Cu} and beam power P_{beam} for each of the seven modules. A complete power tabulation takes into account additional items, listed in Table 8.

A) Typical power, accelerating 50 mA beam.....	9.1 MW
(refer to Table 3). Superfish shunt impedance has been derated for slots (12.5%), brazing and surface imperfections (2.5%), and transit-time factor T).	
B) Waveguide run, (WR975), isolator (if required), VSWR.....	0.6 MW
C) Add 10% for feedback loop regulation.....	<u>1.0 MW</u>
	10.7 MW
D) The cavity diameter may have to be altered slightly at some β 's to avoid TM ₁₁₁ and TM ₁₁₀ deflecting modes.....	<u>0.1 MW</u>
	Est Total 10.8 MW

Table 8: RF Power Tabulation

The power tabulation in Table 8 for the present design shows less than an 11 MW total peak power requirement. The Klystron specifications in Table 9 apply to the 12 MW prototype Klystron (Figures 29 and 30) which is on order with Litton Systems, Inc., and is due in September 1989. The 12 MW rating is nominal at 50% efficiency, but the klystron could most likely run at a higher power with some reduction in efficiency. Since the peak power requirement for the Linac Upgrade is 10% below the nominal klystron rating, the Litton klystron should be a completely adequate device.

The RF power requirements for the transition section (Section 3.1.5) and the 805 Mhz debuncher (Section 3.5.2) are less than 1 MW and can be supplied comfortably by the Los Alamos type klystron or a klystrode.

Peak power output	12 MW
Pulse length	125 μ s
Pulse repetition rate	15 pps
Duty factor	0.1875%
Average power	22.5 KW
Efficiency	50%
Gain	50 dB
RF output	WR975 waveguide
Dimensions	108 inch height 24 inch diameter
Voltage	170 KV
Current	141 A

Table 9: Klystron Specifications

3.2.2 RF Modulator

The RF modulator specifications are given in Table 10.

Peak Power	24 MW
Voltage	170 kV
Current	141 A
Pulse repetition rate	15 pps
Pulse length	125 μ s.
Rise time	9 μ s.
Fall time	18 μ s.
Average power	50 kW
Pulse Flatness	+ - .5%
Voltage regulation	+ - .05%
D.C. power supply	9.0 kV at 6.5 A
Dimensions	See Figure 27

Table 10: Modulator Specifications

The physical layout of the modulator and klystron is shown in Figure 31. The modulator consists of a PFN (Pulse Forming Network)

discharged into the Klystron through a 20:1 set-up transformer, as shown in Figure 32. An ignitron crowbar has been added to the circuit to protect the klystron from damage when it sparks. The PFN is charged to 18 kV using the resonant charging technique, as shown in Figure 33. Our charger uses an SCR (silicon controlled rectifier) switch to initiate the charging cycle; this allows us to delay recharging until the PFN SCR switch has shut off.

3.2.3 System Regulation

The schematic block diagram for a typical rf system is shown in Figure 34. The system contains rf feedback loops for stabilization of the accelerating fields. At this point we may list the major disturbances to the accelerating fields:

1. Modulator voltage regulation ($\pm 0.5\%$)
2. Accelerator section temperature changes ($\Delta f \sim -14 \text{ kHz}/^\circ\text{C}$)
3. Transient and steady-state beam loading during rf pulse (20% power increase, $7^\circ \Delta\phi$).
4. Faults, e.g. modulator or gun sparking, rf sparking in accelerating sections or at windows.
5. Mismatch during cavity field buildup and decay (leads to high VSWR for $\sim 10 \mu\text{sec}$).

For item 1 above, a local feedback loop directly around the klystron rf output to input is planned. In addition to reducing klystron phase shift with beam voltage, the loop will linearize the klystron power output curve, producing a straight line response essentially up to saturation. This helps the global feedback loop maintain an optimum response. Feed forward from the modulator can further assist the regulation.

The accelerator section temperature (item 2), will be maintained with a stabilized water temperature system whose set point will be controlled for maintaining resonance at the operating frequency. Additionally, the location of the water cooling pipes on the accelerating sections will be chosen to minimize any opening of the stopband with duty factor change.

Beam loading disturbances (item 3) will be controlled by a feedback system incorporating pickup loops in the side coupled cavity structure. Placing these loops midway between the rf feed point and the far ends of the module minimizes the net disturbance for a given feedback loop gain. In addition to feedback stabilization, feed forward compensation using a signal from a beam intensity pickup at the entrance of the first drift-tube tank is a further refinement.

In case of modulator or gun faults (item 4), a crowbar is provided at the primary of the modulator transformer, activated by over-current. For rf faults, the klystron drive will be interrupted to prevent sparking damage. Rf mismatch during cavity buildup (item 5) can produce large voltage standing wave ratios (VSWR), which are potentially damaging to klystron and waveguide windows. Careful transmission line design between the klystron and the accelerator should insure that reflections during buildup will present a low impedance to the klystron output gap. Microwave windows will be placed at VSWR minima in both the klystron and bridge coupler.

Testing the impedance matching and VSWR protection concepts will be done as part of the power testing of the SCS prototype structures. In addition, the feedback and feed forward circuits will be examined theoretically and experimentally. If high-power circulators are deemed necessary between the klystron and the accelerator structure, they can be incorporated into the system. They are costly items, however, so the alternate approach is warranted.

3.2.4 Amplitude and Phase Control

As mentioned above the amplitude and phase of the fields within the accelerator modules will be regulated using a feedback control system. A pair of nested feedback loops will be used to regulate the klystron output separately from the module fields. The feedback loop controlling the module fields will use a feedback signal from a small loop probe placed in one of the cavities. The klystron feedback loop will use a feedback signal from a directional coupler located near the output of the klystron. The klystron feedback loop will use a feedback signal from a directional coupler located near the output of the klystron. The klystron loop regulates klystron output before it is directed to the modules. Without this loop, the klystron would be

regulated by the overall feedback loop around the module, and variations in klystron output would have to be sensed from within the accelerating module. The feedback loop around the klystron also linearizes the overall transfer characteristics of the attenuator/amplifier chain, which holds the incremental gain nearly constant up to saturation of the klystron.

The simulation language ACSL (Advanced Computer Simulation Language) has been used to analyze the performance of the loops. Figure 35 is a diagram of the model used to analyze a possible feedback configuration for the Linac Upgrade.¹⁹ This is perhaps the simplest configuration that could be used, having no compensation networks and no feed-forward circuits. The loops include delay lines in the feedback paths to model signal propagation delays in transmission links. Careful consideration of cavity response to arbitrary inputs reveals that each accelerator module can be modeled as a pair of low-pass filters which process separately the real and imaginary parts on input phasors. The analysis indicates that for this relatively simple feedback scheme, amplitude fluctuations can be reduced by a factor of twenty and phase fluctuations by more than an order of magnitude before the system becomes unstable. These levels of regulation should satisfy the requirements for the Linac Upgrade. Further improvements in regulating can be obtained using the Smith compensation principle and feed-forward scheme.²⁰

In order to properly set the amplitude and phase of the modules, we propose to use the "delta-t procedure" developed at the Los Alamos National Laboratory and used extensively on the accelerator for LAMPF.²¹ The method involves measuring changes in the time of flight for particle bunches through successive modules as the rf power applied to the module being tuned is alternately turned on and off. The times of flight are measured by a phase comparison technique which uses a series of phase bridges. The procedure will require beam position monitors in each of the seven SCS modules. It is anticipated that the monitors will consist of strip line detectors similar to those presently used on the Fermilab Linac. Coarse setting of phase and amplitude will be performed by measuring the beam loading within the cavities.

3.2.5 Prototype 12 MW RF System

The prototype 12 MW rf system is intended to provide answers to several questions presently under initial study with the 1 MW test stand which is in use primarily to study peak fields and x-ray levels in small SC cavity models.

The typical WR-975 waveguide length between the klystron and accelerator will be 100 feet. To preserve the waveguide interior surface and prevent contamination, the guide will be pressurized to 0.5 PSIG dry air. Therefore, for each accelerator module, there will be two waveguide windows. The Klystron window is an integral part of the Klystron as provided by the vendor. However, the window at the bridge coupler will be attached by Fermilab. Each window will be placed electrically at its detuned short position in the guide. The total electrical guide length will be adjusted to be an integer number of half wave lengths long. From $\lambda_g = \lambda_c / ((\lambda_c / \lambda)^2 - 1)$, where λ is the free space wave length, λ_c is the guide cutoff wave length and λ_g is the guide wave length, we find $\lambda_g = 56.4875$ cm, and therefore a guide nominally 100 feet long would be set to $108 \lambda / 2$ (using a settable phase shifter). In addition, broadband harmonic absorbers will be coupled to the guide to reduce the Q for modes with frequencies above 805 MHz.

Based on model tests, it is expected that the described configurations will perform adequately for normal operation as well as during fault conditions. Of course, a 12 MW test is necessary to confirm this expectation. The performance under sparking, which will be documented carefully to insure there is no degradation of components.

The waveguide window at the bridge coupler will be titanium coated on the vacuum side. After pumpdown of the accelerating module, a window conditioning period starting at reduced duty factor is necessary in order to safely bring the window up to full power. Thus window conditioning and cavity conditioning will be taking place simultaneously, but the conditioning rate will be governed by the slower of the two processes.

The 12 MW Litton klystron lends itself to higher power operation if required. Because its idler cavities contain tuners, the klystron

can be set (at the factory) for efficiency tuning or broadband tuning.²² Because of power requirements, efficiency tuning will be selected if there are no concomitant ill effects on the regulation loops or fault protection. The 12 MW prototype test will guide the selection for production klystrons.

Sparking is to be anticipated in the high power components of the pulse and rf system. Protective circuits for the klystron gun, the waveguide, the accelerating sections and the windows will be tested and refined in the 12 MW prototype test. As examples, the modulator PFN stores over 3KJ, but it is essential to limit a spark in the gun to ~5J. The accelerating modules store about 40J, and a fair fraction of this will feed the vacuum sparks during conditioning. However it is not desirable to allow the klystron to continue to generate rf power when a vacuum spark occurs so the drive will be gated off. The plan is to have fully operational fault protection for video and RF, under all conditions including initial operation of the prototype.

The 12 MW prototype rf system has the full thermal time constant to test temperature control. The rf stored energy and filling time will be the true values rather than extrapolations from the 1 MW test stand. Both these features make it an essential step in the construction of the rf systems for the Linac Upgrade.

The development of a modulator is central to the prototype 12 MW rf system. A prototype modulator will be operational in September, 1989. It will be used to test the Litton prototype Klystron tube and also to verify modulator design choices. The prototype modulator is sized to run at peak power greater than 42 MW, in order to accommodate unexpected inefficiencies in the klystron tube. It is conservatively rated so as to handle longer pulse lengths and high power losses.

One of the design elements to be tested with the prototype is the use of SCR's as the PFN discharge switch. SCR's are desirable because of their long lifetimes and their relatively slow turn-on which creates less electrical noise in the environment. The SCR's for the present application will switch high currents at a high rate of 1200A/ μ sec. Some SCR's have been tested and look adequate for

this application. Another design element to test is the choice of PFN charging supplies. A standard resonant charging supply is being built because it should be more economical than purchasing banks of commercial high-voltage switcher supplies.

3.3 Mechanical Systems

3.3.1 Construction and Tuning of Side-Coupled Structures

The fabrication and tuning of side coupled structures are strongly interrelated. Very tight mechanical tolerances or clever fabrication sequences are required. One can draw from the previous experience of LAMPF and subsequent structure fabricators. Satisfactory structures can be assembled in a straight forward manner. It is, however, desirable to reduce tuning steps that require repeated machine set-up and trimming of parts (for example the noses of accelerating cells). With the CNC machines available today it is possible to directly machine cell contours to a calculated contour. Our method uses high speed turning with a diamond cutter to contour the final finish of the cells. The nose of the accelerating cells are not touched after machining. The result is a very well controlled surface in the high field gradient region. Final tuning of the cell is done by controlling the depth of the coupling slots. This changes both the cell frequency and coupling but adequate predictions of the correct frequency off-sets to use beforehand can result in a coupling constant that falls within an acceptable range when tuned properly.

A side-coupled structure consists of an interior section made up of a stack of basic cells. A segmented construction is assumed here (Section 3.1.6). The basic cell (1/2 accelerating cell-coupling cell - 1/2 accelerating cell) is the smallest sub-assembly that will support a $\pi/2$ accelerating mode. Ends may be terminated with flat plates, a terminating 1/2 cell, or bridge terminating ends. The proposed tuning and assembly steps are shown in Figure 36 and described here.

- (a) The accelerating and coupling cavity components are machined to precalculated dimensions determined by experimental models and

SUPERFISH (SF) calculations. CNC machining of aluminum models has demonstrated that we can repeatedly predict the required frequencies with SUPERFISH (using a mesh size of .030") and then accurately machine to the desired frequency. Frequency accuracy for 1/2 cell machining is about ± 100 KHz if taken randomly. If the order of stacking cells is taken with care ± 20 KHz can be achieved in matched full cells at final assembly. At this step the parts are still in the round. No coupling slots and unbalancing machine cuts have been made. Coupling slots lower the frequency of a previously axially symmetric cavity. Models of 200-MeV cavities with approximately 5% coupling required an accelerating cell SUPERFISH value of 821.7 MHz and a coupling cavity SUPERFISH value of 834 MHz. The two clamshells which make up the coupling cell are brazed together. Note the dents which can be dinged inward to raise cell frequencies. Six are provided in each 1/2 cell. Each one can raise the cell by 50 to 100 KHz.

- (b) Coupling slots are machined into the accelerating cell. The parts are clamped together. Increasing the depth of the slot lowers the SUPERFISH frequency of both cells. Since we do not want to machine repeatedly on the accelerating cells we have concentrated on obtaining the correct frequency when a slot size gives the desired 4.8% coupling. While machine errors of .0005" on the nose height give 100 KHz frequency errors in the accelerating cells, the same error in coupling cells give a frequency shift of about 400 KHz. The coupling cells can be accessed inside or outside so their gaps can be squeezed together or spread apart. Several MHz of tuning has been achieved using this technique.
- (c) The $\pi/2$ frequencies for a pair of cells, half terminated with a flat plate, are measured and then the stacked pair is measured. The slot is adjusted until the plot of frequency vs $1/n$ (n = the number of 1/2 cells) gives the correct frequency as n approaches infinity. After the correct slot depth is determined all remaining cells will be machined on a CNC mill and the coupling cells brazed to the accelerating segments. This step has been done for 200 MeV cavities and along with LAMPF data we have extrapolated target SUPERFISH frequencies and coupling slot geometries for the complete Fermilab Linac Upgrade. We expect to do some additional modeling with aluminum cavities as real values depart from those we project.

- (d) The half-cells will be stacked in a selected order to best equalize the accelerating cell frequencies. The $\pi/2$ frequency will be checked and the coupling cavities will be adjusted to close the stopband to within a few MHz. Fine adjustment of the accelerating cavities can be done at this step by lapping the surface where they would be brazed together. Approximately 50 KHz change per .001" of surface material removed is typical.
- (e) All cells will be machined to the same nose cone shape. This equalizes the fields of all cells and does not provide a preferential sparking gap. The end cell of the first or last section of a module which has no coupling slot requires a lower SUPERFISH frequency (as measured against a flat plate, it is just under 805 MHz). This end cell will be lowered by machining at the outer cavity radius in the low electric field region of the cell. End cells connected to the bridge coupler which have slots but have less direct coupling need to be lowered slightly in frequency. Pushing the end nose cone in slightly can tune these end cells with less than a 1% increase in the field level on average. Starting with an assembled frequency of 804.600 MHz at the operating temperature and under vacuum before dinging should give adequate range for final tuning to 805 MHz. As we gain experience we expect to be able to tune closer to 805 MHz in brazed structures. With the indicated tuning margin it may be possible to weld structures together and eliminate the expensive braze steps.

Brazing is the conventional method of constructing side-coupled structures. The brazing process has as many as four steps in order to construct a vacuum tight cavity structure. Nicoro (35 Au - 62 Cu - 3 Ni) is used as the highest temperature alloy (1900 F) to make all the copper to stainless steel joints, and to braze the side-cell clam shells together. If step brazing is necessary in joining the stainless steel to copper, then 35 Au - 65 Cu alloy is used. This brazing step occurs in the bridge coupler. The side-cells are brazed to the accelerating segments using 50 Au - 50 Cu alloy. The final stack braze uses Cusil (72 Ag - 28 Cu). If a vacuum leak should occur during the final braze, the alloying properties of the Cusil allows one to repeat the braze at the same temperature or slightly

lower in order to repair the leak. All the braze joints were designed to reduce the amount of blushing on the inside surfaces of the side-coupled structure.

3.3.2 Temperature Regulation

The cooling system for the seven side-coupled modules will be installed in the basement of the Linac building in between the existing equipment. Approximately 100 KW of heat will be dissipated by the seven SC modules in the industrial chilled water (ICW) system which presently is installed in the basement. Careful sharing of the available cooling water will be required during the simultaneous testing of the new linac and the normal operation of the drift-tube linac. The ICW cooling load for the existing equipment is close to its maximum capacity especially in the summer when the air conditioning demand is high.

Low conductivity water (LCW) of about 10 megaohm-cm resistivity will regulate the temperatures of the modules. A supply and return manifold will be installed in the basement near the existing ICW piping. A cooling skid, with a heat exchanger, pump, regulating valves, and a deionizing system will cool and process the LCW using the chilled water as a heat sink.

Seven cooling racks (one for each accelerating module) will be installed near the existing wall penetrations which connect the basement to the Linac enclosure. Each rack will have four individual water temperature controlling crates. Each crate will remotely control the temperature of one section of a module. The crates will be stacked on top of each other and they will all be of the same construction. One or two spare units could be made for emergency crate replacement. Temperature regulation will also be available to the adjacent bridge coupler by controlling the water flow. All of the twenty-eight crates will be connected in parallel to the LCW manifolds. The existing wall penetrations will be used to route the insulated copper tubes to the modules. Figure 37 shows a simplified schematic of the cooling system for one section of the SC linac.

Each cell has one-half inch copper tubing brazed azimuthally in a groove around the outside surface. The tubes have spiral inner fins to increase the heat transfer surface area and to create a turbulence in the water to improve the film heat transfer coefficient. The tubes are connected in parallel to the manifolds. Two supply and two return water manifolds will be used with the side-coupled structure design. Alternate supply and return connections will give a uniform temperature distribution in the cavity section. This will keep the section straight during the thermal cyclings.

Each section with the adjacent half of the bridge coupler will have a separate cooling loop. The main components, consisting of a computer controlled valve, a mixing vessel, a small pump, and a heater will be installed in a metal crate. The remote controlled valve will regulate the flow of 60° F water into a mixing vessel to cool the circulating water for the rf cavities. The temperature of the water will control the final physical dimensions (through thermal expansion) of the cavities so that the desired rf tuning can be achieved. The bridge coupler, bringing the power to the connecting section, will use the water from the same cooling loop. The flow of water to the coupler could be controlled to regulate the temperature.

For mechanical stability, each section should have a uniform temperature distribution. A low water temperature differential from the supply to return is therefore required. The peak rf power of a module (4 sections) is about 7 MW, and the duty factor is 1.875×10^{-3} . With an average rf power of 3.3 KW for each section and bridge coupler (which contributes only a few percent of this power) a water flow of 1 GPM will give a water temperature rise of 1°C. Very little heat will be dissipated into the room. The hydraulic resistance is low with parallel connections so a small pump of 1/3 HP will circulate the water with a 12 psi head pressure.

When the RF power is turned off, an electric heater will raise the temperature of the water to keep the cavities mechanically stable for the required rf tuning. The size of the heater will be determined once from side-coupled prototypes the optimum temperature of the cavities and the time allowed for operational changes is determined.

3.3.3 Vacuum System

The SC linac vacuum system will employ a 6 inch diameter high vacuum header for each module. Each of the 4 sections of a module connects to a corresponding length of the high vacuum header below the accelerator (Figure 23). Each of these includes a 240 liter/sec ion pump. The modules will be rough pumped by mobile roughing stations. The vacuum systems of adjacent modules are connected only at beam apertures which therefore are equipped with isolating valves.

An ultimate operating vacuum level of 10^{-7} Torr will exist in the accelerating cavities. The vacuum will be somewhat better in the header and somewhat poorer at the bridge coupler. It is anticipated that a module should be able to continue operating with any one ion pump disabled. Ion pump currents will, in general, indicate vacuum levels. This function will be augmented by ion gages to show vacuum levels near the rf window and along the header in the event of ion pump failure.

3.3.4 Support and Alignment

The installation constraints for the modules dictate that each be assembled on a portable girder. This is to accommodate rigging to a point adjacent to final tunnel location and a final short translation to the beamline position later.

The girders range from 20 feet to 30 feet in length and weigh from 8000 lbs. to 12000 lbs. approximately. The girders consist of composite weldment structures with legs (Figure 23). These are stress-relieved after welding for long term stability.

Each girder supports four sections along with the cooling water and vacuum headers, ion pumps, bridge couplers and control cabling. The girder has 6 fiducial tooling balls attached which are used to set a datum initially in the assembly area. Each section is set on the girder and aligned using its own independent supports. It is hoped that once the girder is set in the tunnel, no further adjustment of individual sections will be needed.

The girder alignment accuracy transverse to the beam (horizontal and vertical) should be ± 0.005 inch. This dictates that the adjustment slides should have fine adjustment with almost no lost motion. The section supports on the girder should provide for axial float due to thermal expansion upon start-up. A single support next to the waveguide is fixed and provides the least stress.

3.4 Linac Beam Diagnostics and Controls

The beam diagnostics in the new side-coupled linac will perform the following operations on the beam:

- a. Measure the final momentum of the 400-MeV beam,
- b. Continuously monitor the position of the beam centroid in order to correct the steering,
- c. Periodically observe the beam envelope to insure that the quadrupoles are correctly tuned, both during routine operation and during commissioning,
- d. Measure the transverse emittance in the transition section, the 400-MeV transfer line and at least once within the linac,
- e. Provide fast (5 MHz) measurement of the beam position within the beam pulse in order to observe transverse instabilities,
- f. Measure the longitudinal emittance, especially during commissioning,
- g. Provide beam-induced rf signals for the delta-t procedure.

3.4.1 Momentum Measurement

The momentum of the 400-MeV H⁻ Linac beam could not be measured by the present 40 degree spectrometer magnet (Figure 38). At a field of 16.7 kG needed to bend a 400 MeV beam, essentially all of the H⁻ beam would be stripped in the first five centimeters²³ causing radioactivity problems from the electrons. With the present magnet at 200 MeV (B=11.265 kG, L=1.33 meters), 0.2% of the beam is stripped going through the magnet. To keep the stripping for a 400-MeV beam to the same level (0.2%) the field would have to be reduced to 7.5 kG and the path length increased to 3 meters to retain the 40 degree bend. Such a magnet would be large, expensive, difficult to install and require a significant change in the transport optics. This maybe unattainable in the space required.

Use of the 40 degree momentum dump is desirable for continuous dumping of the Linac beam. The momentum dump was constructed with a larger steel casting and has an estimated dissipation of 3 to 10 kW while the straight-ahead dump has a dissipation in the range of 0.3 to 1 kW. Typical 50 mA linac pulses at 400 MeV and 15 pulses per second produce 7.2 kW, requiring the momentum dump. With pulses of once per second or less either dump is usable, but the momentum dump would still be preferred.

A possible solution is to place a thin foil in the H⁻ beam to strip to protons. By stripping the H⁻ beam before the present spectrometer, the momentum dump can still be used, allowing relative momentum and momentum spread measurements. Foils of 200 $\mu\text{gm}/\text{cm}^2$, as used at the booster injection, strip both electrons at 99% efficiency or better with an energy loss to the proton of less than 1 keV at 200 MeV. At 400 MeV the stripping cross section is reduced by a factor of 1.5 so the foil thickness should be increased to 300 $\mu\text{gm}/\text{cm}^2$ to give the same stripping efficiency. To accommodate 400-MeV protons requires increasing the power supply current from 100A to 150-200A to obtain 16.7 kG in the spectrometer. Operating the spectrometer at this level should be possible, but it must be tested for cooling.

3.4.2 Beam Steering

Beam steering in the new linac is more important than it has been for the 200-MeV linac because the beam occupies a greater fraction of the available aperture. For good steering, the linac first must be installed and aligned accurately. Alignment of the four sections and four quadrupoles on a "strongback" will lead to alignment accuracies of less than 0.1 mm through the module; careful module-to-module alignment will produce alignment errors of about 0.25 mm. These produce an average position error of 5 mm and an angle error of 0.15 mrad in the beam. The beam steering system must be able to correct this.

Steering correction is accomplished with an appropriate combination of non-intercepting Beam Position Monitors (BPM) and dipole trim steering magnets (trims). BPMs presently installed in the 200-MeV linac can resolve position differences of 25 microns. Trims capable of imparting a 1 mrad deflection are common.

The system to correct steering errors in the new linac will consist of sets of trim/BPM pairs. (This arrangement can only correct position errors; angle errors are ignored.) Space limitations between modules limit the number of places available for correction: only a correction at every other β_{\max} is possible. Since there are two FODO periods per module, there will be one correction set per plane per module in the linac, or fourteen total trim/BPM pairs. BPM's and trims which are sensitive to both planes at one location are not necessary, although adding this capability is neither significantly more expensive nor more difficult.

The implementation of an algorithm in the control system to correct steering will follow from the present Operations console program (L36). The algorithm will be debugged and initially implemented in the console environment to be run as appropriate (once a shift), and later be migrated into a local station to run at regular intervals (probably continuously).

Transverse instabilities due to a two-stream instability in the Fermilab 750 KeV transfer line connecting the Cockroft-Walton accelerator to the drift-tube linac have been observed using BPM's.²⁴ Since this instability has a 3 MHz signature, fast response in the BPM readout is necessary. Rf-induced dipole instabilities can also be observed in principle, though none has been observed to date. To facilitate this sort of measurement in the new linac, BPM's must be distributed throughout the linac. The same BPM's used for determining steering are sufficient.

The BPM has been designed to fit in as small a space as possible. For a 805 MHz bunched beam, the minimum acceptable length for the pickup is 2 cm; a longer pickup will give a larger and cleaner signal. An overall length of 3 cm has been adopted. Two prototypes are under construction. One has four very narrow plates each subtending 10° . This narrow plate gives a relatively small signal, but the overall outside diameter is small (4.01 cm OD for 3.25 cm ID, preserving a 50Ω character for the strip). The other has two wide plates each subtending 130° (5.73 cm OD). Tests are being conducted on these models and other designs are being considered.

The trim design is a small iron "picture-frame" magnet with appropriate copper wire wound around each side. These magnets can produce relatively strong (600 Gauss) and suitably uniform (2% field variation at 20% of the aperture) dipole fields, given their compact size. The trims will have approximately 4.0 cm-long iron plates and take up no more than 6.0 cm of the beam line. The trim upstream of module 3 will be slightly shorter due to limited space, and the trims near within module 2 may be slightly longer for increased steering power. The integrated magnetic field-length necessary to obtain a kick θ in a beam with momentum p is

$$\int B dl \text{ [Gauss-cm]} = 3300 p(\text{GeV}/c) \theta \text{ (mrad)}. \quad (11)$$

For a 1 mrad kick the field is 398 G at an H^- kinetic energy of 116 MeV and 531 G at 400 MeV for a 4 cm trim.

3.4.3 Beam Envelope Measurements

Accurate measurements of the beam envelope will provide information on quadrupole gradient errors, inaccurately measured drift distances and rf effects. The beam envelope is most reliably and accurately measured with a scanning wire. The information obtained from a scanning wire at every module is clearly redundant. Wires will be put only at enough locations to facilitate commissioning and to make the monitoring of the beam envelope accurate.

Seven wire scanners will be installed in the new linac: two in the transition section, one within module 1, two within module 2, and two within the last module. Since each wire will be near a waist in one plane, the transverse emittance and the twiss parameters can be easily calculated there (see Section 3.4.4).

3.4.4 Transverse Emittance Measurement

There are three commonly accepted methods for measuring transverse emittances in a linac: an emittance probe, a single wire with a tunable quadrupole and three wires in a drift space. Emittance scanners are inappropriate for energies above a few MeV and will not be considered here. Three-wire emittances are presently calculated routinely in the 200 MeV line; this procedure can be adapted directly to the 400 MeV line. The single wire with tunable quadrupole method will work well in the new side-coupled linac.

It can be shown that the following relationship holds in a quadrupole-wire arrangement:

$$\beta_f = Ak^2 + Bk + C \quad (12)$$

where A, B and C are simple linear functions of the twiss parameters β , α and γ at the quadrupole, and k is the gradient in the quadrupole.

The values of A, B and C are obtained from measuring the width of the wire for several different quadrupole gradients and fitting the results to a parabola. Of course, since the square of the beam width is equal to $\beta\epsilon$, the twiss parameters and the emittance ϵ at the quadrupole can be obtained. The measurement is most sensitive when a waist can be moved through the wire. Thus, this measurement can be performed at any focusing quadrupole which has a wire downstream of it. (This presentation ignores the effect of rf-defocusing and energy change in the accelerating module between the quadrupole and the wire.)

A conventional wire scanner has been designed with length of 5 cm to minimize the amount of space taken along the beam line. A horizontal and a vertical wire are mounted on a frame which moves in and out of the beam by a stepping motor. The wire scanners placed before modules 1 and 2 have an rf pickup plate on the far wall to facilitate the delta-t measurement.

3.4.5 Longitudinal Emittance

Measuring longitudinal emittances in a linear accelerator is difficult. The most reasonable solution is to provide for measurements of the momentum spread ($\sim\Delta E$) and of the bunch length ($\sim\Delta\phi$). Momentum spread can be measured with the 400 MeV spectrometer by turning off the rf modules downstream of the module under test and scaling the spectrometer gradient to the desired energy. Of course, this can only be done during dedicated studies time. Bunch length is most accurately measured with a device described by Feschenko and Ostroumov.²⁵ This reference also outlines a technique for using this device and a linac rf tank to directly measure the longitudinal phase space of the beam. This is being more fully investigated. Prototypes for bunch length detectors are under development.

3.4.6 Delta-t Measurement

To facilitate the delta-t procedure for setting the amplitude and phase in modules (Sections 3.2.4 and 3.6), a beam induced rf signal is needed between each module. Regular BPM's can be put between modules downstream of module 2. A different type of pickup is necessary upstream of modules 1 and 2. Since profile monitors (wire scanners) are going at these locations, specially modified wire scanners will be built to incorporate an rf pickup on the far wall of the wire chamber.

3.4.7 Linac Control System

The control system will be functionally similar to the present Linac control system. It will consist of local VME based computer stations connected via the IEEE 802.5 token ring network. These local stations will be responsible for monitoring and controlling their respective module of the accelerator. They will respond to settings and requests for data sent to them via the network. The network itself will be connected to the main accelerator control system (ACNET) via a VME based computer front end which will be responsible for protocol translation between the two networks.

The local stations will consist of a Motorola MVE 133 computer card (68020 cpu, 1 Mbyte Ram, 68881 floating point chip) or its successor, 1 Mbyte battery backed Ram, a token ring card, a utility card for interfacing to the local console, a card for interfacing to Mil-Std-1553B bus, and a local console. Binary control bits, binary input status bits, input A/D's, and output D/A's will be connected through the 1553 bus. The software will be derived from the present Linac's local station software and the local station software of the control system of the D \emptyset detector (which itself was derived from the present Linac's local station software). Much of the software for these systems is written in Pascal in such a way as to make porting (recompiling on another computer system) rather easy.

The local stations will be responsible for maintaining a data pool of device readings, scanning for alarms, inhibiting beam on certain alarm conditions, reporting alarms up the network, responding to requests for data and settings generated from ACNET or any of the

local stations, and taking care of any device that needs local intelligence (e.g. beam diagnostics). A heartbeat system in each local station will inhibit the beam if any station falls offline.

3.5 Transfer and Injection to the Booster

3.5.1 Transfer Line

The present 200-MeV transfer line (Figure 39) from the Linac to the Booster contains an electrostatic chopper and a magnetic septum to remove a portion of the linac beam and deflect it into the Booster line. This is followed by four major bends to transport the beam from the Linac to the Booster and twenty-six quadrupoles for matching and achromatic correction. Twelve horizontal and twelve vertical trim elements allow for small steering corrections. Beamline diagnostics consist of multiwires, beam current toroids, and loss monitors. At 400 MeV the momentum is approximately 50% larger than at 200 MeV (954 vs 644 MeV/c). Assuming that the basic characteristics of the present line will be retained, operation at 400 MeV will require replacement of several major elements.

3.5.1.1 Technical Problems for the 400-MeV Upgrade

The entire transfer line was evaluated on an element by element basis at 1.7 times the current operating values to assess what devices and power supplies will have to be upgraded or replaced (Table 11). The factor of 1.7 was chosen instead of 1.5 to provide an additional 20% safety margin in the upper operating range of these devices.

With this condition nine quadrupole magnets will fail and twelve quadrupole power supplies were found to deliver insufficient power. The current capability of all four dipole power supplies (for magnets MH1, MV1, MV2, and MH2) will be exceeded at 1.7 times their preset value. In addition it is not clear whether MV1 and MV2 have sufficient cooling for this new operating point. Also the increase in field combined with path length results in a considerable stripping of the H⁻ ion in MH2 (Table 12). In MH1, MV1, and MV2, H⁻ stripping will be less than 1% and stripping in the quadrupoles will be negligible.²³

200 MEV DEVICE	LENGTH (M)	APERTURE (M)	PRESENT OP. PT.	ASSUMED NEW OP.PT. (X1.5)	MAXIMUM OP. PT. (X1.7)	DEVICE OR POWER SUPPLY LIMITATIONS	
CH	1.43	0.0254	59 KV	112 KV **		CHOPPER & PS	
S1	1.04	0.0381	10.5 KA	15.8 KA	17.9 KA	MAGNET & PS	
Q6	0.2985	0.08255	28.0 A	42.0 A	47.6 A		
Q7	"	"	42.0 A	63.0 A	74.4 A	MAGNET & PS	
Q8	"	"	46.0 A	69.0 A	78.2 A	MAGNET & PS	
Q9	"	"	30.0 A	45.0 A	51.0 A	PS	
Q10	"	"	22.0 A	33.0 A	40.4 A		
MH1	0.505	0.0508	36.0 A	54.0 A	61.2 A	PS	
MV1	1.162	0.0635	230.0 A	345.0 A	391.0 A	PS	
MV2	"	"	"	"	"	PS	
Q11	0.2985	0.08255	20.0 A	30.0 A	34.0 A		
Q12	"	"	24.0 A	36.0 A	40.8 A		
Q13	"	"	15.0 A	22.5 A	25.5 A		
Q14	"	"	30.0 A	45.0 A	51.0 A	PS	
Q15	"	"	32.0 A	48.0 A	54.4 A	PS	
Q16	"	"	13.0 A	19.5 A	22.1 A		
Q17	"	"	6.00 A	9.00 A	10.2 A		
Q18	"	"	35.0 A	52.5 A	59.5 A	MAGNET & PS	
Q19	"	"	38.0 A	57.0 A	64.6 A	MAGNET & PS	
MH2	1.162	0.0635	(The magnetic field will strip the beam at 400 MEV.)				MAGNET & PS
Q20	0.2985	0.08255	44.0 A	66.0 A	74.8 A	MAGNET & PS	
Q21	0.3302	0.1026	150.0 A	225.0 A	255.0 A		
Q22	0.2985	0.08255	41.0 A	61.5 A	69.7 A	MAGNET & PS	
Q23	"	"	37.0 A	55.5 A	62.9 A	MAGNET & PS	
Q24	"	"	22.0 A	33.0 A	37.4 A		
Q25	"	"	50.0 A	75.0 A	85.0 A	MAGNET & PS	
Q26	"	"	38.0 A	57.0 A	64.6 A	MAGNET & PS	
S2	1.04	0.0381	10.0 KA	15.0 KA	17.0 KA	MAGNET & PS	
OREMP	0.96	(0.1159 X0.0572)	28.0 KA	42.0 KA	47.6 KA	MAGNET & PS	

** The Chopper is an Electrostatic device and does not scale the same as a magnet.

Table 11: 400 MeV Operating Parameters

Bending Magnet	Angle (deg)	Length (m)	Field (kG)		
			200 MeV	400 MeV	at 400 MeV for Stripping<0.1%
MH1	5.925	.495	4.49	6.65	7.9
MV1	-12.83	1.16	4.14	6.13	7.6
MV2	12.83	1.16	4.14	6.13	7.6
MH2	-24.62	1.11	8.31	12.3	7.6

Table 12: Bending Magnet Parameters

The plates of the electrostatic chopper (CH) are 143 cm long, separated by 2.54 cm, and can operate up to 80 kV. Reducing the separation or increasing the voltage is impractical because of electrical breakdown. For 400-MeV operation, the electrostatic

chopper would be required to run at 112 kV to give the same beam deflection. The septum (S1) is 104 cm long and operates at a field of 3.2 kG (9900 A, pulsed). The septum is not watercooled and cannot operate at the 400-MeV operating point of 4.8 kG. For this reason a new septum is unavoidable. In addition its pulsed power supply will not reach 1.5 times the present current.

3.5.1.2 Magnets

With regard to the problems outlined in the previous section, several options are open with regards to the quadrupoles needed for the 400-MeV Upgrade. Those under consideration are:

1. Connect the cooling paths in parallel instead of series on the 200-MeV quadrupole coils.
2. Build new coils for the 200-MeV quadrupoles with improved cooling.
3. Replace magnets with quadrupoles developed for the Loma Linda medical accelerator.²⁶

Since all the 200-MeV quadrupoles have their coil cooling in series, a simple manifold change can put all the coils in parallel. These coils use a cooling plate placed among stacks of conductor. Running at the highest currents needed for 400-MeV operation (75-85 amps) will cause localized hot spots and eventually cause the magnets to fail. The maximum power dissipation with a parallel cooling system needs to be studied in more detail. Some new power supplies will be needed but not as many as required for the other options. The 200-MeV quadrupoles have a history of steering and magnetic alignment problems and should not be used unless tests prove they will work. Extensive tests are underway at the Magnet Test Facility to determine the field quality and saturation characteristics of these quadrupoles.

New coils with improved cooling can be designed and installed in the old quadrupole carcasses. Hollow conductor of diameter .229 inch would be used in this case, and the number of turns that could be fit into the present carcass would be down by at least a factor of two. The corresponding increase in current will mean that new power supplies will have to be purchased. However new coils may not be any more cost effective than the third solution if, as expected, new magnet stands will have to be built in order to align the beamline properly.

The quadrupoles being produced for the Loma Linda medical accelerator could replace the 200-MeV quadrupoles that require currents in excess of their present capability at 400 MeV. The 3.25 inch bore and 10 inch length duplicate physically the 200-MeV quadrupoles, yet they can maintain a field gradient of 3.4 kG/inch as opposed to the 2.4 kG/inch maximum gradient of the present quadrupoles. These quadrupoles can be used as replacements for all of the quads with problems in the 400-MeV Upgrade. Also, in reviewing specifications and measurements on both types of quadrupoles, the field uniformity, hysteresis, and saturation characteristics were found to be better in the Loma Linda quadrupoles than in the existing 200-MeV quadrupoles. New power supplies will have to be purchased. Technically the preferred solution is to use the Loma Linda quadrupoles for the transfer line.

All dipoles in the transfer line will need new power supplies. MV1 and MV2 will have to undergo temperature tests at the new operating point to determine their adequacy. Because of H⁻ stripping, MH2 will have to be replaced by a magnet 50-70% longer to decrease the field sufficiently to preserve the H⁻ beam.

3.5.1.3 Chopper and Septum

A new chopper entails constructing a complete new enclosure and plates. Little if anything could be salvaged from the existing chopper because of residual beam-induced radioactivity. Instead of rebuilding the electrostatic chopper, which is reliable and works well, it can be moved upstream since the new linac will be shorter than the existing linac by about four meters. Beam transport calculations indicate that the chopper should be moved upstream of its present location by about a meter. In this position the chopper will work at its present operating voltage. Neither the magnet nor the power supply need to be modified for the Upgrade.

A pulsed, water-cooled septum that has been used successfully in the 8-GeV line can be essentially copied for the 400-MeV transfer line upgrade. This septum incorporated a better structural and field design than the one used in the present transfer line. The new septum will have to be 50% longer. Because this implies a 50% greater inductance, a new pulsed power supply will have to be built.

A shorter (1 meter), stronger DC septum is being investigated as an alternative to a pulsed system. Extra beamline space would not be required and the magnet would be cheaper to build and more reliable to operate. A DC power supply can be bought cheaply and is also more reliable. Using POISSON, a DC septum has been designed which has good field quality and is capable of an 8 to 12 degree bend at 400 MeV. This corresponds to a field of 4.5 to 6.5 kG. It is desirable that the new septum work for injection as well so a study is continuing to minimize fields in the zero-field region.

3.5.1.4 Transfer Line Optics

In the 200-MeV transfer line (Figure 39) there are three achromatic bends. The achromatic property is local in each bend and does not depend on the characteristics of the beam but only on the relative strengths of the magnets in the bend.

The first achromatic bend is a horizontal one made up of the chopper, Q1, S1, Q6 and MH1 and serves to separate the transfer line from the straight-ahead linac diagnostic line. Q1 does the vertical focusing in this section of the line and Q6 performs momentum recombination for the bend.

The next bend is a vertical translation which projects the beam down a vertical chute to the level of the Booster synchrotron. Two identical, 12.8 degree magnets, MV1 and MV2 are used. Quadrupoles 9-12 provide the focusing and make the bend achromatic. Q7 and Q8 perform matching between the first horizontal bend and this vertical one.

The final horizontal deflection is used for injection into the Booster and is accomplished with MH2 and S2. Q13-19 are used to match the beam to the transverse acceptance of the Booster and provide focusing in the long drift space up to the debuncher. The final quadrupoles in the line, Q20-26, are tuned for dispersion matching into the Booster.

Beam transport simulations of the transfer line have begun. So far the basic characteristics of the 200-MeV transfer line have been satisfactorily reproduced using TRANSPORT. Lattice functions and trajectories appear to be consistent with beam profiles taken with the twelve multiwires situated along the existing line. This TRANSPORT deck has since been modified to predict the optics of a 400-MeV beam, assuming that some of the basic attributes of the 200-MeV line will be retained. The new 400-MeV transfer line is being designed with a 30π acceptance (95%). Two solutions for the first achromatic horizontal bend have been found and both involve moving the chopper upstream of its present location by approximately a meter. One solution maintains the position and scales the strength of Q1 but varies the position and strength of S1. The other solution in addition allows the position and strength of Q1 to vary. Several quadrupoles will also have to be situated between the chopper and the end of the linac to focus the beam at the septum.

3.5.1.5 Diagnostics Transfer Line

Figure 39 shows the location of the present transfer-line diagnostics. Some of these diagnostics will need to be upgraded. BPM's will also be added to each of the 12 multiwires to assist in tuning the 400-MeV beam.

The ferrofluidic feedthroughs currently being used on the multiwires produce a field with a dipole component of greater than 20 Gauss in the vicinity of the beam. In addition the shelf life of these feedthroughs has expired so they can be expected to start leaking in the near future which makes replacement imperative. The feedthroughs can be modified with shaft extenders to virtually eliminate their effect on the line.

3.5.2 Debuncher for Booster Injection

The longitudinal phase space area of the Booster beam is proportional to the energy spread of the Linac bunches. This is because all Linac bunches are "debunched" during the first 30 revolutions or so, and the resulting unbunched beam is captured into the usual 84 bunches by the Booster rf. This debunching process is not adiabatic and the phase space area of the final unbunched beam is not the sum of the areas of

the individual Linac bunches. Consequently a debuncher which reduces the energy spread by rotating the phase space ellipse of each Linac bunch is essential to reduce the longitudinal phase space area of the resulting Booster beam.

The present 201.25 MHz debuncher is located approximately 40m from the end of the Linac. This location is also satisfactory for the new 805 MHz debuncher if the longitudinal emittance is the 26π keV/nsec which recent measurements indicate. For larger longitudinal emittance it is better to move the debuncher farther upstream. A suitable alternate location is about 27 cm from the end of the SC linac and between Q12 and MV2, just after the transport line reaches the level of the Booster tunnel. Bunches of 80 keV-nsec phase space area drift to a phase width of $\pm 60^\circ$ where a four-cell SC debuncher section with a gradient of approximately 2.4 MV/m reduces the energy spread to less than 250 keV. The phase space ellipse plots in Figure 40 show the beam phase space in all three coordinates at the end of the SC linac and at the Booster stripping foil as calculated by TRACE-3D.

3.5.3 Injection into the Booster

Figure 41 shows the layout of the present H⁻ injection system. Like the transfer line, the present H⁻ charge-exchange injection system, located in the six-meter straight section (LONG-1) requires no fundamental design changes. However, scaling the design to the new momentum necessitates replacement of some components.

3.5.3.1 Injection Septum and Orbumps

The problems described with the transfer-line septum also apply to the injection septum. The design of an injection DC septum is more critical because the circulating Booster beam passes continuously through the "zero-field" region of the septum. The impact of residual fields effectively integrate over the 16,000 turns made by the Booster beam before extraction. The design of the septum pole faces have been refined to the extent that only 5 Gauss remains in the region of the circulating proton beam (Figure 42). With this design, a DC septum with its increased reliability factor as compared with a pulsed septum appears feasible.

For the 400-MeV Upgrade, the present "orbump" magnets (orbit-bump magnets: pulsed back-to-back dipoles) and power supplies cannot be run at 50% above their present capabilities. A new pulsed power supply would be costly. Since the beam size adiabatically shrinks from 200 to 400 MeV, the stripping foil can be located about 20% closer to the centroid of the circulating beam. By moving the foil, increasing the orbump length by 10%, and decreasing its horizontal aperture, the required current and inductance will remain the same. (The required increase in length is 10% rather than 20% because the displacement at the foil scales as the square of the length; one power for the added integrated strength and one power for the added lever arm.) If these changes are implemented, the present power supply can be used.

To make access easier, our plan is to separate the individual elements on the new injection girder (Figure 43) instead of enclosing them in a common coffin as was done on the present girder. A smaller less complex foil changer is envisioned to create the needed space on the girder. Additional space may be gained by moving the septum magnet upstream.

3.5.3.2 H⁻ Stripping Foil

The effects of the stripping foil on the beam depend on the energy. The important stripping cross sections decrease by about a factor of 1.5 from 200 to 400 MeV. The present carbon foil which is 200 $\mu\text{gm}/\text{cm}$, converts H⁻ to H⁺ with an efficiency of about 99%. A thickness of about 300 $\mu\text{gm}/\text{cm}$ will give the same conversion efficiency at 400 MeV. Emittance growth scales linearly with the thickness and inversely with momentum. The emittance growth for a 300 $\mu\text{gm}/\text{cm}$ foil at 400 MeV should be approximately 20% smaller than for 200 $\mu\text{gm}/\text{cm}$ at 200 MeV.

3.5.3.3 Injection Diagnostics

Figure 43 shows the diagnostics to be installed between the elements on the injection girder (which include the injection septum, the upstream orbump, the foil, and the downstream orbump). These will permit us to measure injection positions and angles for matching and tuning purposes. The general set of diagnostics planned for the girder includes a revolution frequency BPM paired to a single wire scanner.

3.6 Installation and Commissioning

The new side-coupled modules and rf power systems will be installed with only minor disruptions in the operating schedule of the present 200-MeV linac. The 200 MeV tunnel access doors, buried after the original linac was completed, will be reopened to facilitate installation of the new accelerator modules and removal of the 200 MHz drift-tube tanks. The new modules can then be installed in the linac enclosure during short maintenance and development periods without disturbing the operating systems. Initially, the new modules will be positioned on the west side of the linac enclosure parallel to the existing linac (Figure 44). Waveguides, utilities, and instrumentation cables will be connected to the modules in this temporary location. Unused penetrations in the shield wall between the linac enclosure and the gallery basement already exist for routing drive power, water, and diagnostics signals. The length of the seven new modules and transition section will be the same total length as the drift-tube tanks that they replace.

The new klystron power supplies will be installed, initially, in space adjacent to the existing 200 MHz power supplies. Two options exist for the location of the supplies. The first option would locate klystron supplies in a building expansion east of the present linac gallery (Figure 45). This option provides ample space for klystron placement and the least perturbation to existing office and laboratory space. The second option would locate klystron supplies in the linac gallery without any new civil construction (Figure 46). To create sufficient space, existing office and laboratory areas would be removed along the east wall of the linac gallery. Less freedom exists in component placement and interconnections under this option. Since no new space has been created, the areas removed would have to be relocated into existing space, leading to greater crowding. The advantages of this option are that klystron installation does not depend upon potentially lengthy civil construction, and that it is less expensive.

With the klystron power supplies and the new linac modules in their temporary locations, the modules can be conditioned and run at full gradient without interrupting the operation of the 200 MeV

linac. At this time, computer control and monitor systems will be brought on-line and tested to the maximum extent possible without beam. When the temporary installation is complete, all seven modules will be operated and maintained at full gradient until the extended shut-down for final module positioning. All systems will be fully operational at this point.

During the extended shut-down, approximately a two month period, the drift-tube tanks 6-9 will be removed, and the new SC modules are moved laterally onto the beamline. At the same time, modifications are made to the beam diagnostics area and the transport and injection system to the Booster. The systems are then commissioned at the higher energy of approximately 400 MeV.

After the initial commissioning period, the four unused 201.25 MHz power supplies at the high energy end of the Linac will be removed from the linac gallery. The seven 805 MHz power supplies will then be moved into the space now occupied by the 201.25 MHz hardware. A layout of the power supplies in their final position is shown in Figure 47. In this position, prime space in the east half of the linac hall is recovered, and the distance between the klystrons and the modules they power can be minimized. Minimizing the signal paths permits improvements in the regulation of the feedback systems. The movement of the power supplies will be accomplished during short maintenance and development periods.

To minimize the time required to move each power supply, a special sequence of moves is planned which uses the spare (eighth) power supply. According to this plan, the spare supply will be installed at the end of the linac hall in a final position in the west half of the linac hall. The other seven power supplies will remain in operation in their temporary locations until the eighth rf supply is thoroughly commissioned in the final supply location using dummy loads. During a brief linac shut-down period, re-routing of waveguides and cables from the seventh accelerating module to the spare power supply will take place. There will be no need to move large pieces of hardware during the brief shut-down under this plan. The power supply which has been turned off is now available to move to the next final position down the linac hall while the linac resumes operation. While the components for the non-operating power

supplies are available for use as spares, the supplies cannot be maintained continuously as a hot spares until all power supplies are in their final positions against the west half of the linac hall.

The prototype rf power system (Section 3.2.5) will be installed just north of building column 15 next to the existing 200 MHz spare rf station (Figure 46). It will be thoroughly tested at full power in this location before additional klystrons are commissioned. The prototype accelerator module will be conditioned and tested to full power using this supply. The prototype module (Section 3.1.6) could possibly be located either in the basement area beneath the klystron or in nearby laboratory space. X-ray shielding requirements will be determined from tests on an experimental 6-cell side-coupled structure which will be operated at a gradient equal to or greater than that for the prototype module.

Once the new accelerator modules have been moved onto the beamline and fully tested at full gradient without beam, commissioning with beam will take place over a period of several weeks. Initially, the beam current, pulse duration, and pulse repetition rate will be set to the minimum required to diagnose beam properties. This action will minimize the risk of damaging beam-line components during initial accelerator adjustment. Before rf power is applied to the structure, the quadrupole fields will be set to nominal values. Beam loss along the length of the accelerator will be checked using beamline current monitors.

The amplitude and phase in the transition section bunchers (Section 3.1.5) will be set to calculated values by scanning the phase in each of the two buncher sections and observing the change in energy. The energy change can be measured using either the momentum analyser at the end of the linac or a time of flight technique. The proper phase setting will lie midway between the maximum and minimum energies as phase is varied. The electric field value can be determined from the difference between maximum and minimum energies. The bunch width of the beam exiting the transition section will be checked after the transition section has been adjusted and before the accelerator modules are powered. This measurement will be accomplished either by a de-convolution of BPM signals induced by individual beam bunches, or using a secondary beam analysis technique similar to that described in Ref. 21.

In order to properly set the amplitude and phase of the accelerator modules, we propose to use the "delta-t procedure" developed at the Los Alamos National Laboratory, and used extensively on the accelerator for LAMPF.²¹ The method involves measuring changes in the times of flight for particle bunches through successive modules as the rf power applied to the module being tuned is alternately turned on and off. The times of flight are measured by a phase comparison technique. Beam induced signals will be monitored in the spaces between modules. Coarse settings of phase will be determined using measurements of beam loading as phase is varied. Coarse setting of amplitude will be determined from forward power measurements combined with SUPERFISH calculations of cavity fields on axis. A second method to determine the module field and phase settings involves measuring and optimizing the energy spectrum obtained in the momentum analyser at the end of the linac as power is applied to each module. Results of this alternate measurement will be used to corroborate the delta-t measurements.

3.7 Conventional Construction

The new klystron power supplies will be installed in the linac gallery. Initially, the new klystrons will be located in space adjacent to the existing supplies along the east side of the gallery. This is necessary to maintain the existing 200-MeV linac in operation throughout the construction period. After completion of the 400 MeV linac commissioning phase, the old klystrons for the last four tanks of the drift tube linac will be decommissioned and removed, and the new klystrons and power supplies will be relocated, one at a time, on the west side of the gallery. The locations of the new klystrons in both their initial and final configurations are shown in Figs 45-47. It should be noted that two alternatives are being studied for the initial configuration of the new klystrons. The first, shown in Fig 45 is designed to locate the supplies without requiring a reconfiguration of the Neutron Therapy Facility (NTF) pre-treatment area. This solution, however, requires the construction of new space for the klystrons and modulators, and also requires relatively long rf waveguides. A second solution, shown in Figure 46 is also being studied. This solution does not require an

enlargement of the building for the purpose of the initial (temporary) location of klystrons and power supplies. This solution, however, does require the relocation of some of the NTF patient consultation and pre-treatment rooms. The relative costs and benefits of these two solutions are still under review.

In either of the proposed solutions for the initial location of the klystrons, existing office areas and tech support space are absorbed into the klystron space, as well as the NTF space mentioned above for the second solution. To recover this space, and to provide technician work space, office space, room for system staging, a two story building addition is proposed. Included in this addition is space for mechanical equipment for the building and toilets. Partitions are included only around power supplies, toilets, and mechanical equipment. Open planning is used for the office and tech work spaces similar to many other existing areas at Fermilab. Building modifications will be designed according to DOE Order 6430.1.

Unless test areas with sufficient hard X-Ray shielding to permit operation of the new modules at full power are provided, the only full power testing possible will be conducted inside the linac enclosure. This may prove inconvenient, especially in the early stages, and consideration is now being given to the possibility of providing sufficient shielding in an accessible location for full power tests. Studies for the staging of inventory, subassembly construction, testing, and final assembly are now underway. These studies have already revealed that space will be at a relative premium, and motivated the second solution above for initial klystron placement which maximizes ground floor space available during the early critical stages of inventory management and subassembly.

Additional utilities will be required to operate the new systems, especially during parallel operation with the existing 200 MeV linac. Two new 1.5 MVA substations with a new high voltage feeder and switch will supply power for both the new systems as well as for the new office/tech work space. Additional capacity will be provided for the existing Linac low conductivity water (LCW) cooling systems. Fire detection and suppression systems for both equipment and building space will be provided. Ventilation of the

new power supply equipment and HVAC for the new building space are included.

The construction of the new building space will be done so as to minimize impact on the operating schedule of the present 200-MeV linac. Very substantial temporary barriers, dust partitions, and roof covering will be installed at the start of the job. The present wall and precast fascia will be removed as necessary and a new roof structure installed. Special precautions with approved techniques will be used for the removal of existing asbestos insulation on concrete fascia panels that are to be removed. Heavy shoring under existing precast panels and roof trusses will be installed so that removal and demolition may be accomplished with minimum disruption to operations. Electrical and cooling system additions will be installed and tested and connected on line with minimal outages.

References

1. L.J. Laslett, "On Intensity Limits Imposed by the Transverse Space-Charge Effects in Circular Accelerators", in BNL-7534, p. 324. (1963).
2. L.M. Young and J.M. Potter, "CW Side-Coupled Linac for the Los Alamos/NBS Racetrack Microtron", IEEE Trans. Nuc. Sci., NS-30, No. 4, pg. 3508 (1983). E.A. Knapp, B.C. Knapp and J.M. Potter, "Standing Wave High Energy Linear Accelerator Structures", Rev. Sci. Inst., 39, Number 7, p. 979 (1968).
3. V.D. Burlakov, et al, "Status of the Construction of the INR Meson Factory", Proc. of the 1984 Linear Accelerator Conference, GSI, Darmstadt, GSI-84-11, pg. 9-13 (1984).
4. V.K. Grishin, et al, "Computer Simulation of the RF Properties and Thermal Conditions of the Disk-and-Washer Accelerating Structure for the Racetrack Microtron", Nuc. Inst. and Methods in Phys. Res. A255, pgs 431-436 (1987).
5. S. Inagaki, "Disk-and-Washer Cavities for an Accelerator", Nuc. Inst. and Methods in Phys. Res. A251 (1986) pgs. 47-436.

6. A. Moretti, et al, "An 805 MHz Disk and Washer Structure for the Fermilab Linac Upgrade", Fermilab-Conf-88/145 (1988) (to be published in the Proc. of the 1988 Linear Accel. Conf.).
7. R.J. Noble, "Acceleration Gradient for the 400-MeV Linac Upgrade", Fermilab TM-1448 (1987).
8. W.D. Kilpatrick, "Criterion for Vacuum Sparking Designed to Include Both RF and DC", Rev. Sci. Inst. 28, 824 (1957).
9. R.M. Hutcheon et al, "Operation of a CW High Power RFQ Test Cavity: The CRNL Sparker", Proc. of the 1984 Linac Conf. (GSI-84-11), p. 74. See also S.O. Schriber, "Factors Limiting the Operation of Structures under High Gradient", Proc. of the 1986 Linear Accel. Conf., Stanford, CA, p. 591.
10. R. Lehmann, "Experiments with an RFQ Sparker", Particle Accel. 22, 161 (1987).
11. C.W. Owen, C.A. Radner and D.E. Young, "High Field Measurements at 200 MHz in Conventional Linear Accelerator Geometries at 5,50, and 130 MeV", Proc. of the 1966 Linear Accel. Conf., LANL-8, 3609, Pgs. 176-182 (1966).
12. T.G. Jurgens, Q.A. Kerns, J.R. Fritz and M.A. May, "An Alternate Side Coupled Structure for the Fermilab Linac Upgrade", 1988 Linear Accelerator Conference (Williamsburg, VA, October 3-7, 1988).
13. L.M. Young, LANL, private communication.
14. T. Weiland, "Computer Modelling of Two and Three-Dimensional Cavities, "IEEE Trans. Nucl. Sci. NS-32, 2738 (1985). M.J. Browman, R. Cooper, and T. Weiland, "Three-Dimensional Cavity Calculations", Proc. of the 1986 Linear Accel. Conf., SLAC, 1986.
15. J.M. Potter and E.A. Knapp, "Bridge Coupler Design and Tuning Experience at Los Alamos", Proc. of the 1972 Linear Accel. Conf. (Los Alamos), p. 242. G.R. Swain, "LAMPF 805-MHz Accelerator Structure Tuning and It's Relation to Fabrication and Installation", Los Alamos Report LA-7915-MS (1979).

16. R.K. Cooper et al, "Radio-Frequency Structure Development for the Los Alamos/NBS Racetrack Microtron", Los Alamos Report LA-UR-83-95 (1983).
17. K.R. Crandall, "TRACE 3-D Documentation", LANL report LA-11054-MS (August, 1987).
18. R. Jameson, "Beam Intensity Limitations in Linear Accelerators", IEEE Trans. Nucl. Sci. NS-28, No. 3, 2048 (1981).
19. T. Owens and O.A. Calvo, "Feedback Control of the Upgraded Linac at Fermilab", 1989 Particle Accelerator Conference (Chicago, Ill., March 1989).
20. J.E. Marshall, Control of the Time-Delay Systems, IEEE Control Engineering Series (1979).
21. K.R. Crandall, "The Δt Tuneup Procedure for the LAMPF 805-MHz Linac", Los Alamos Scientific Laboratory Report LA-6374-MS, June 1976.
22. A.S. Gilmour Jr., Microwave Tubes, p. 229 (Artech House, Norwood, MA, 1986).
23. A.J. Jason, D.W. Hudgins, O. van Dyck, W. Faulkner and D.A. Clark, "H- Field Detachment", LA-UR-81-1257 (1981).
24. E. McCrory et al, "Observation of Transverse Instabilities in the FNAL 200 MeV Linac", 1988 Linear Accel. Conf. (Williamsburg, VA, October 3-7, 1988).
25. A.V. Feschenko and P.N. Ostroumov, "Bunch Shape Measuring Technique and its Application for an Ion Linac Tuning", Proc. of the 1986 Linear Accel. Conf., Stanford, CA, p. 323.
26. Everson Electric Co. quadrupoles, Bethlehem, Penn.

Appendix A

Tevatron Upgrade - Linac Schedule

APPENDIX A

FERMILAB LINAC UPGRADE

ACTIVITY	FY	89	90	91	92	
	CY	1989	1990	1991	1992	
<u>MILESTONES</u>		①②	③	④		⑤⑥
<u>R & D & PREOPERATING</u>						
PROTO SC ACCEL STRUC		DESIGN	PRO	FABRICATE	TEST	PREOP
PROTO RF SYSTEM		DESIGN	PRO&FAB	TEST		PREOP
<u>CONSTRUCTION</u>						
CONVENT. CONSTR. (H)			DES	BID	CONSTR.	
RF SYSTEMS (B)			DE	PRO	FABRICA	1 2 3 4 5 6 7
SC MODULES (A,C,F)					TEST	COM
AUXILLARY SYSTEMS (D,E,G)				DES & PRO	CONSTR.	1 2 3 4 5 6 7
					TEST	COM
		DESIGN	PRO	FABRICATE	TEST	COM

No.	Milestone	Date
1	Start Project	October 1, 1989
2	Specify RF System	November 15, 1989
3	B.O. of Power Supply Gallery	September 30, 1990
4	Full Power Test of 1st Module	June 1, 1991
5	Conversion to 400-Mev Injector	September 1, 1992
6	Complete Project	September 30, 1992

Appendix B

Tevatron Upgrade - Linac Cost Estimate

FERMILAB LINAC UPGRADE - LINAC COST ESTIMATE
(FY-1989 K\$)

A.	SCS Accelerator Cavity Systems	<u>5,585</u>
A.1	Accelerating cavities including brazing (28 sections)	3,520
A.2	Tuning lab	230
A.3	RF feed cells (21 units)	425
A.4	Quadrupoles w/P.S. (32)	170
A.5	Beam diagnostics	320
A.6	Stands	190
A.7	Cooling system	140
A.8	Vacuum	340
A.9	Installation	250
B.	RF Power Supply Systems	<u>5,245</u>
B.1	Power supply and filters (8 units)	560
B.2	Pulse forming networks (8 units)	1,250
B.3	Klystron w/solenoid, oil tank, transformer (8 units)	2,005
B.4	Transmission waveguide	900
B.5	Controls and interlocks	320
B.6	Dummy load and test equipment	50
B.7	Installation	160
C.	Transition Section	<u>1,120</u>
C.1	RF cavities including brazing (4 sections, 52 cells)	480
C.2	Tuning lab	20
C.3	RF power supply	385
C.4	RF feed cells	80
C.5	Quadrupoles w/PS (6)	30
C.6	Beam diagnostics	30
C.7	Stands	20
C.8	Cooling system	15
C.9	Vacuum	30
C.10	Installation	30

D.	Linac 400-MeV Beam Diagnostics	<u>110</u>
	D.1 Stripping equipment	20
	D.2 Beam position, profile, and intensity monitors	40
	D.3 Powers supply replacement	50
E.	Booster Transfer Line	<u>380</u>
	E.1 Replace MH-2	30
	E.2 Chopper	15
	E.3 Septum replacement	20
	E.4 Quadrupole coil replacement	50
	E.5 New steering elements w/PS (10 units)	50
	E.6 New power supplies	140
	E.7 Diagnostics and controls	35
	E.8 Installation	40
F.	Debuncher for Booster Injection	<u>635</u>
	F.1 Cavities, supports, vacuum (4 cells)	210
	F.2 RF power supply	385
	F.3 Controls	30
	F.4 Installation	10
G.	Injection into Booster	<u>230</u>
	G.1 Stripper	10
	G.2 Septum	20
	G.3 New orbumps	50
	G.4 Septum power supply	40
	G.5 Mechanical, vacuum, water	40
	G.6 Installation	70

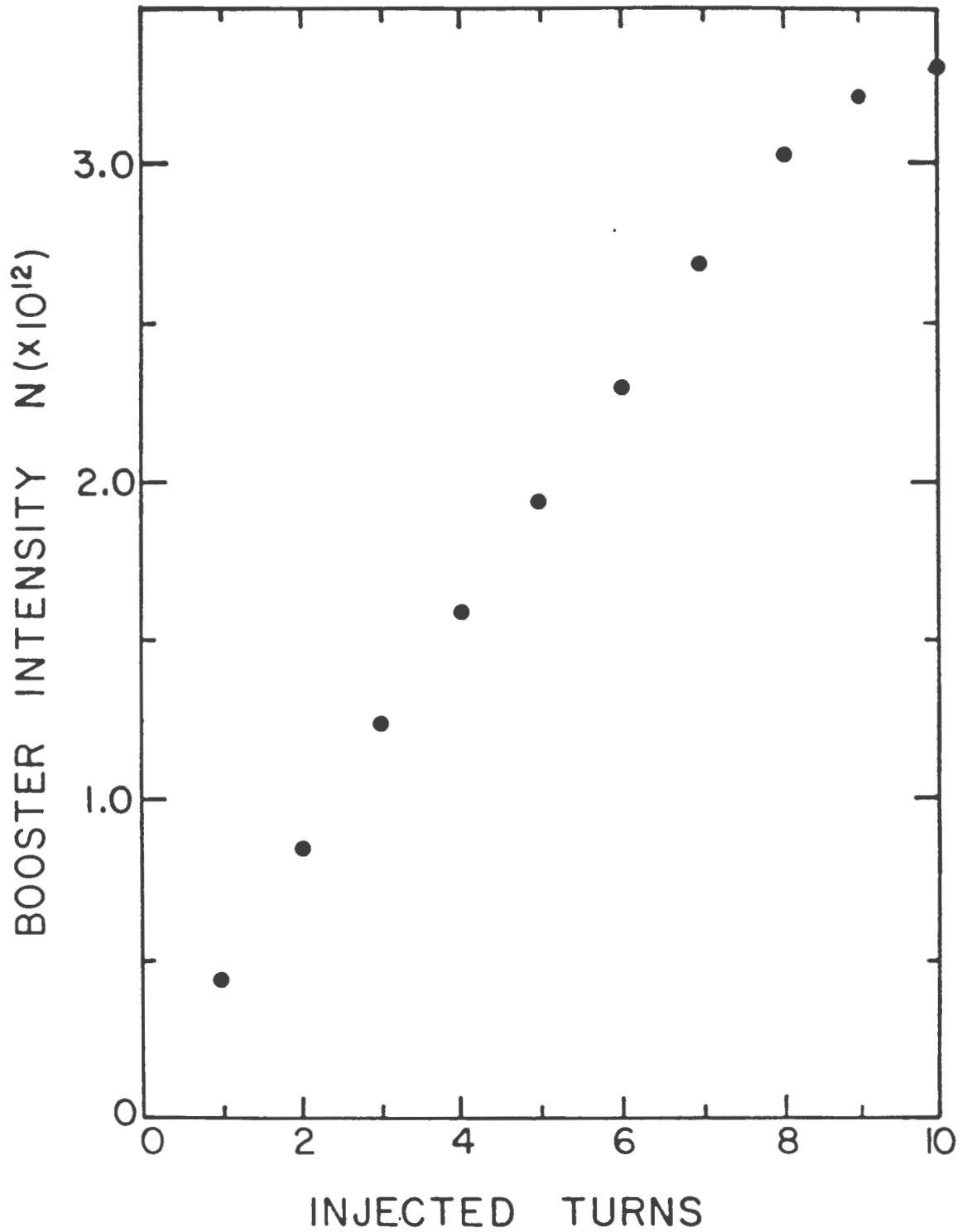
H. Building Modifications	<u>1,630</u>
H.1 Sitework, earth work, paving	120
H.2 Demolition and protection	160
H.3 Concrete foundations	150
H.4 Structural and misc steel	190
H.5 Precast concrete walls, panels and blocks	130
H.6 Roof closures, partitions, windows and doors	140
H.7 HVAC and process piping	200
H.8 Cooling system rf power supplies	60
H.9 Electrical substation (13.8 Kv)	90
H.10 Electrical distribution	190
H.11 Fire Protection and plumbing	200
 Total Construction Costs	 14,935
Engineering, Design, Inspection and Administration ⁽¹⁾ (16% of M&S)	<u>2,390</u>
	17,325
Contingency (19% of above costs)	<u>3,240</u>
	20,565
Incremental Overhead ⁽²⁾	<u>140</u>
	20,705
 Escalation ⁽³⁾	 1,830
 Total Estimated Cost in Then-Year K\$	 <u><u>22,535</u></u>

(1) Administration costs include Fermilab project management costs.

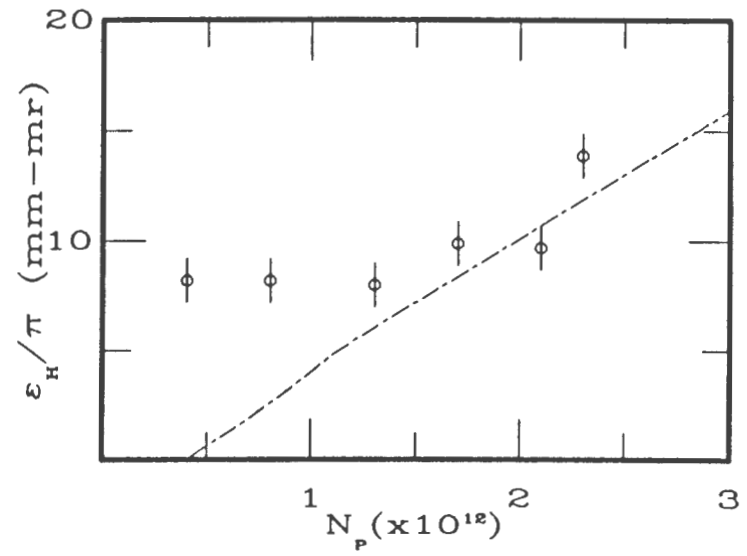
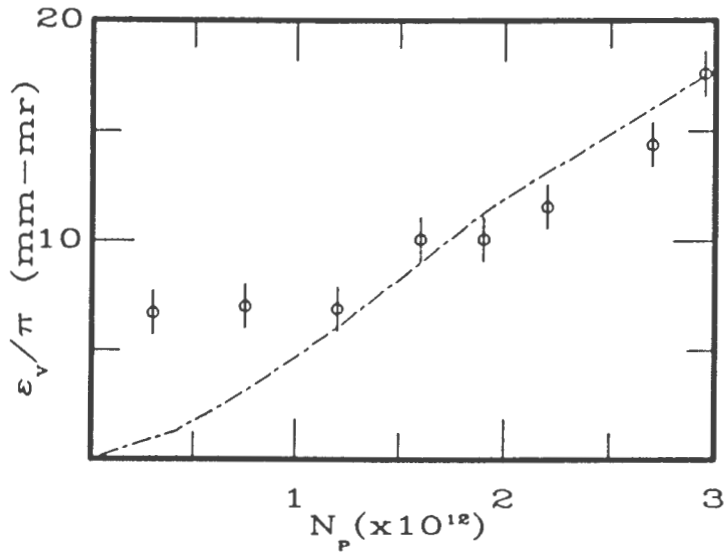
(2) Included in this category are the incremental support from the Fermilab Business and Services Section and for the purpose of the cost estimate is taken as 0.7%.

(3) Using DOE escalation rates.

Figure 1



BOOSTER INTENSITY VS. NUMBER
OF INJECTED TURNS



----- $\Delta\nu_{sc} = 0.38$

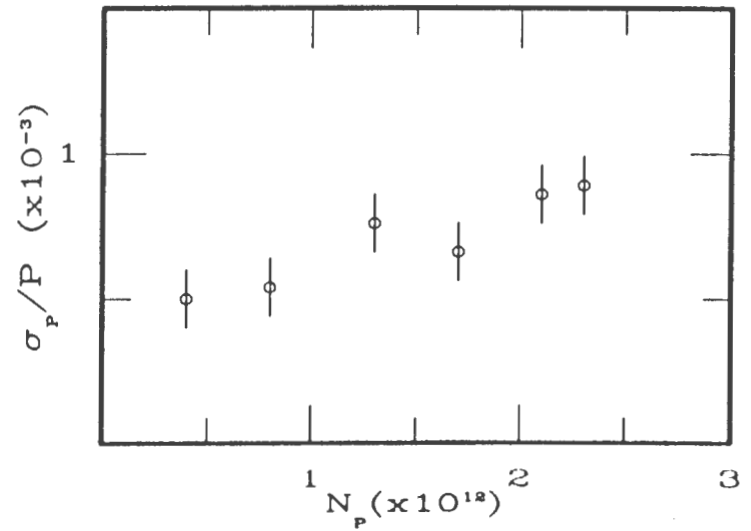


Figure 2 - Booster emittance and momentum spread vs. intensity showing growth at higher intensities.

BOOSTER EMITTANCE vs. INTENSITY

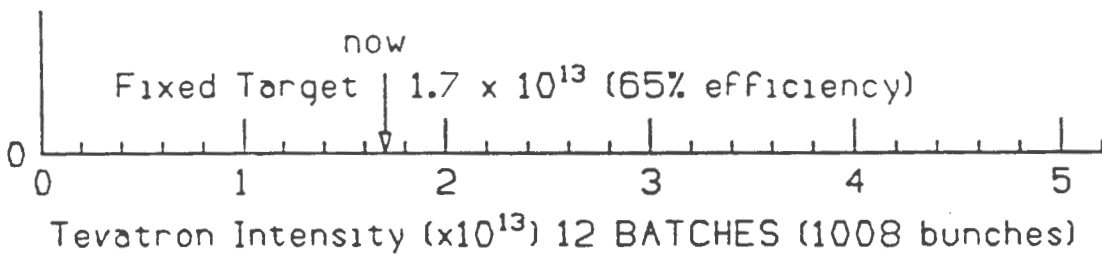
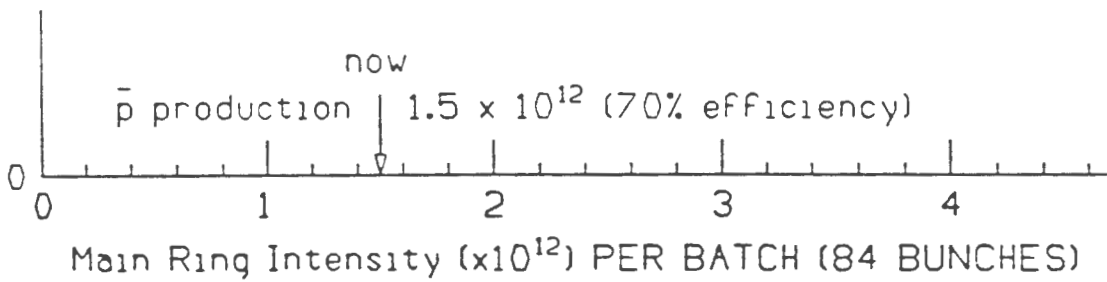
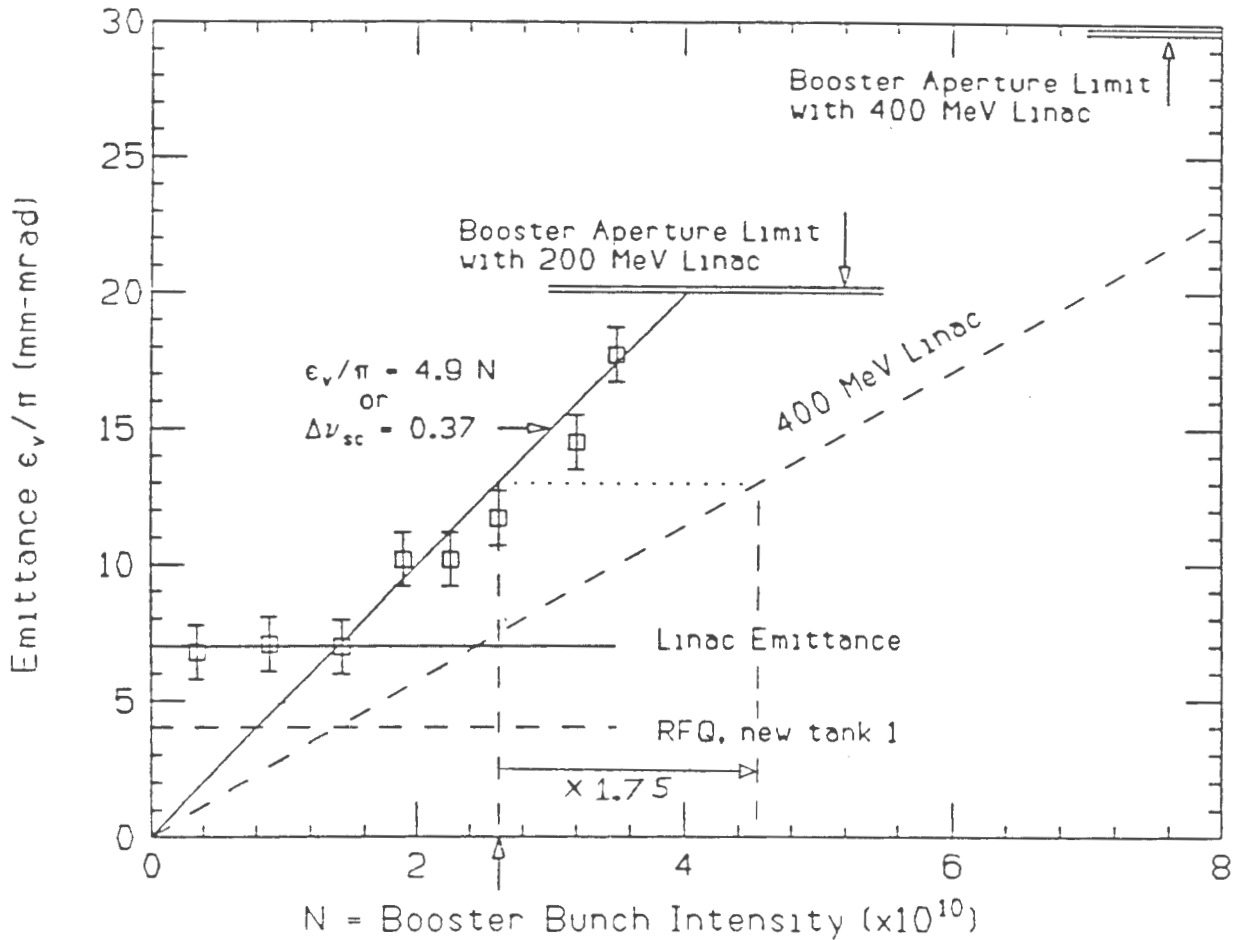
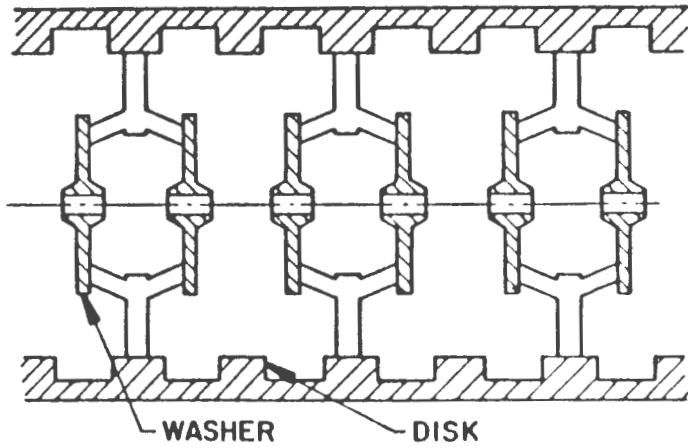
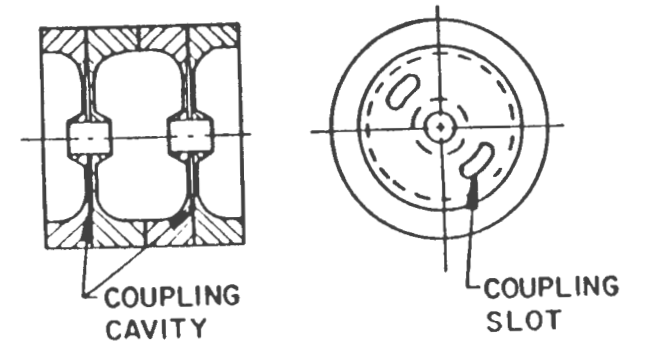


Figure 3

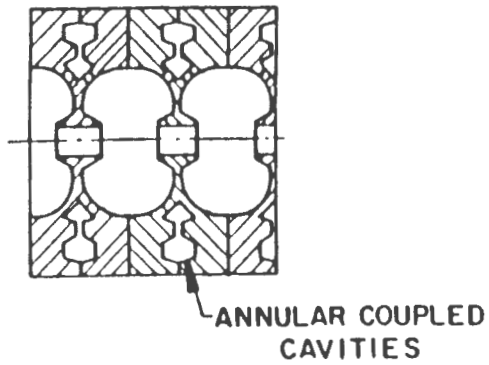
DISK AND WASHER



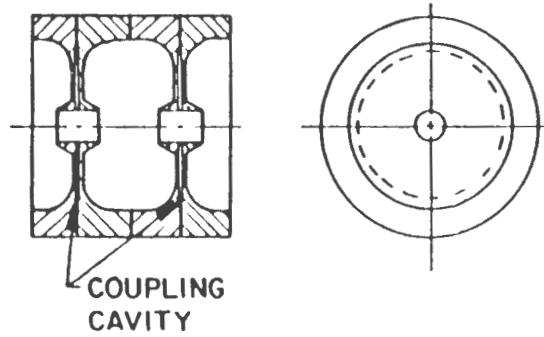
COAXIAL COUPLED



ANNULAR COUPLED



ON AXIS COUPLED



SIDE COUPLED

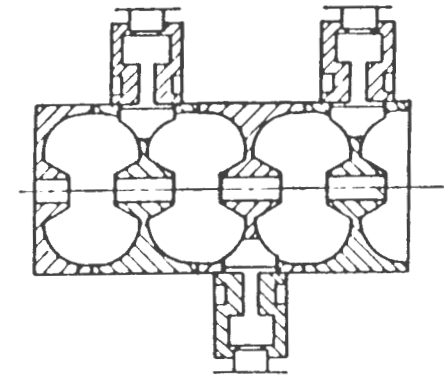


Figure 4 - Five types of standing wave accelerating structures

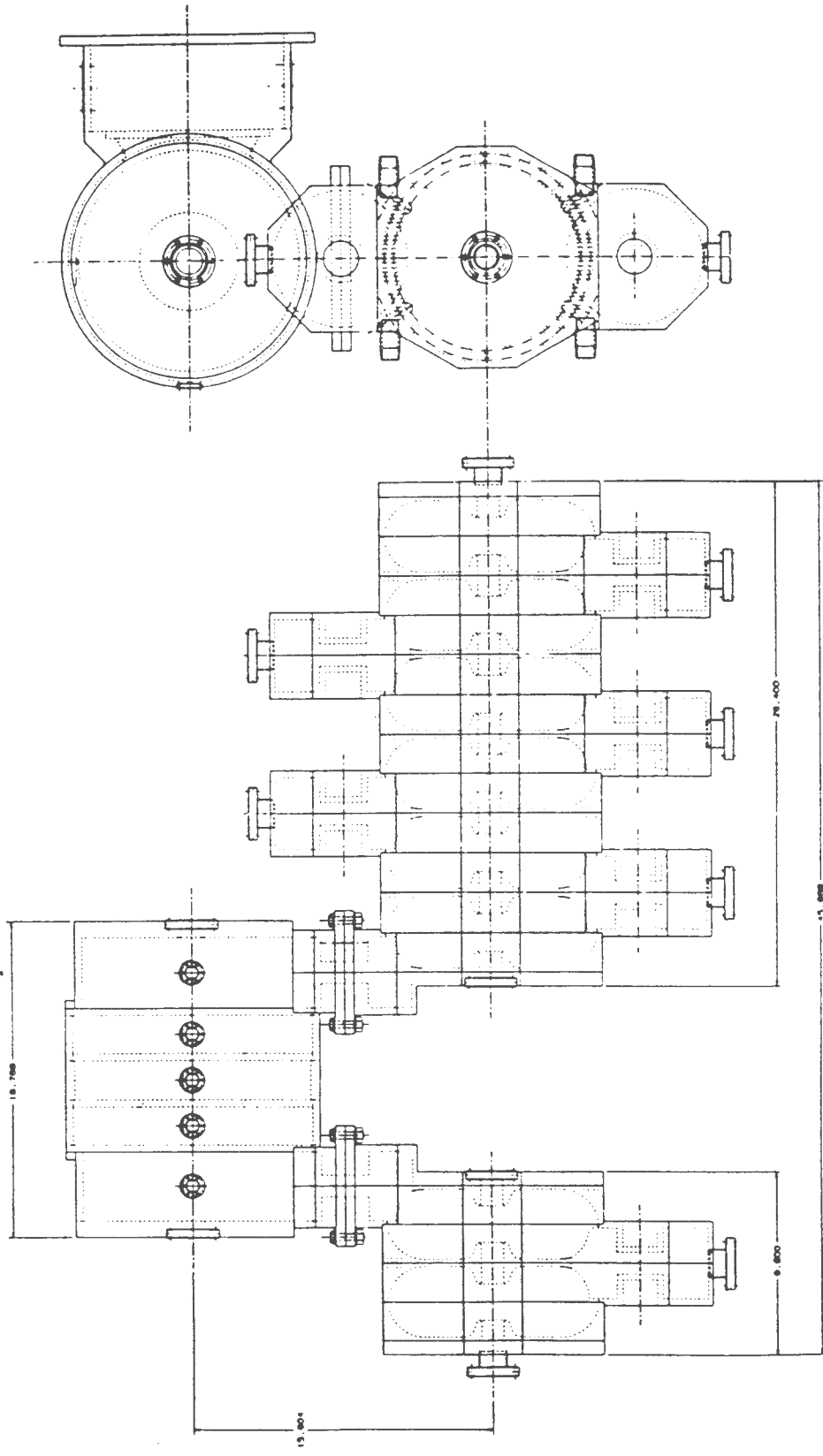


Figure 5 - Side-Coupled Structure Power Test Model

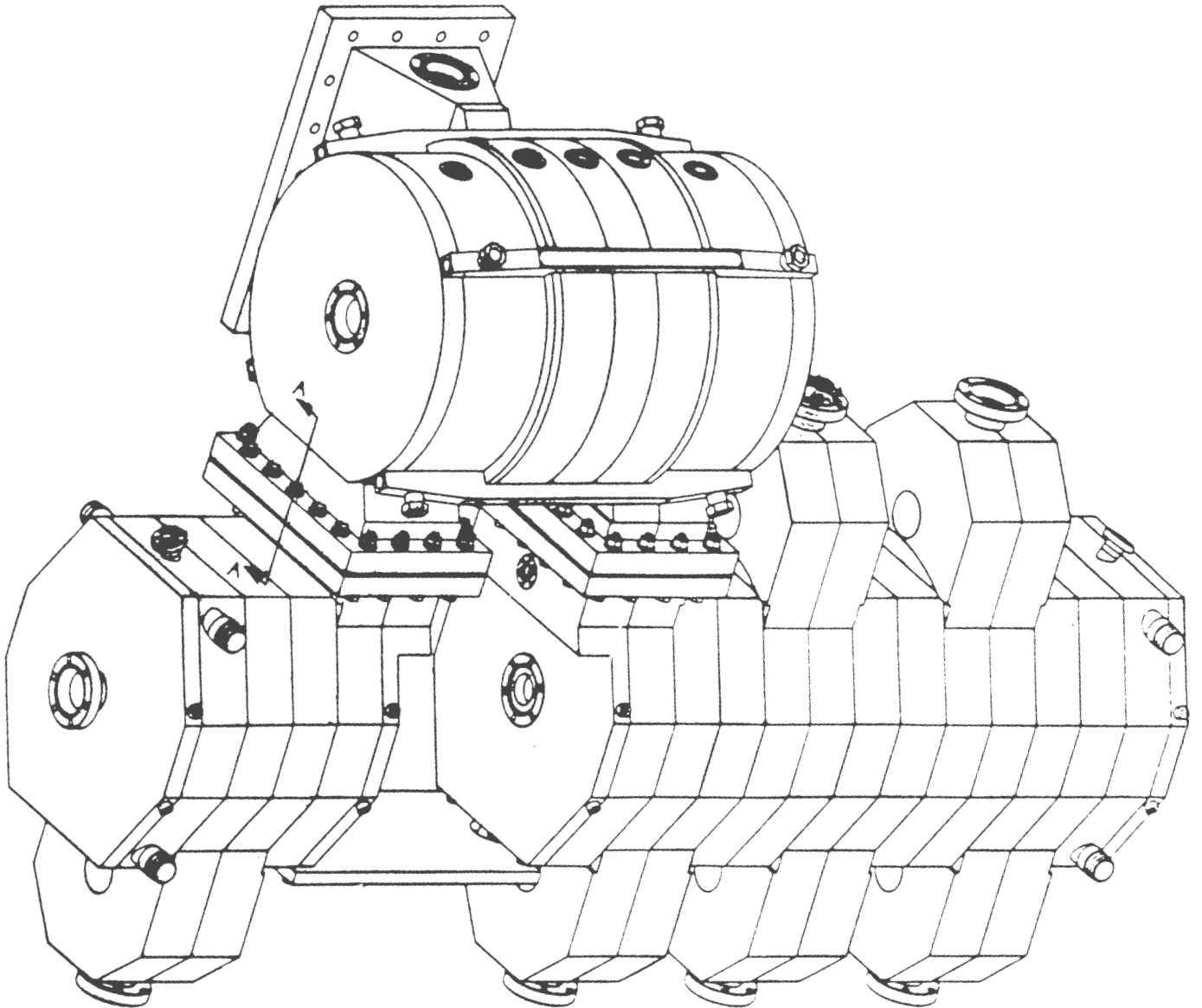


Figure 6 - Isometric view of side-coupled power test model

Figure 7

SCS Reference Design Cavity

(dimensions in mm)

Half cell

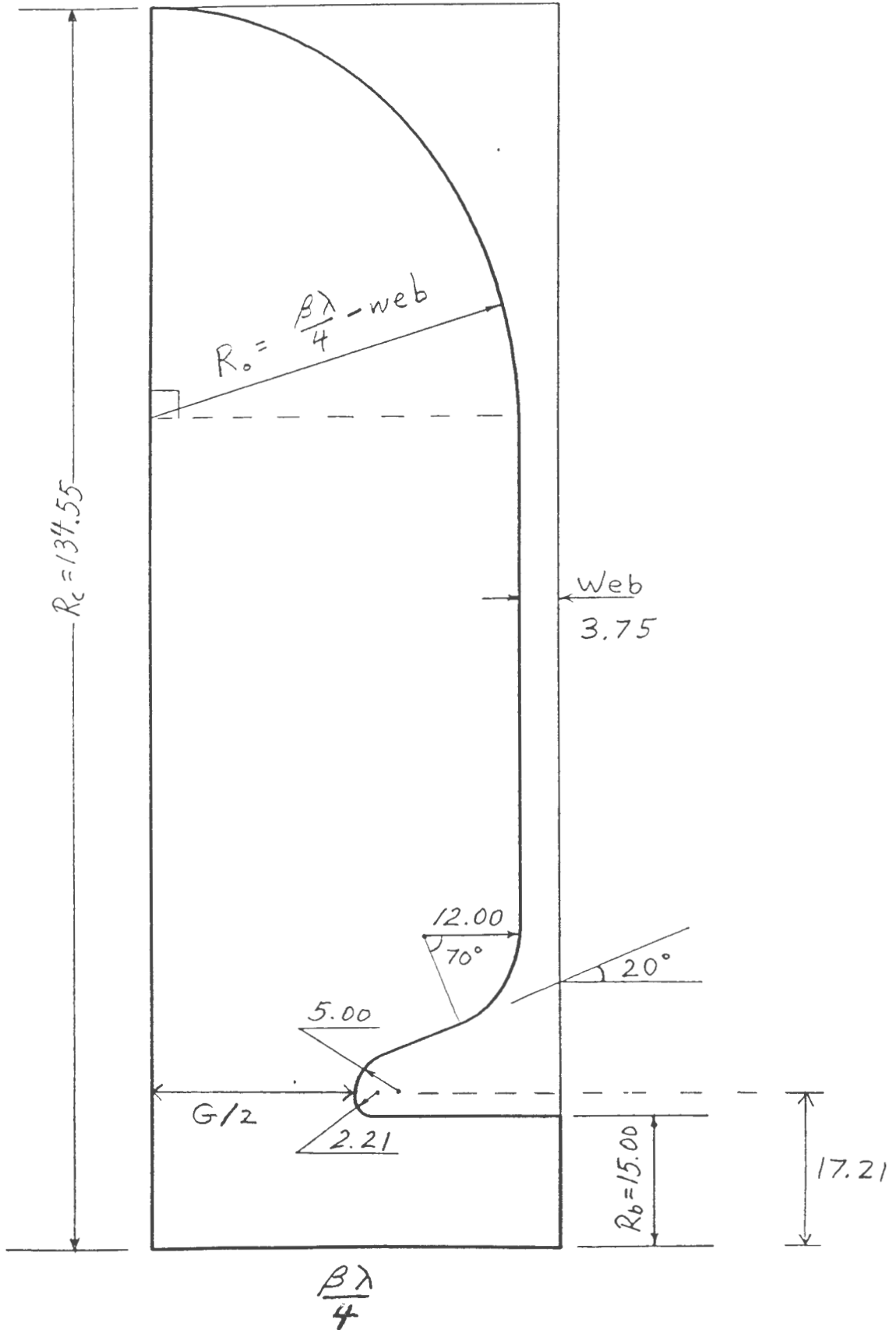


Figure 8

ZT² vs. Beta

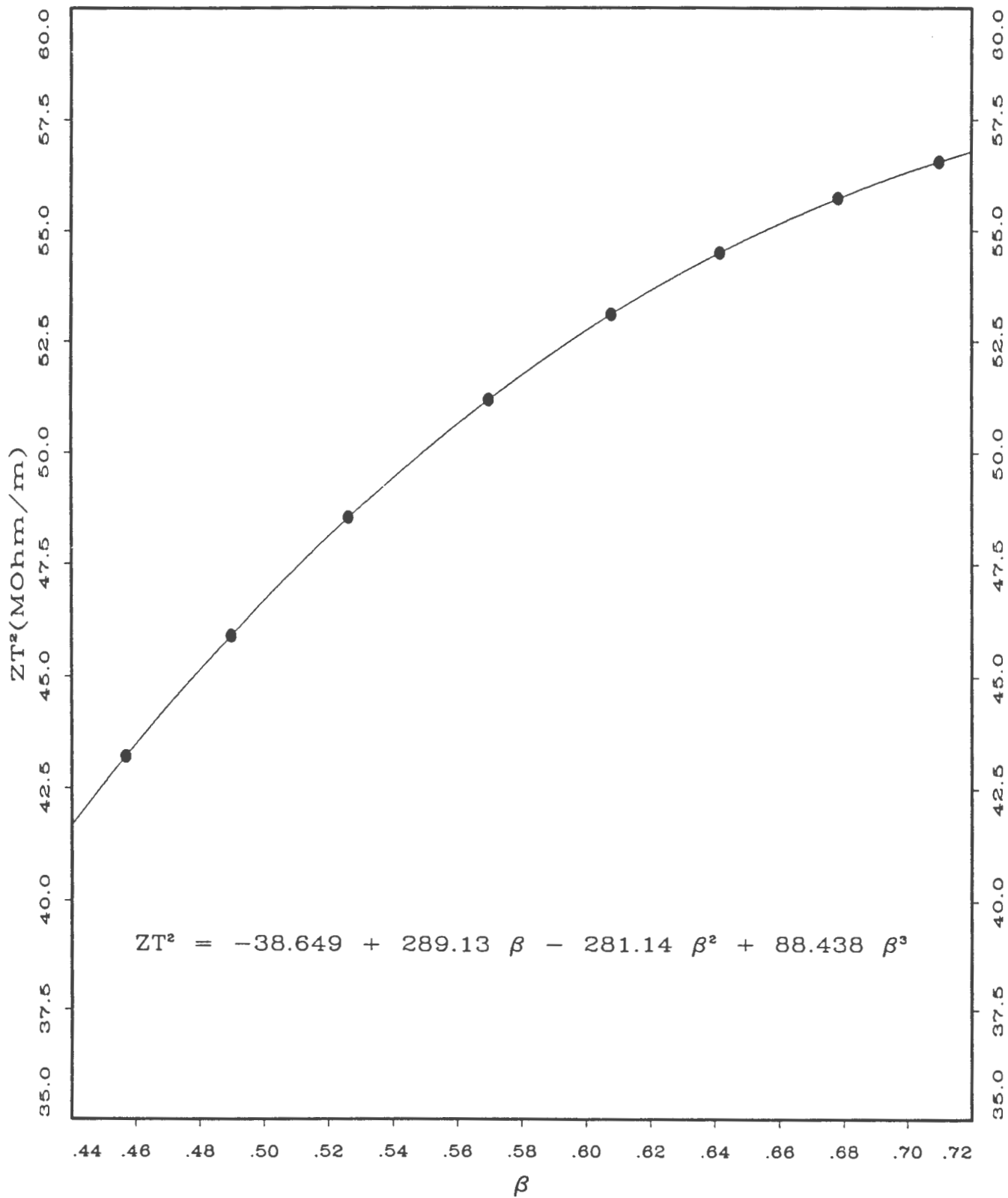


Figure 9

Transit Time Factor vs. Beta

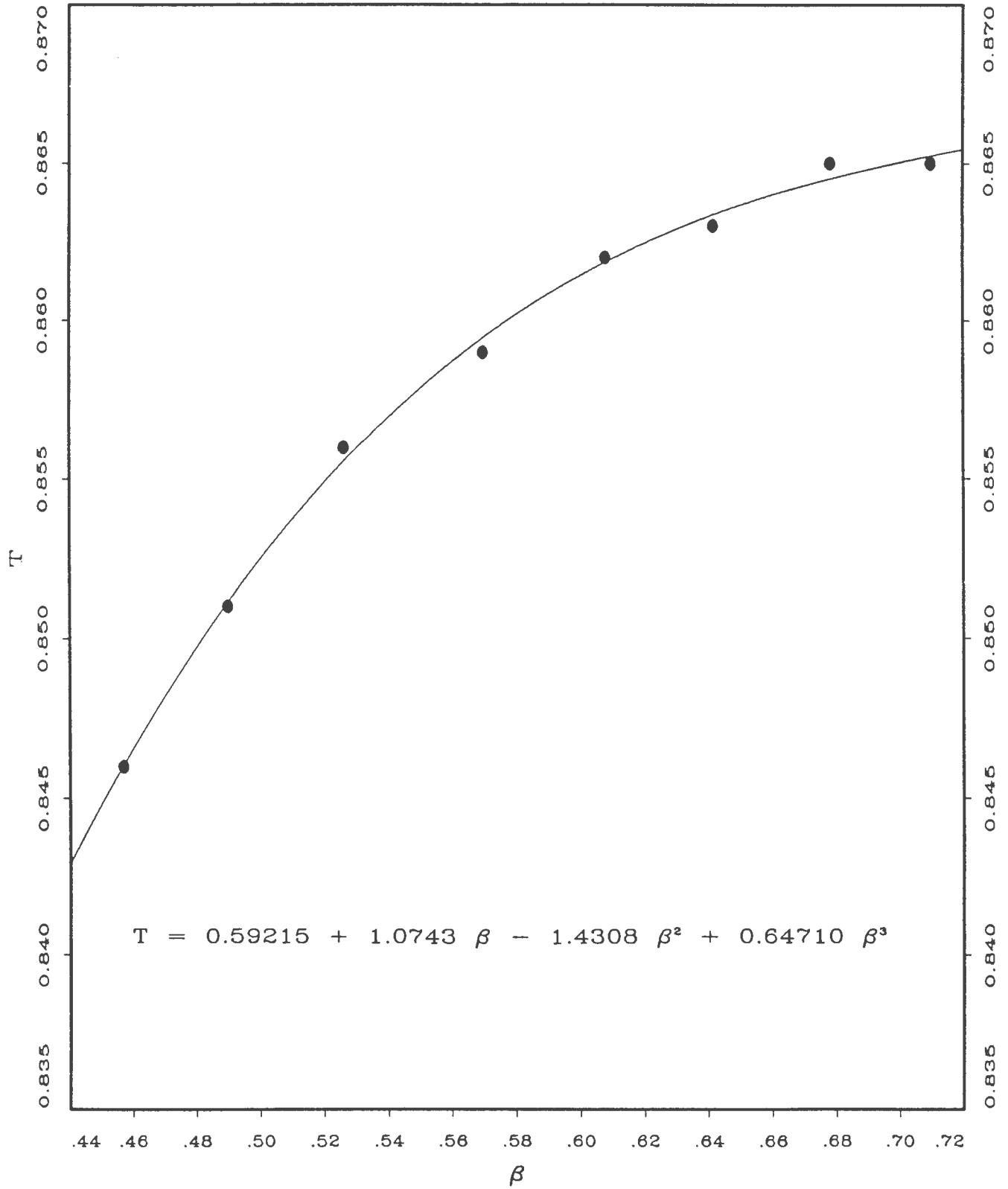


Figure 10

E_{\max}/E_0 vs. Beta

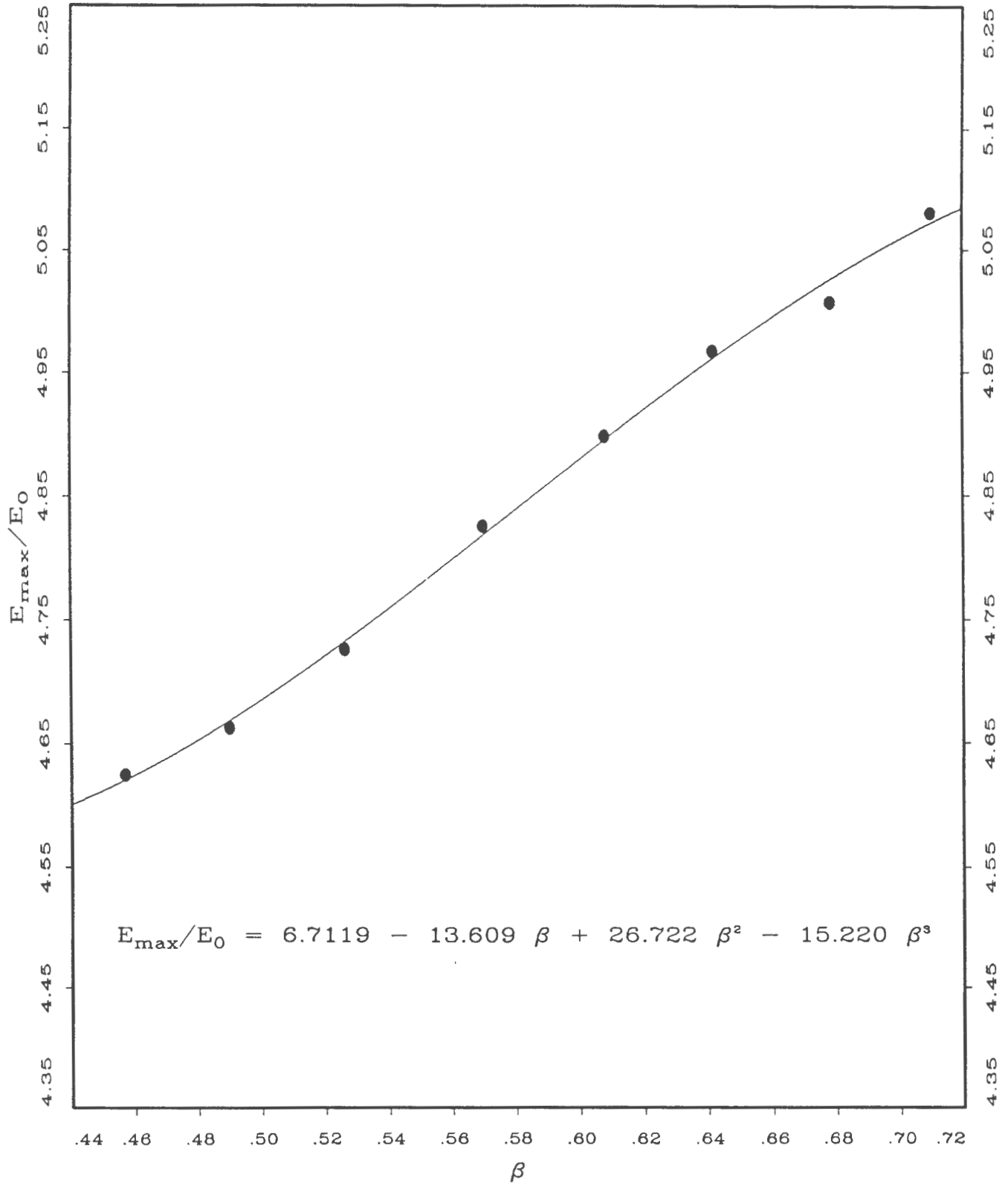
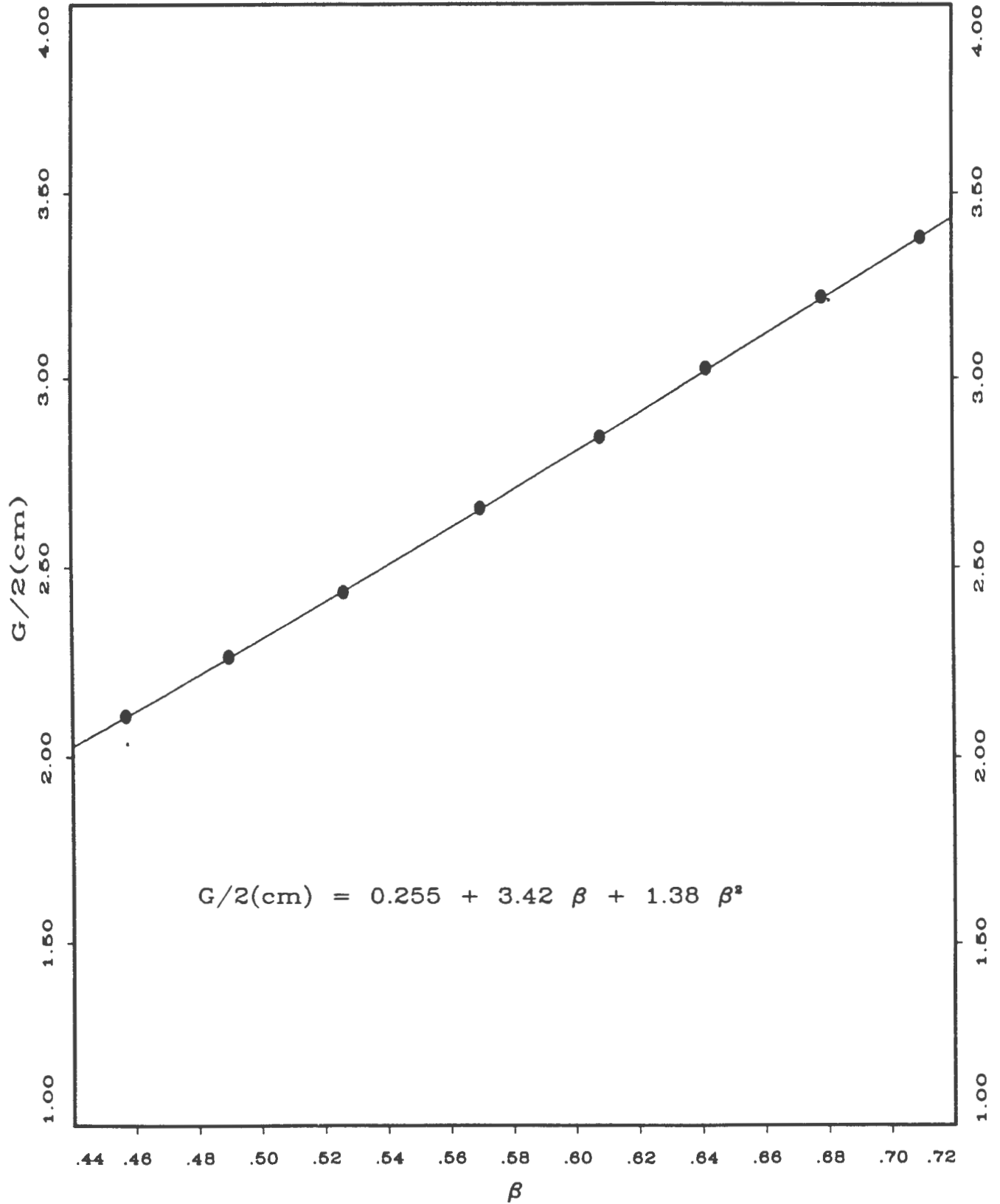


Figure 11

Half Gap Length vs. Beta



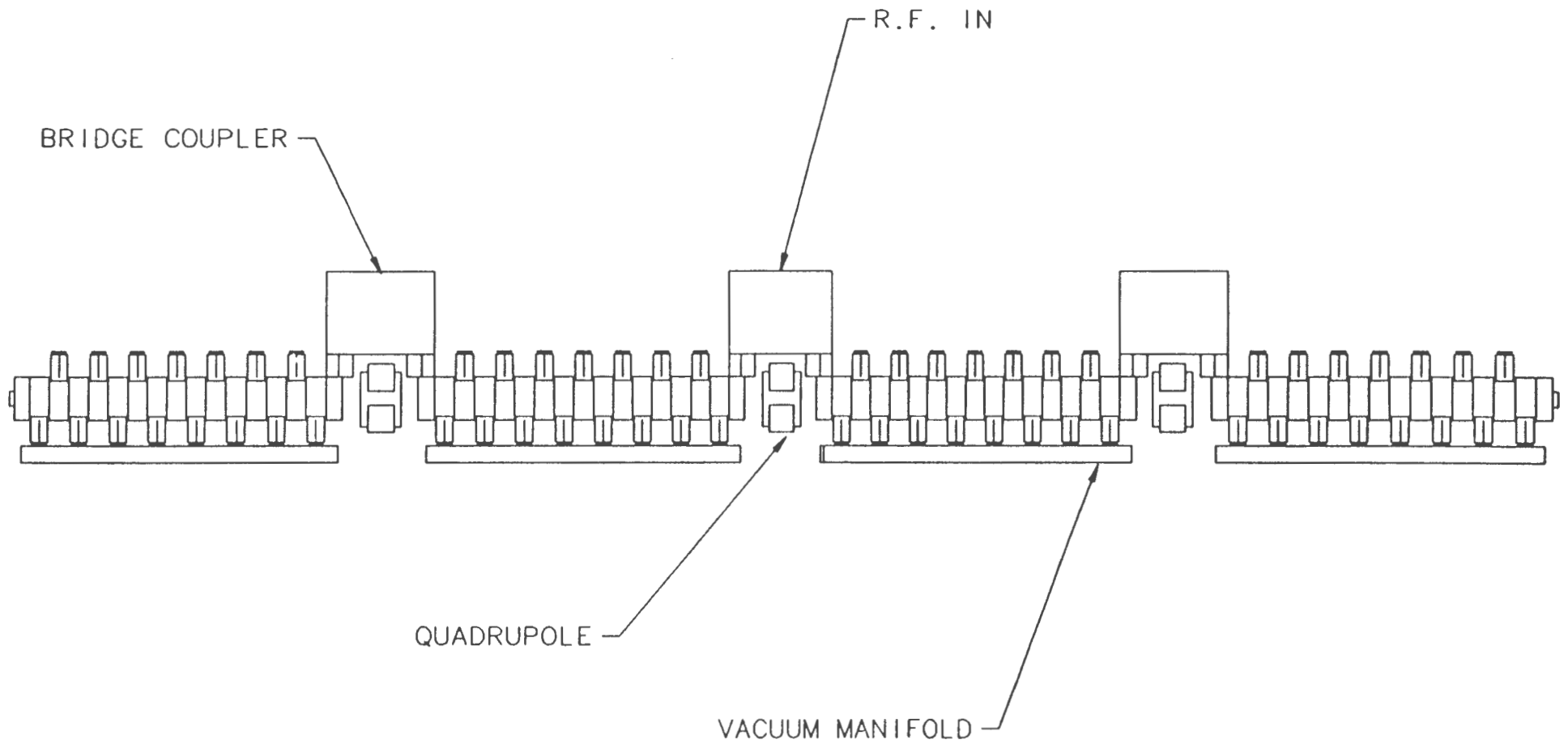


Figure 12 - Schematic of one 805 MHz side-coupled cavity module. The module consists of four sections connected by bridge couplers. Each section contains sixteen accelerating cells.

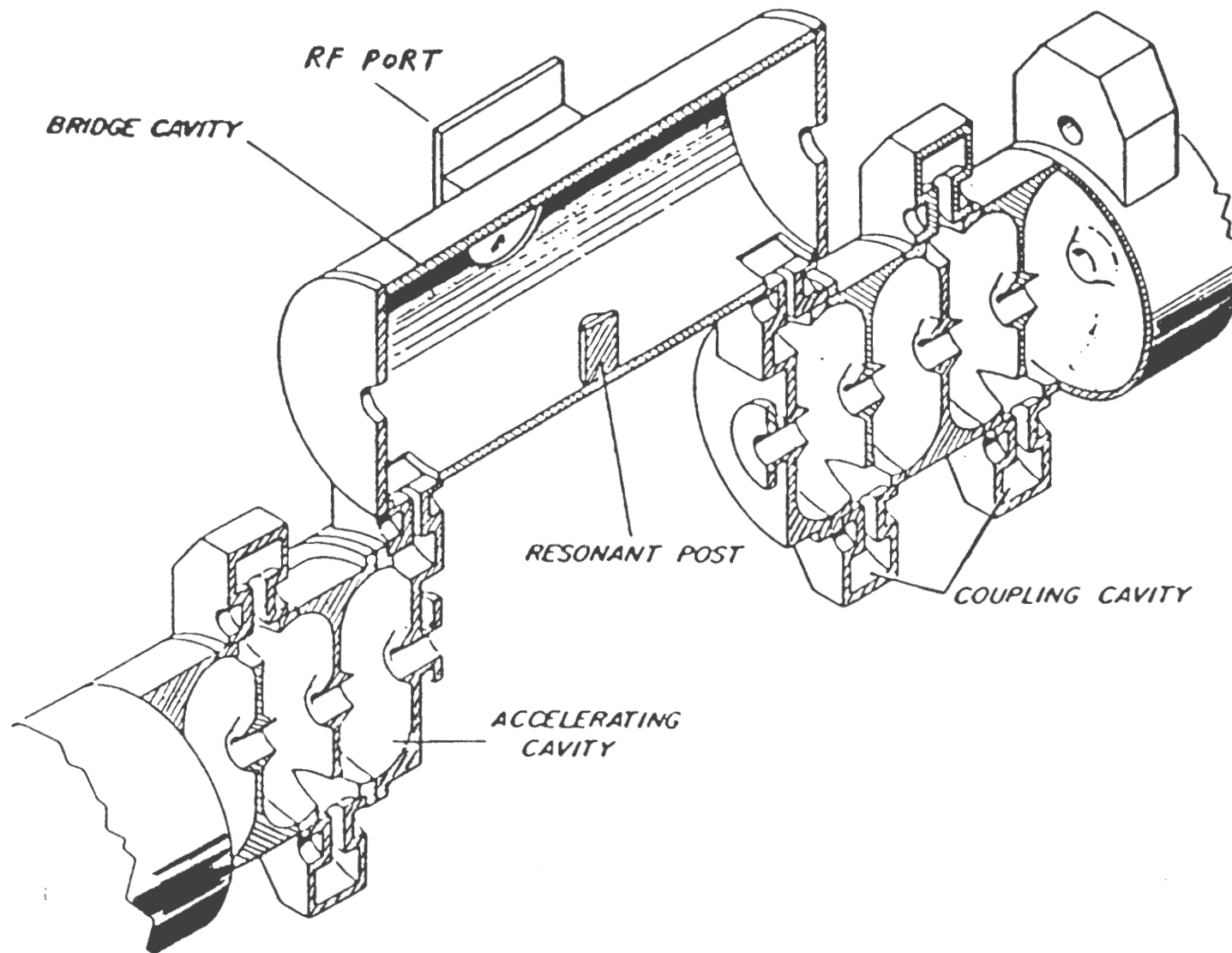


Figure 14 - LAMPF post-stablized bridge coupler connecting accelerating sections

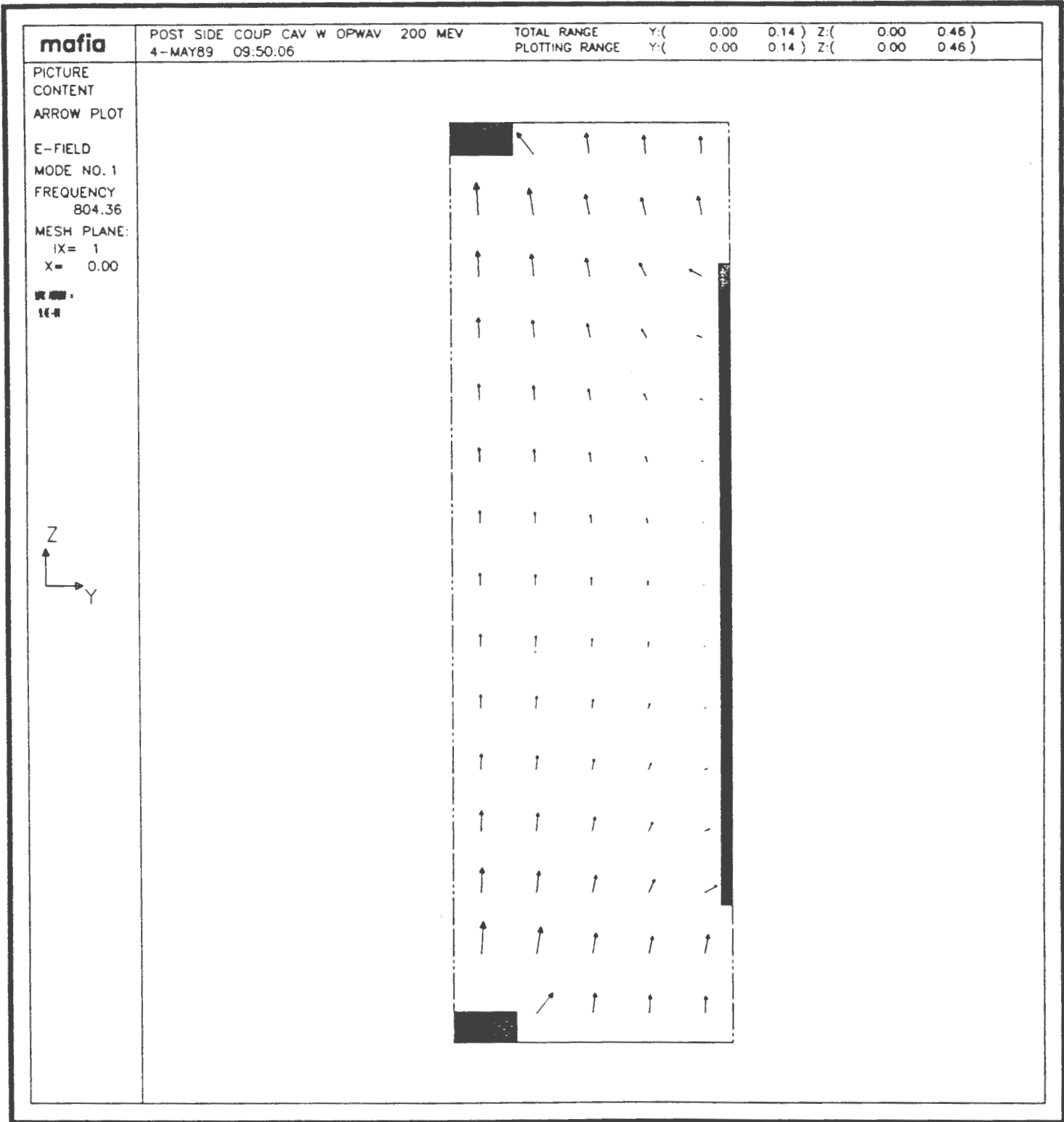


Figure 15 - Post-stablized bridge coupler designed with MAFIA

EM ; Poisson cycle number 3000

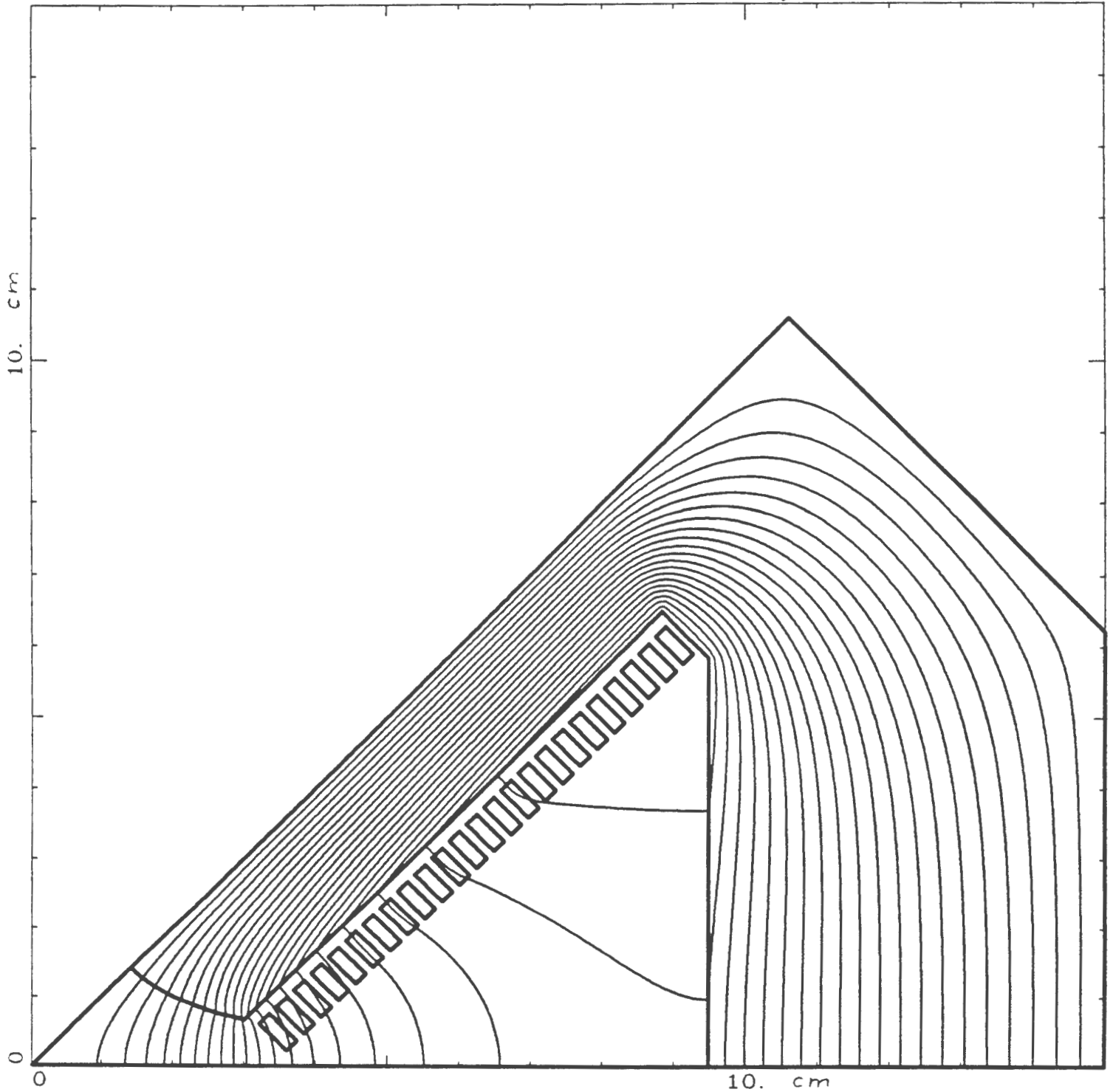


Figure 16 - Output of the program POISSON showing an octant of a 7 cm core length quad with 2 cm pole tip radius.

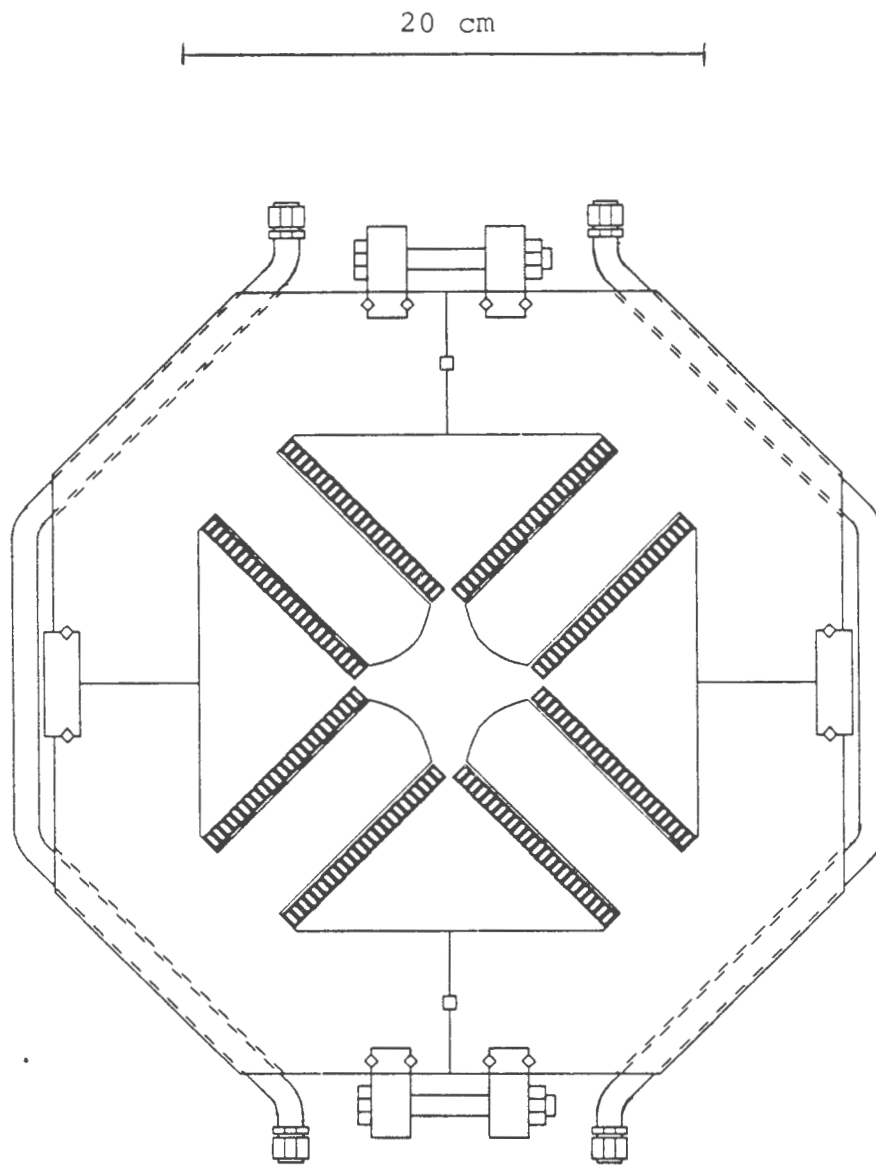
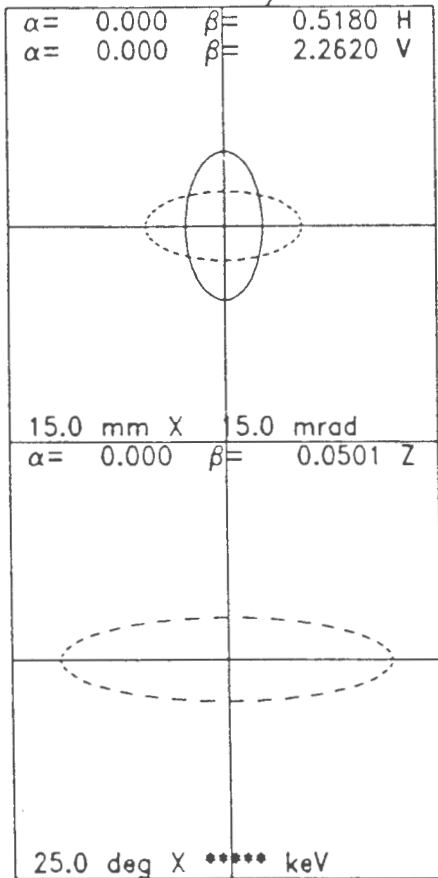


Figure 17 - Quadrupole cross section

Buncher/Matching Section - 2 RF & 2 Quad 11-MAR-89 19:04:00



Beam Current= 200.0
 EMITI= 13.80 13.10 7450.00
 EMITO= 13.66 12.97 7449.98
 W= 114.510 116.517

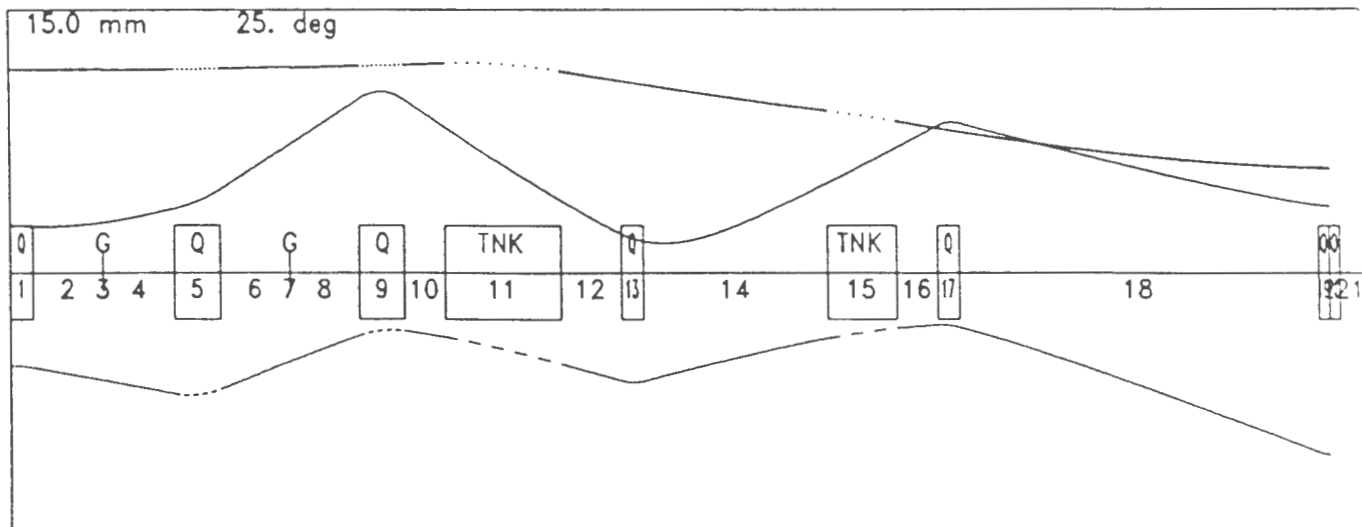
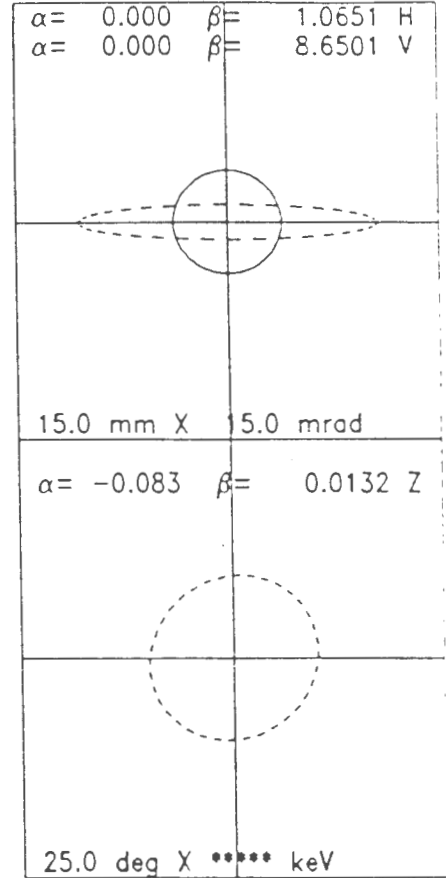


Figure 18 - Initial beam ellipses, final beam ellipses and beam envelopes for the 116-MeV transition section. The bunch width and horizontal plane envelope are shown above the layout schematic; the vertical plane envelope is shown below the layout.

FIGURE 19. BUNCH SIZE REDUCTION AND SHAPE OSCILLATION

SCS -805MHZ LINAC BEAM ENVELOPE

PART.DISTN.-WATERBAG

BEAM CURRENT-50 MA.-

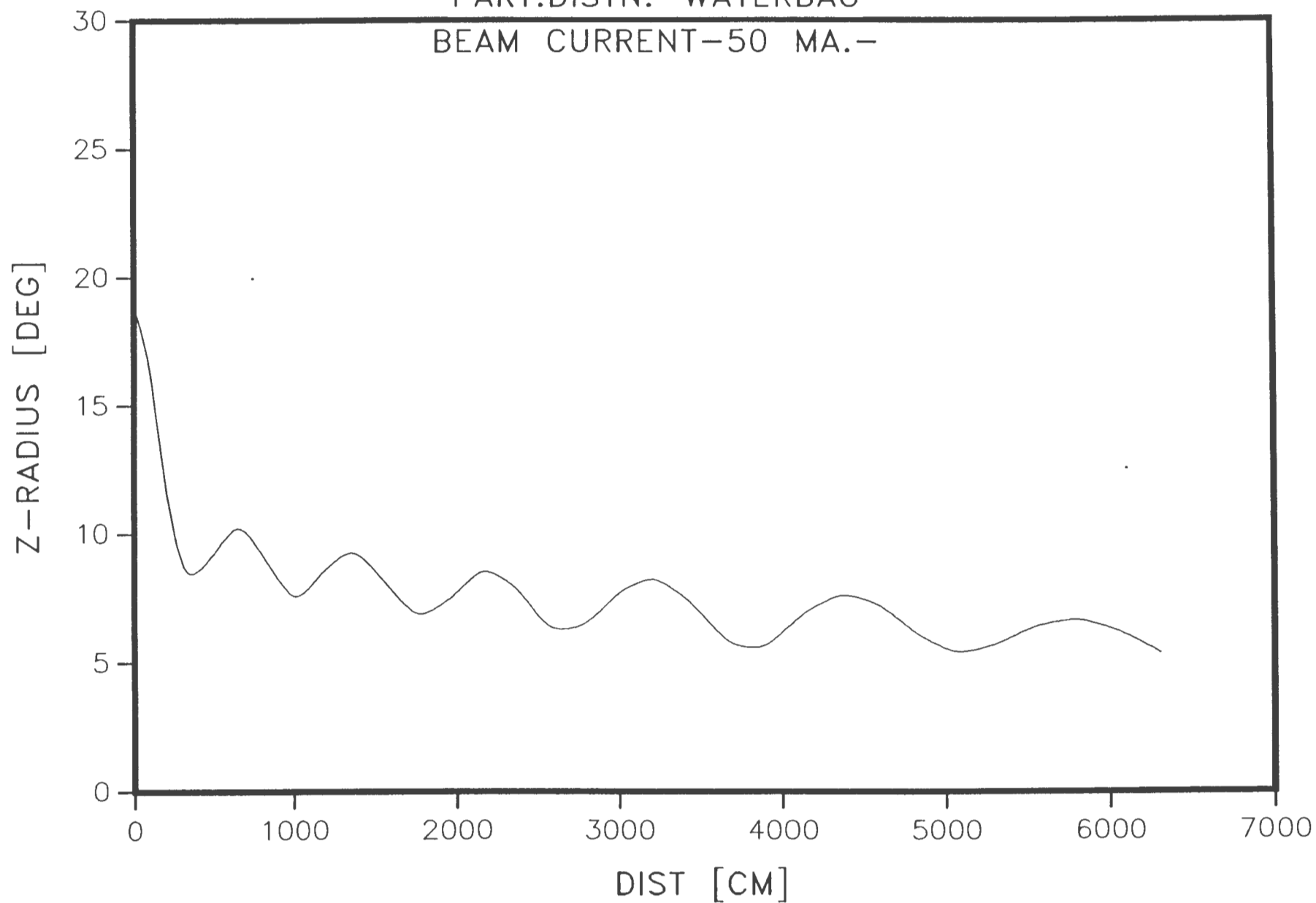


FIGURE 20. Z-PLANE 90% EMITTANCE GROWTH (116-400 MEV)

SCS -805MHZ LINAC BEAM EMITTANCE

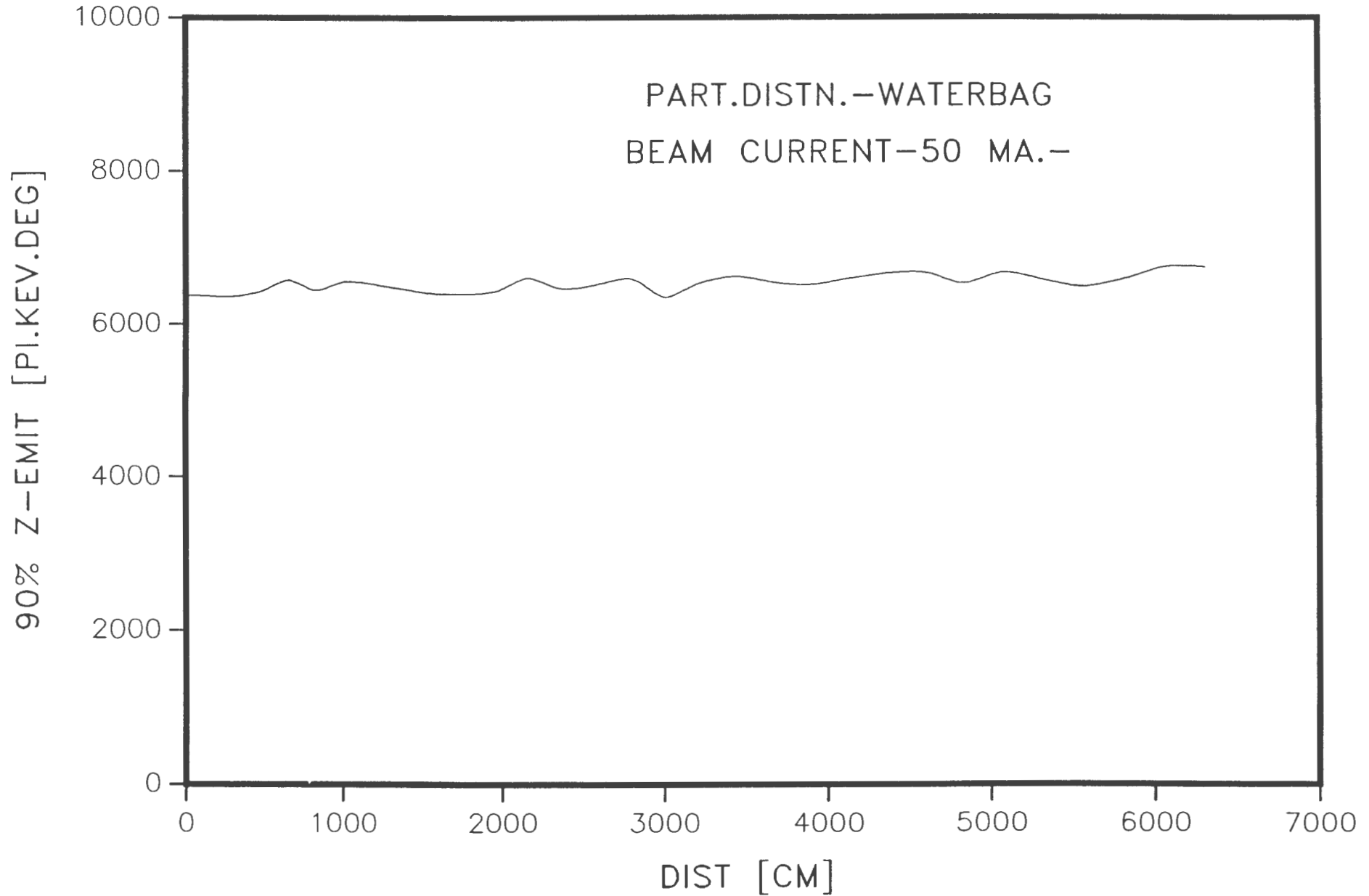


FIGURE 21. BEAM RADIUS IN FODO CHANNEL.116-400 MEV

SCS -805MHZ LINAC BEAM ENVELOPE

PART.DISTN.-WATERBAG

BEAM CURRENT-50 MA.-

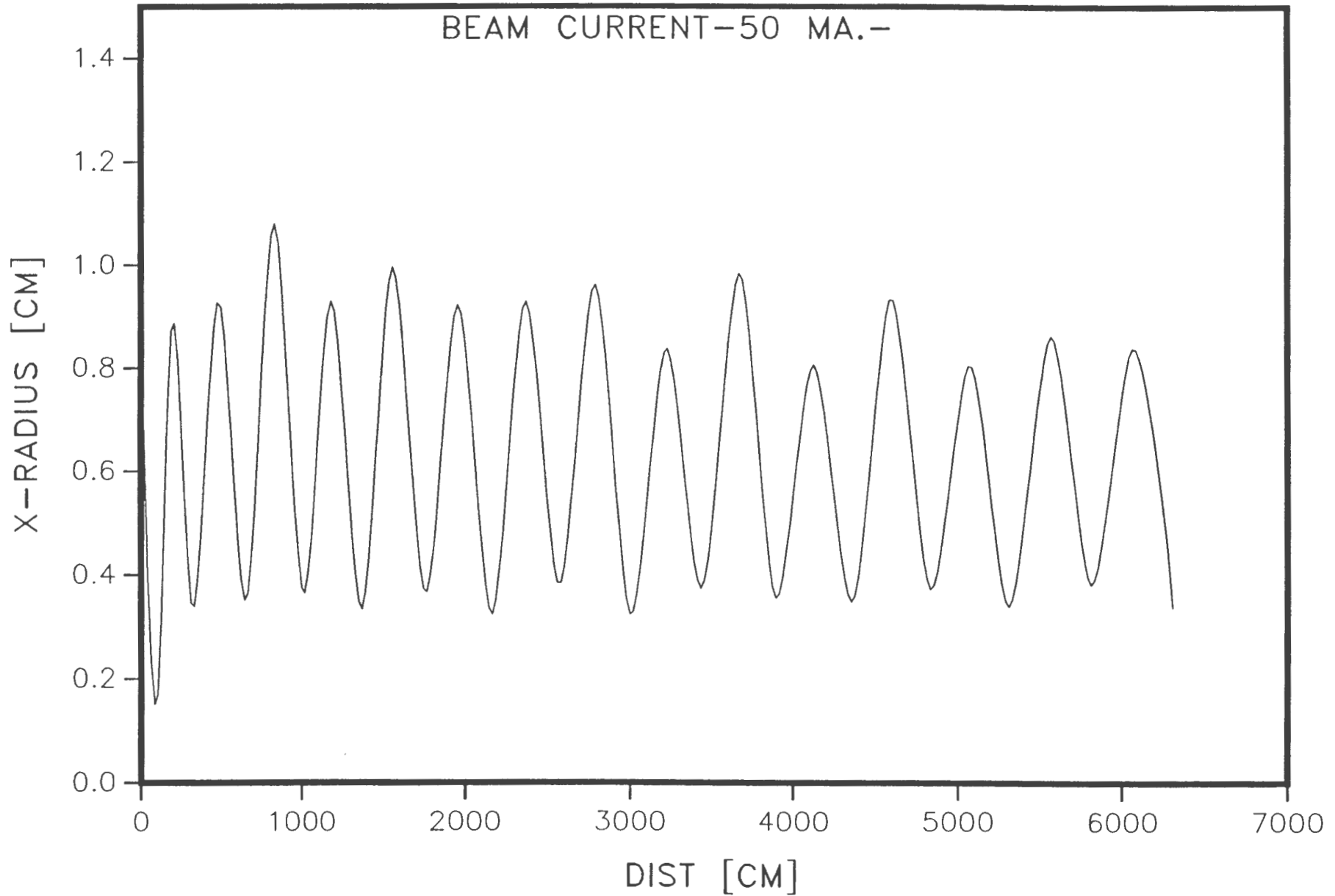


FIGURE 22. X-PLANE 90% EMITTANCE (norm.) (116-400 MEV)

SCS -805MHZ LINAC BEAM EMITTANCE

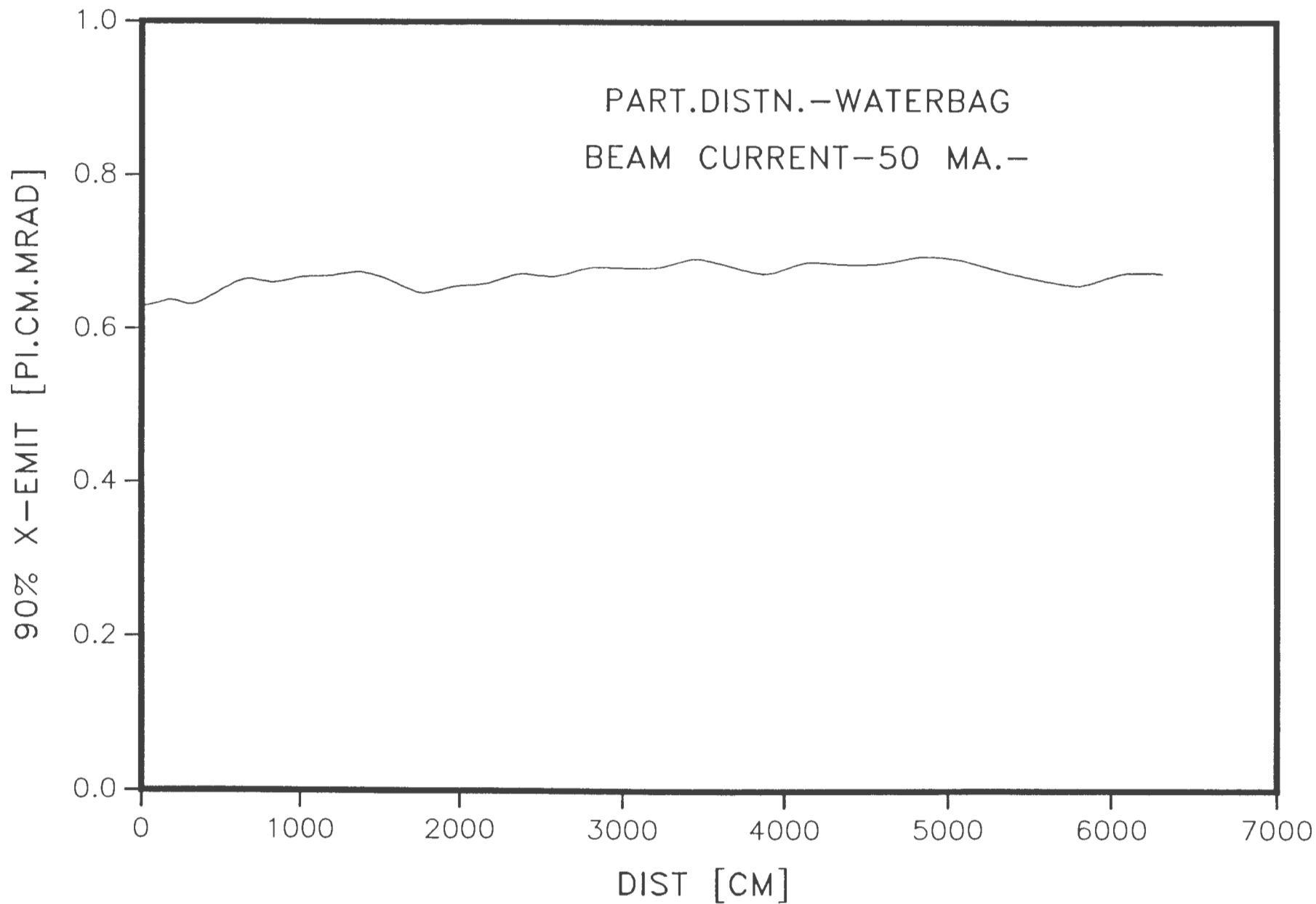
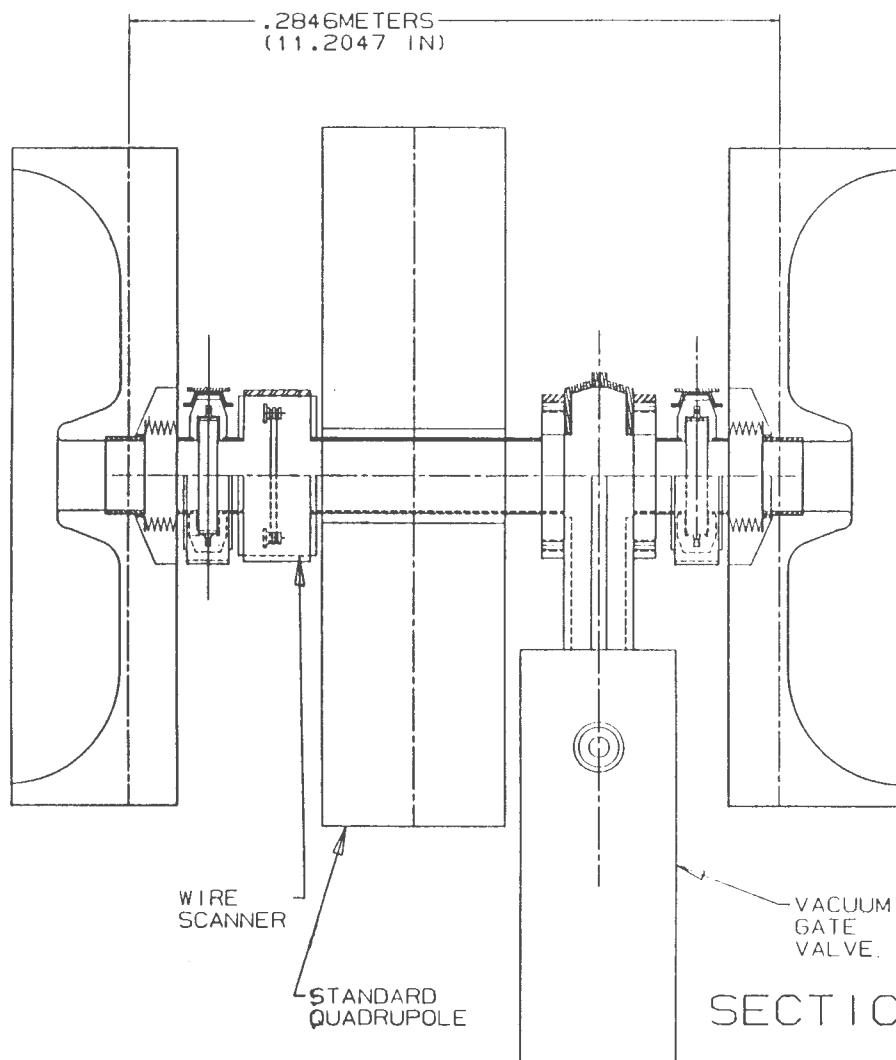


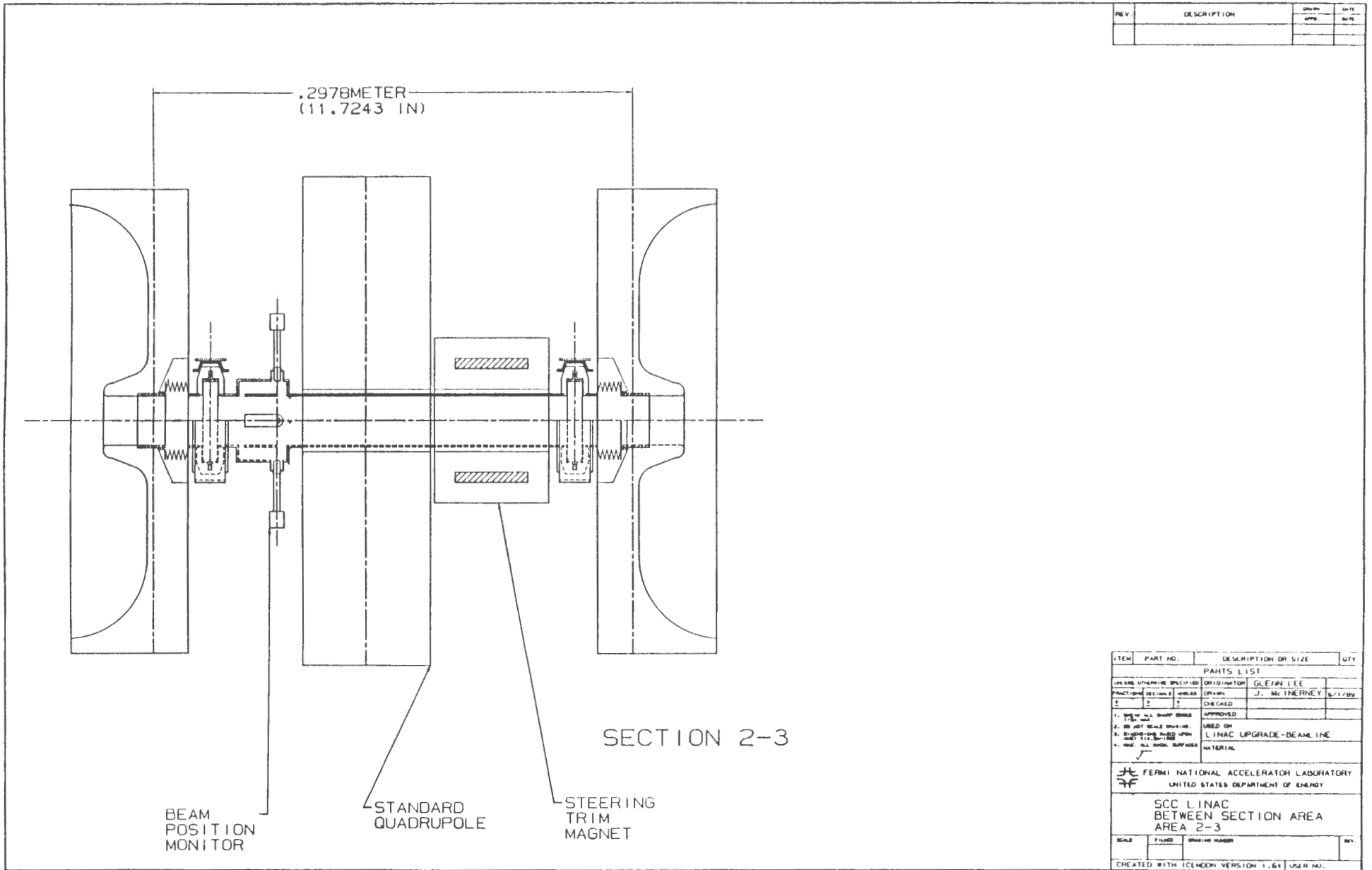
Figure 24



REV.	DESCRIPTION	DATE	BY
		APPRO.	DATE

ITEM	PART NO.	DESCRIPTION OR SIZE	QTY.
PARTS LIST			
UNLESS OTHERWISE SPECIFIED	ORIGINATOR	GLENN LEE	
FRAC./DEC./IN.	DRAWN	J. MCINERNEY	6/1/88
	CHECKED		
1. DIM. ALL SHARP EDGES TO SHARP	APPROVED		
2. DO NOT SCALE DRAWING	USED ON		
3. DIMENSIONS BASED UPON DRAWING TO DIM LINE	LINAC UPGRADE-BEAMLINE		
4. HIDE ALL HIDDEN SURFACES	MATERIAL		
FERMI NATIONAL ACCELERATOR LABORATORY UNITED STATES DEPARTMENT OF ENERGY			
SCC LINAC BETWEEN SECTION AREA AREA 2-1			
SCALE	FILMED	QUANTITY NUMBER	REV.

Figure 26



REV.	DESCRIPTION	DATE	BY

ITEM	PART NO.	DESCRIPTION OR SIZE	QTY
PARTS LIST			
USE AND OTHERWISE SPECIFIED	ORIGINATOR	GLENN LEE	
FUNCTIONAL SECTION	ANALYST	OPRATOR	J. MCINERNEY 6/1/80
1	2	3	CHECKED
1. DIM. ALL SHARP EDGES TO BE MAINT.		APPROVED	
2. DO NOT SCALE DIMENSIONS		USED ON	LINAC UPGRADE-BEAM LINE
3. DIMENSIONS ARE TO CENTER UNLESS NOTED OTHERWISE		MATERIAL	
4. DIM. ALL SURFACES			
FERMILAB NATIONAL ACCELERATOR LABORATORY UNITED STATES DEPARTMENT OF ENERGY			
SCC LINAC BETWEEN SECTION AREA AREA 2-3			
SCALE	FILED	WORKING NUMBER	REV.
CREATED WITH ICEHORN VERSION 1.64 USER NO.			

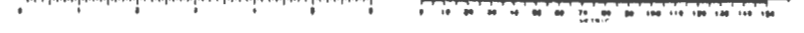
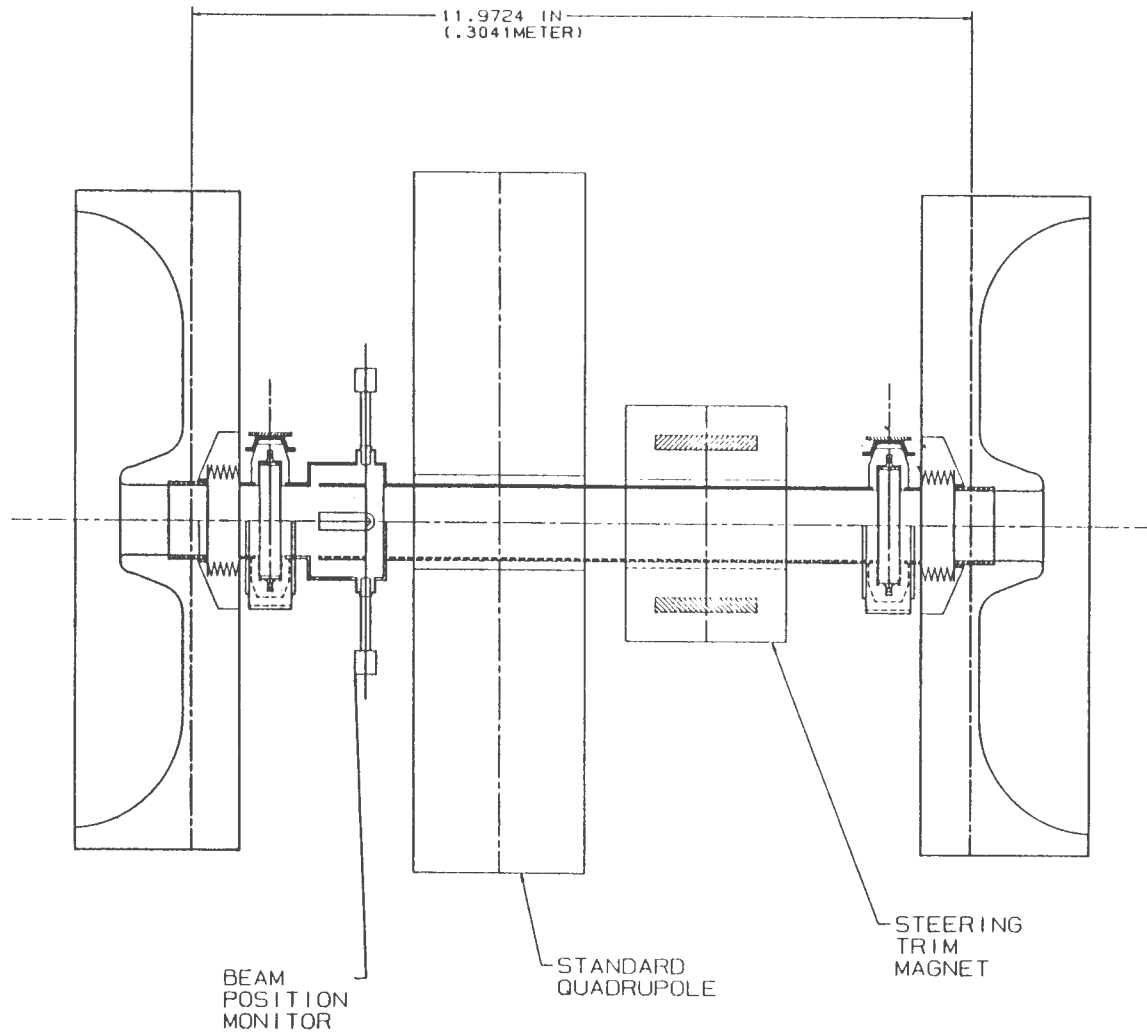


Figure 27



SECTION 2-4

REV.	DESCRIPTION	DATE	BY

ITEM	PART NO.	DESCRIPTION OR SIZE	QTY.
PARTS LIST			
UNLESS OTHERWISE SPECIFIED:		ORIGINATOR	GLENN LEE
FRACTION	DECIMALS	UNITS	DRAWN
1	2	3	J. McJERNEY
4	5	6	CHECKED
1. FINISH ALL SHARP EDGES		APPROVED	
2. DO NOT SCALE DRAWING		USED ON	
3. SHARPEN THE POINTS UPON		LINAC UPGRADE-BEAMLINE	
4. HOLE DIA. FROM SURFACE		MATERIAL	
 FERMI NATIONAL ACCELERATOR LABORATORY UNITED STATES DEPARTMENT OF ENERGY			
SCC LINAC BETWEEN SECTION AREA AREA 2-4			
SCALE	FILMED	DRAWING NUMBER	REV.
CREATED WITH ICEMCON VERSION 1.6A			

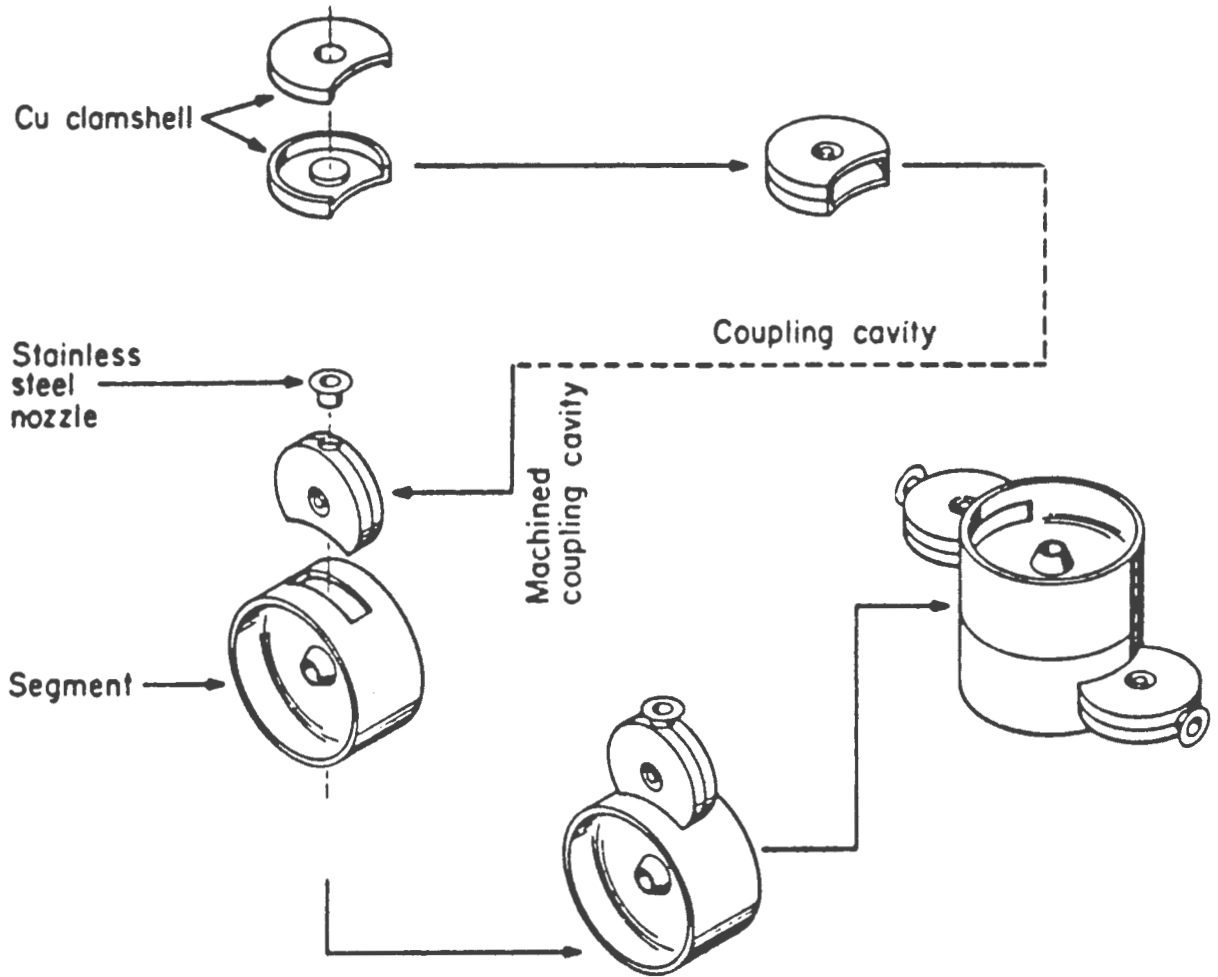


Figure 28 - Segmented construction of side-coupled accelerating structure

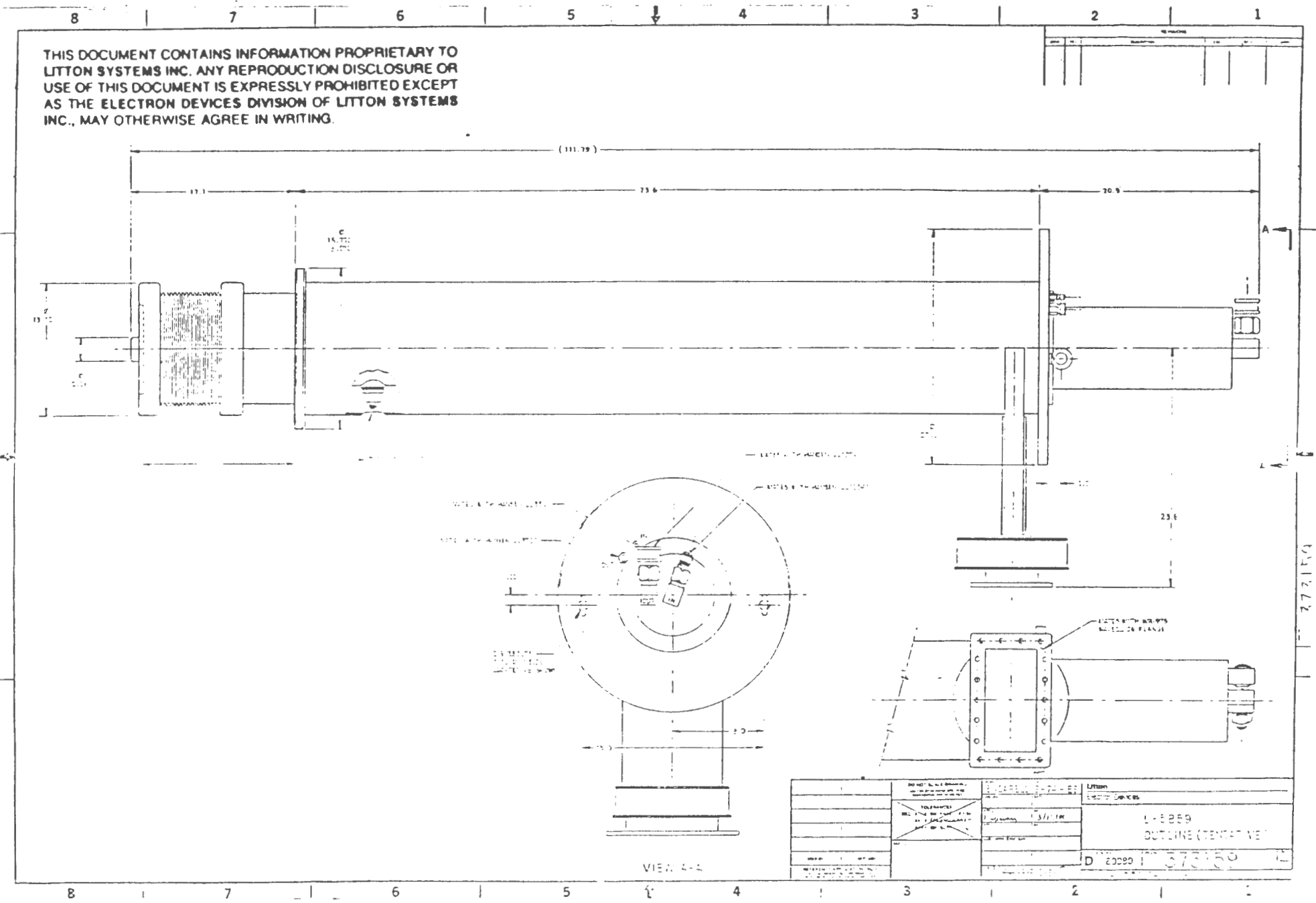


Figure 29 - Exterior view of Litton 805 MHz klystron L-5859

THIS DOCUMENT CONTAINS INFORMATION PROPRIETARY TO
LITTON SYSTEMS INC. ANY REPRODUCTION DISCLOSURE OR
USE OF THIS DOCUMENT IS EXPRESSLY PROHIBITED EXCEPT
AS THE ELECTRON DEVICES DIVISION OF LITTON SYSTEMS
INC., MAY OTHERWISE AGREE IN WRITING.

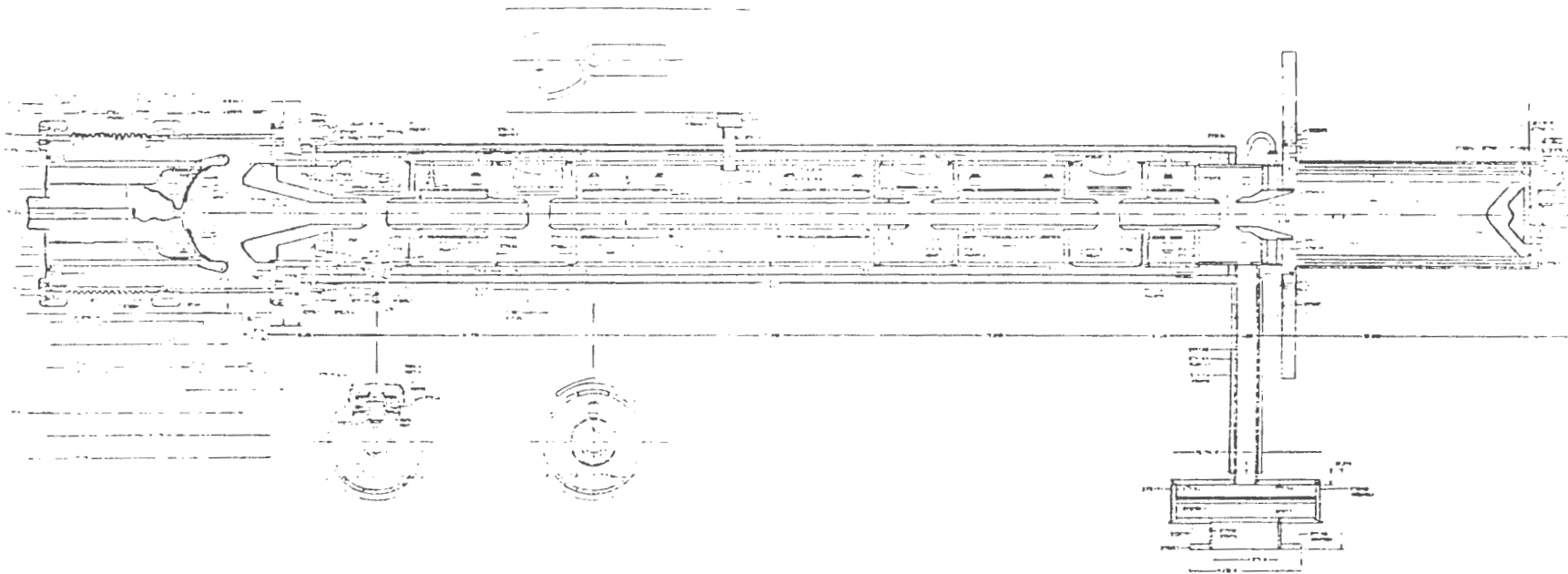


Figure 30 - Interior view of Litton 805 MHz klystron L-5859
showing details of cathode, drift-tubes, cavities, collector
and rf output port.

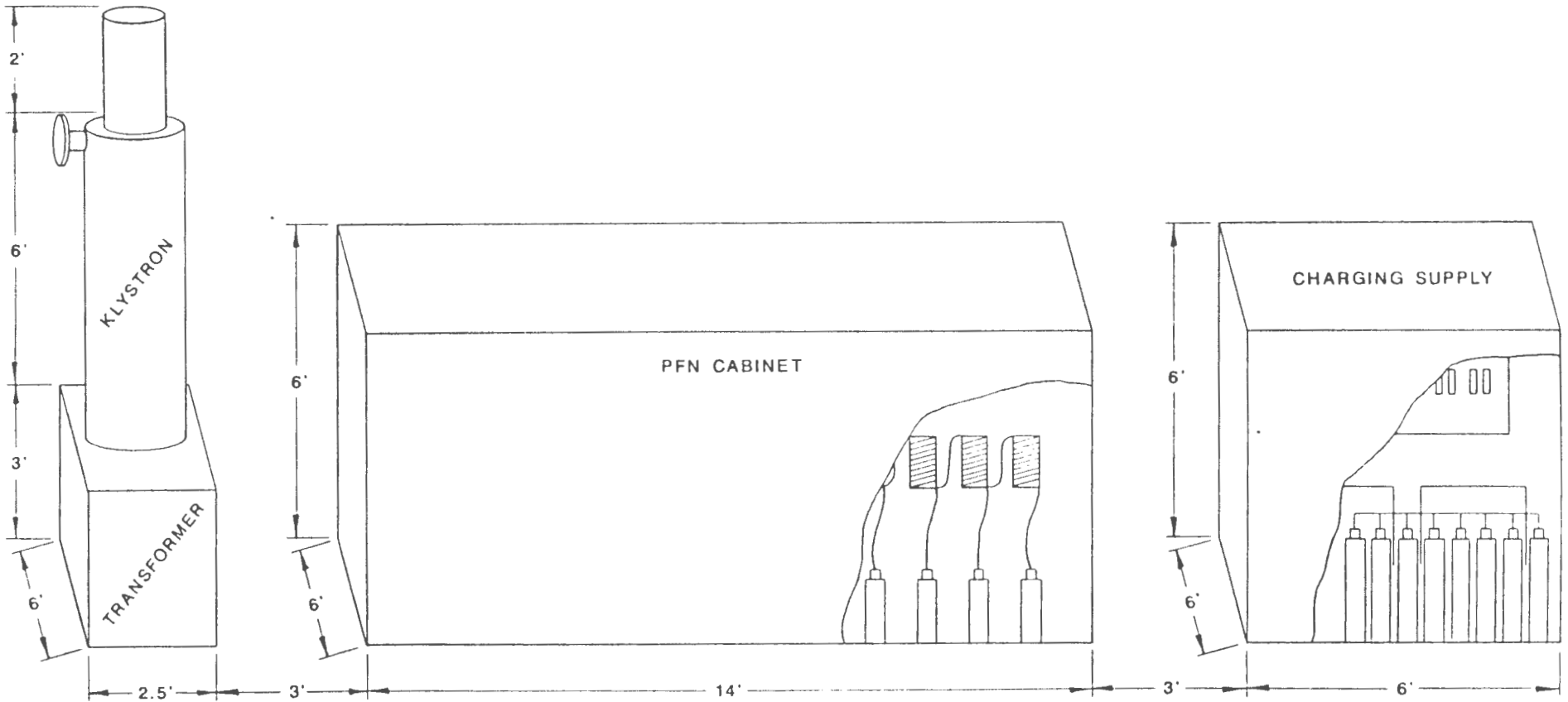


Figure 31 - Pictorial view of rf power system showing the charging supply, PFN, pulse transformer and klystron.

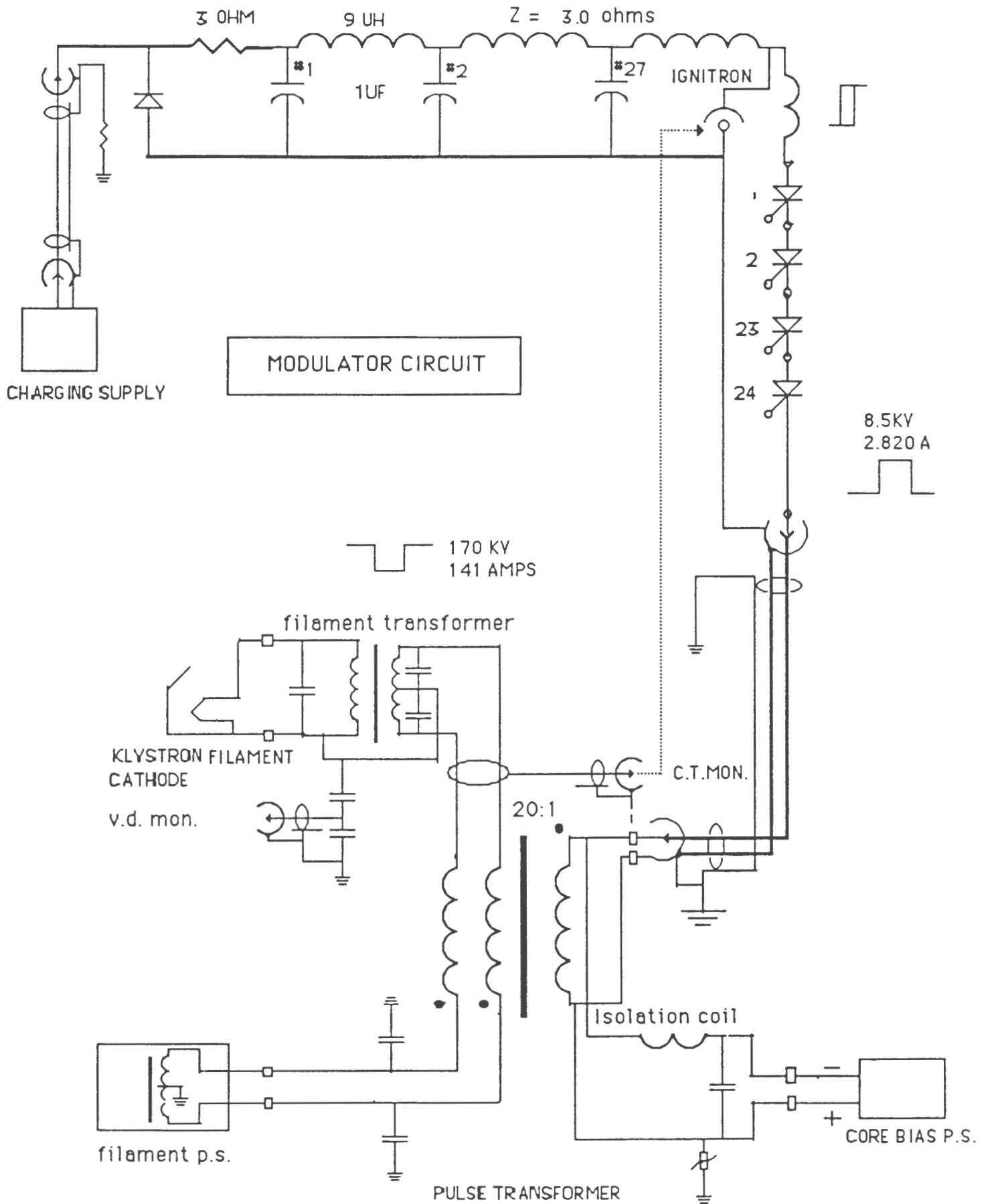


Figure 32 - RF Modulator Circuit

PFN CHARGING SUPPLY

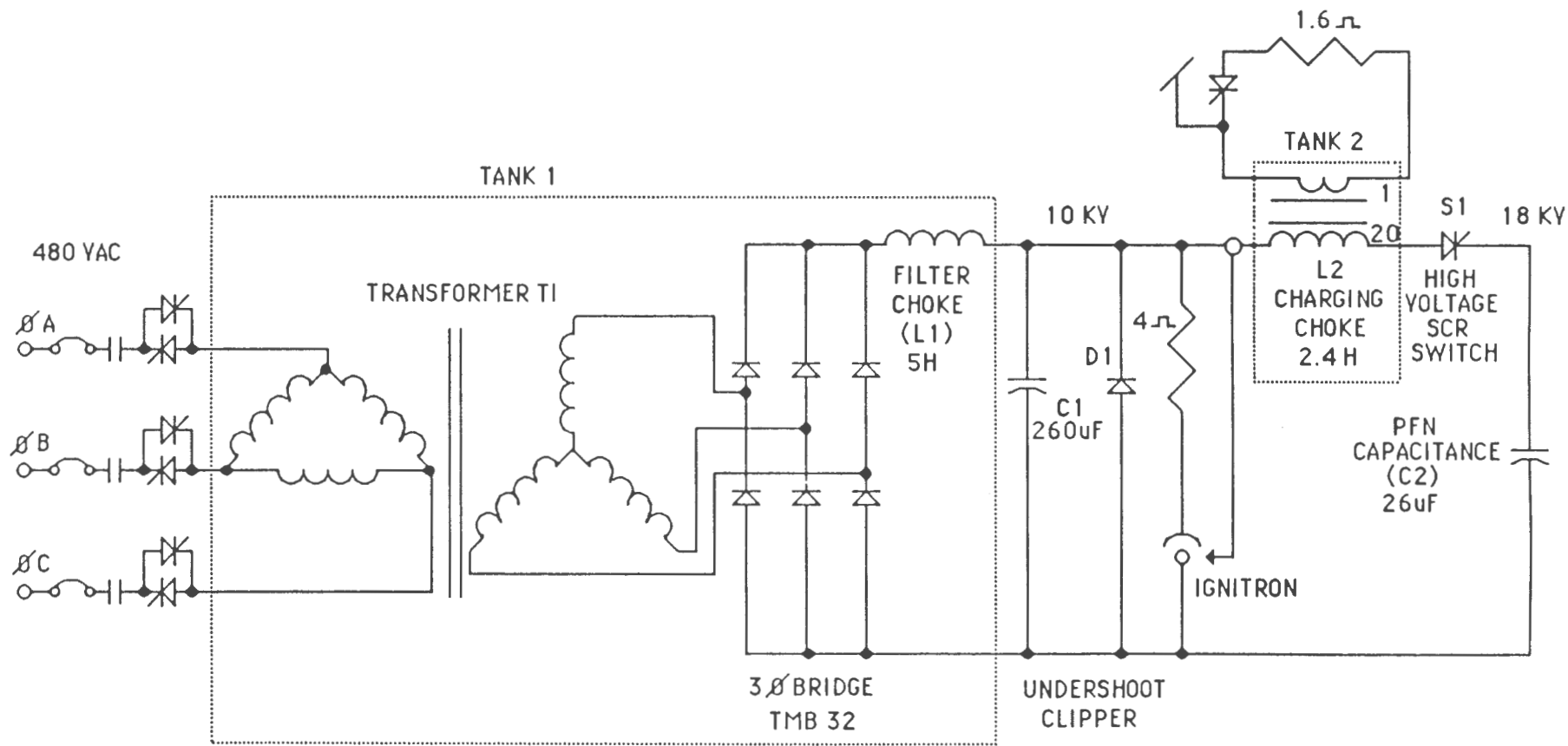


Figure 33

805 MHz SCS RF System

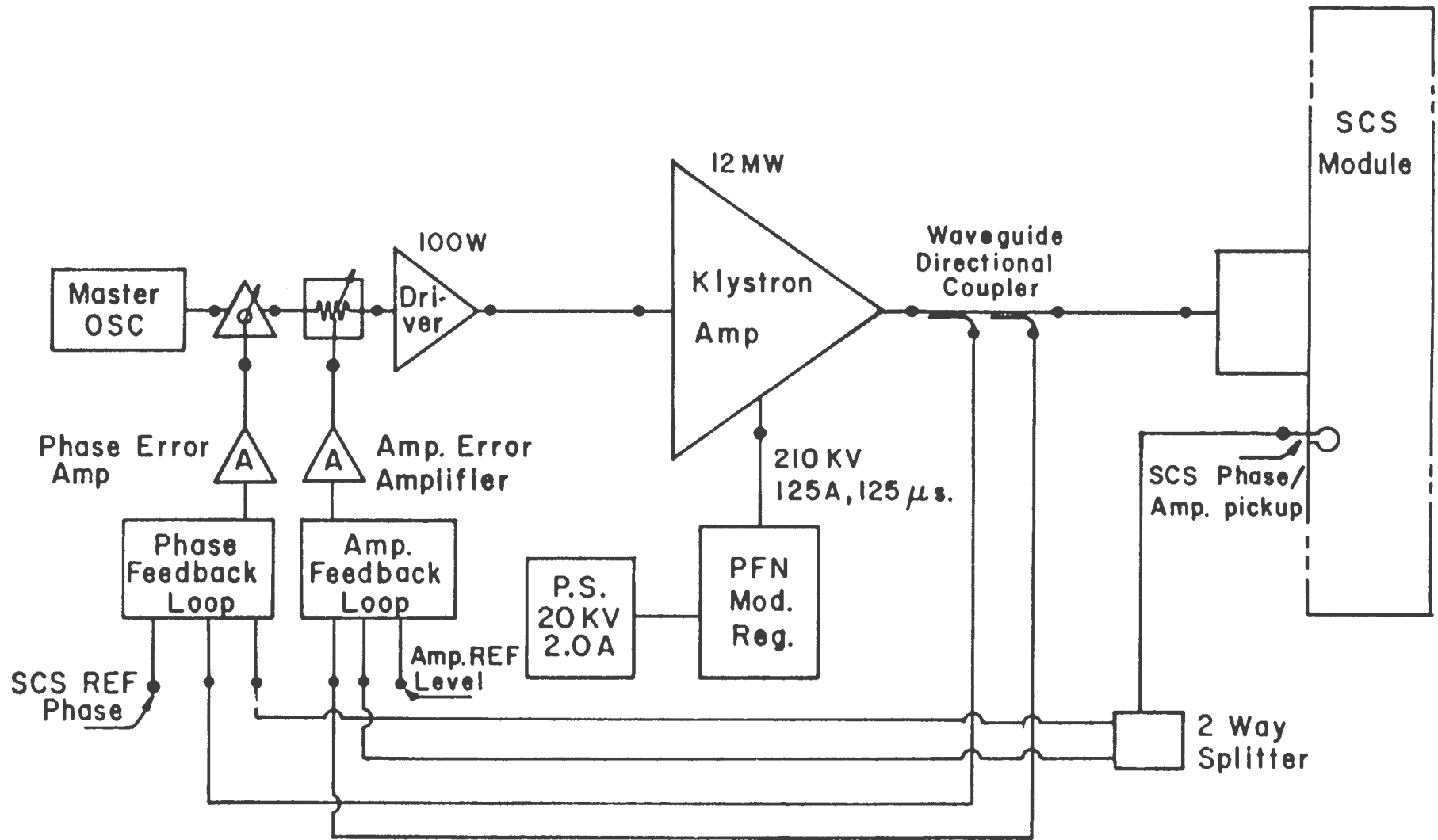


Figure 34

FEEDBACK LOOP MODEL

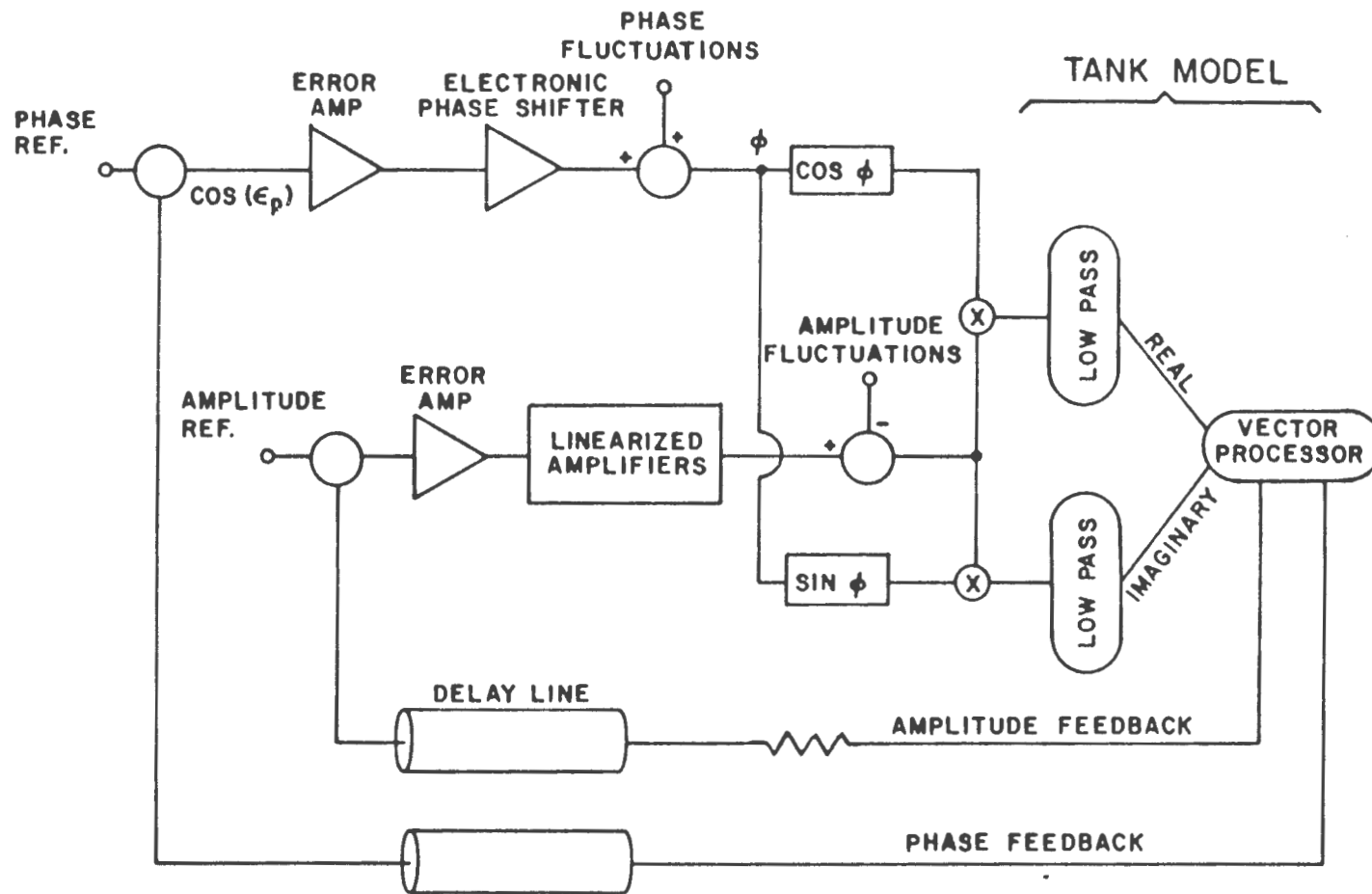


Figure 35

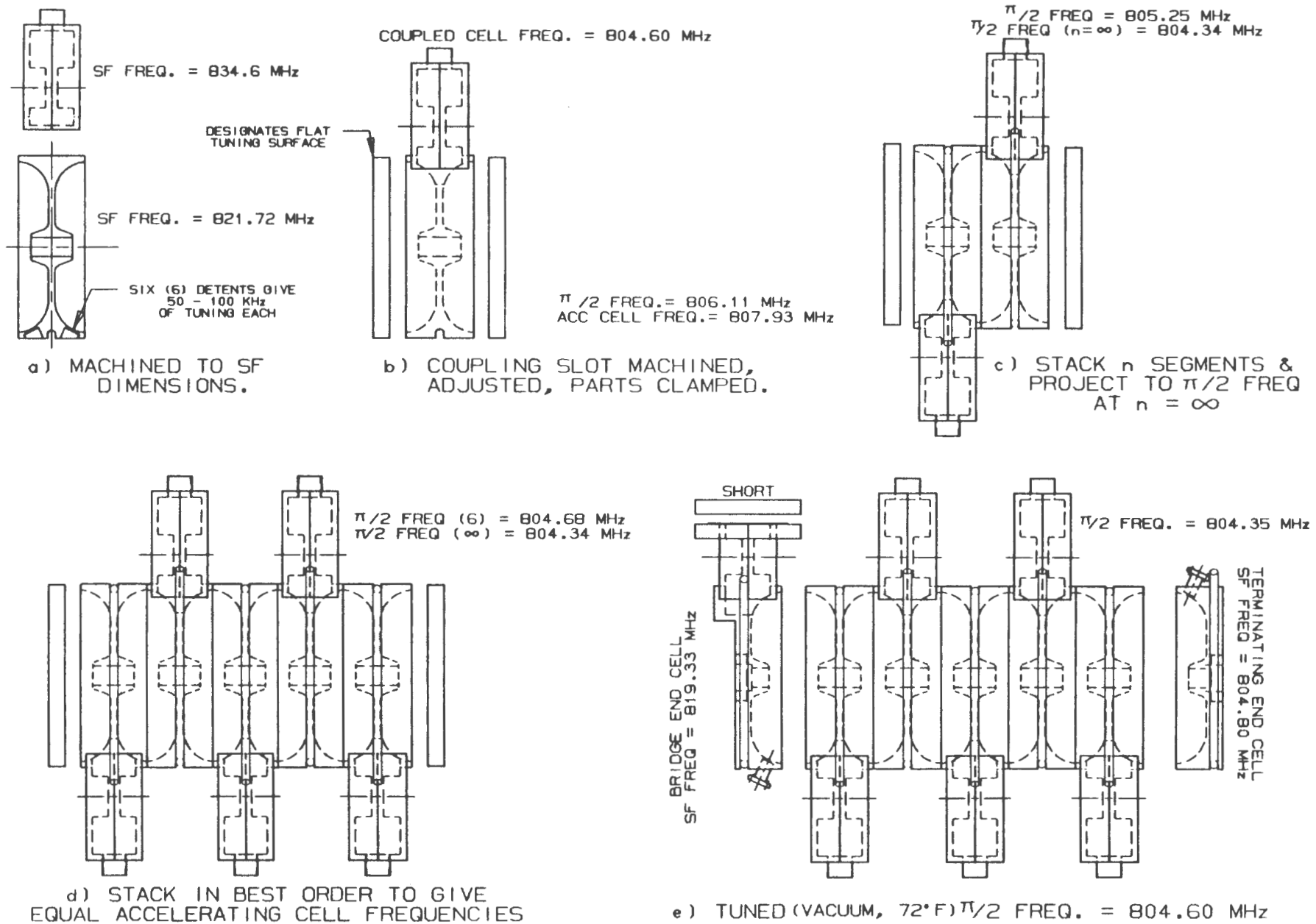
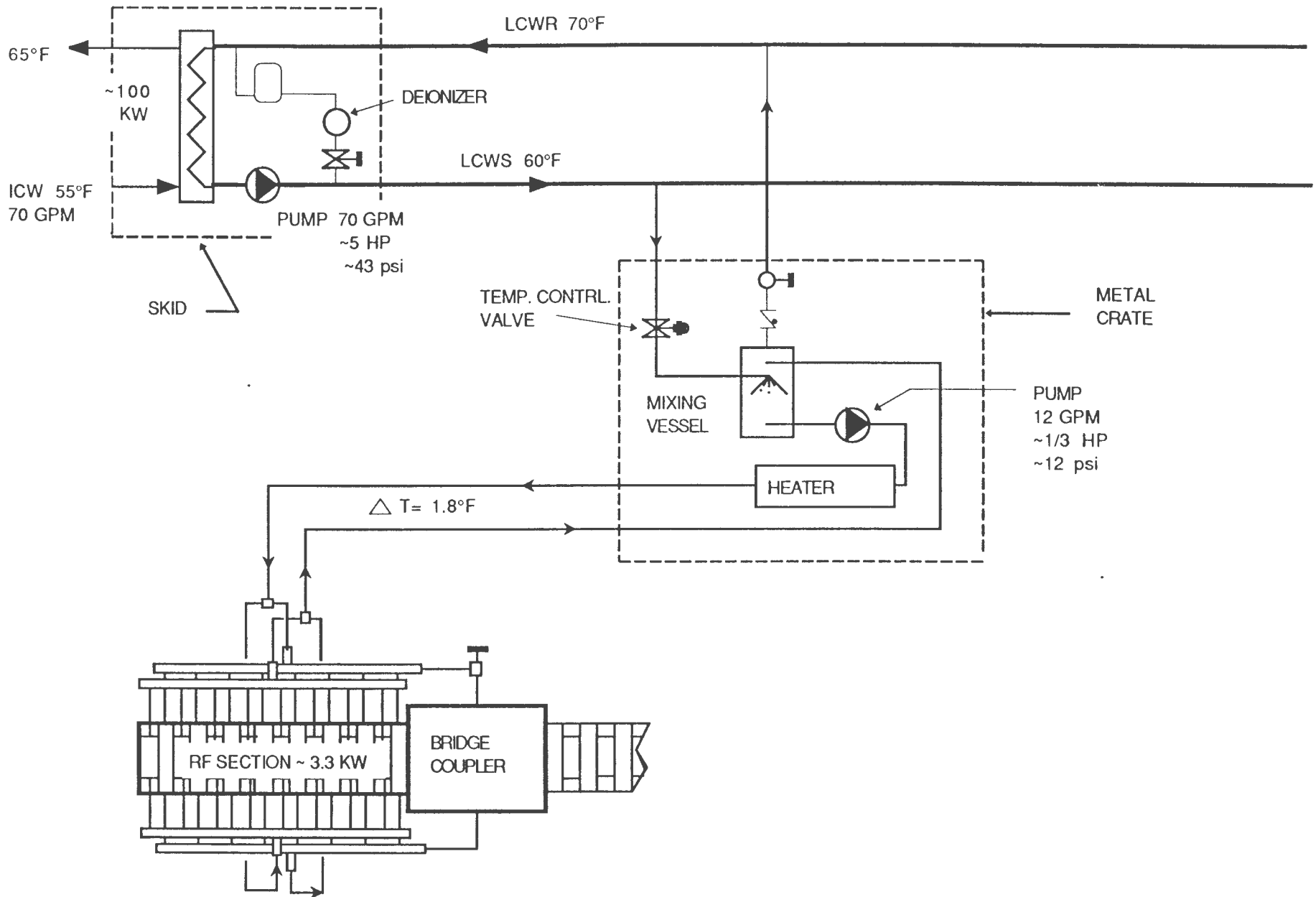


Figure 36



SIMPLIFIED SCHEMATIC OF A TYPICAL ONE SECTION CAVITY COOLING SYSTEM

Fig. 37

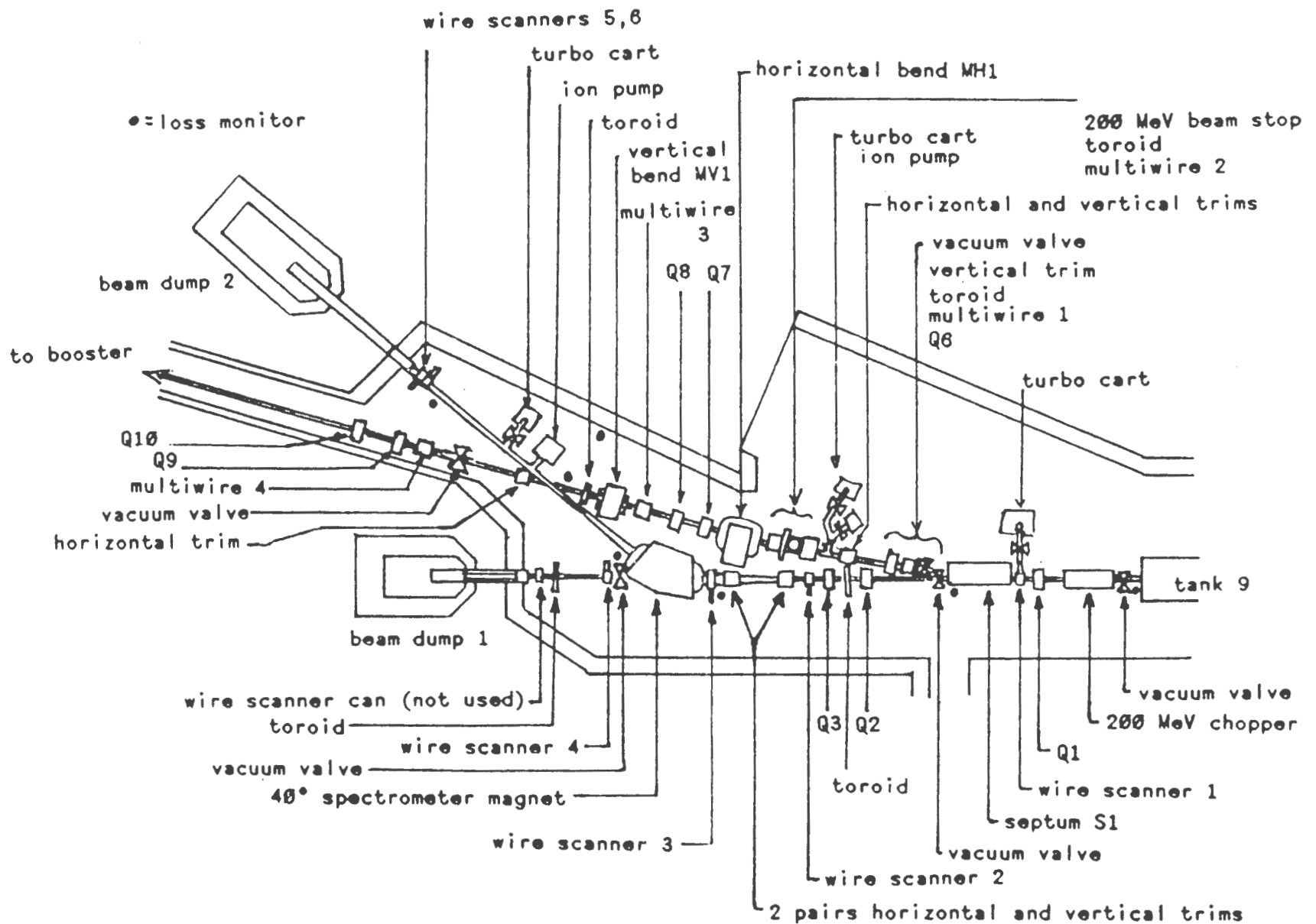


Figure 38 - Present 200 MeV area

Present 200 MeV Transfer Line to Booster
with elements to be modified in boxes,

200 MeV LINE

- H.F. QUAD
- ⊗ H.D. QUAD
- ◆ MULTIWIRE
- ⊗ VACUUM VALVE
- ⊙ TOROID
- L LOSS MONITOR

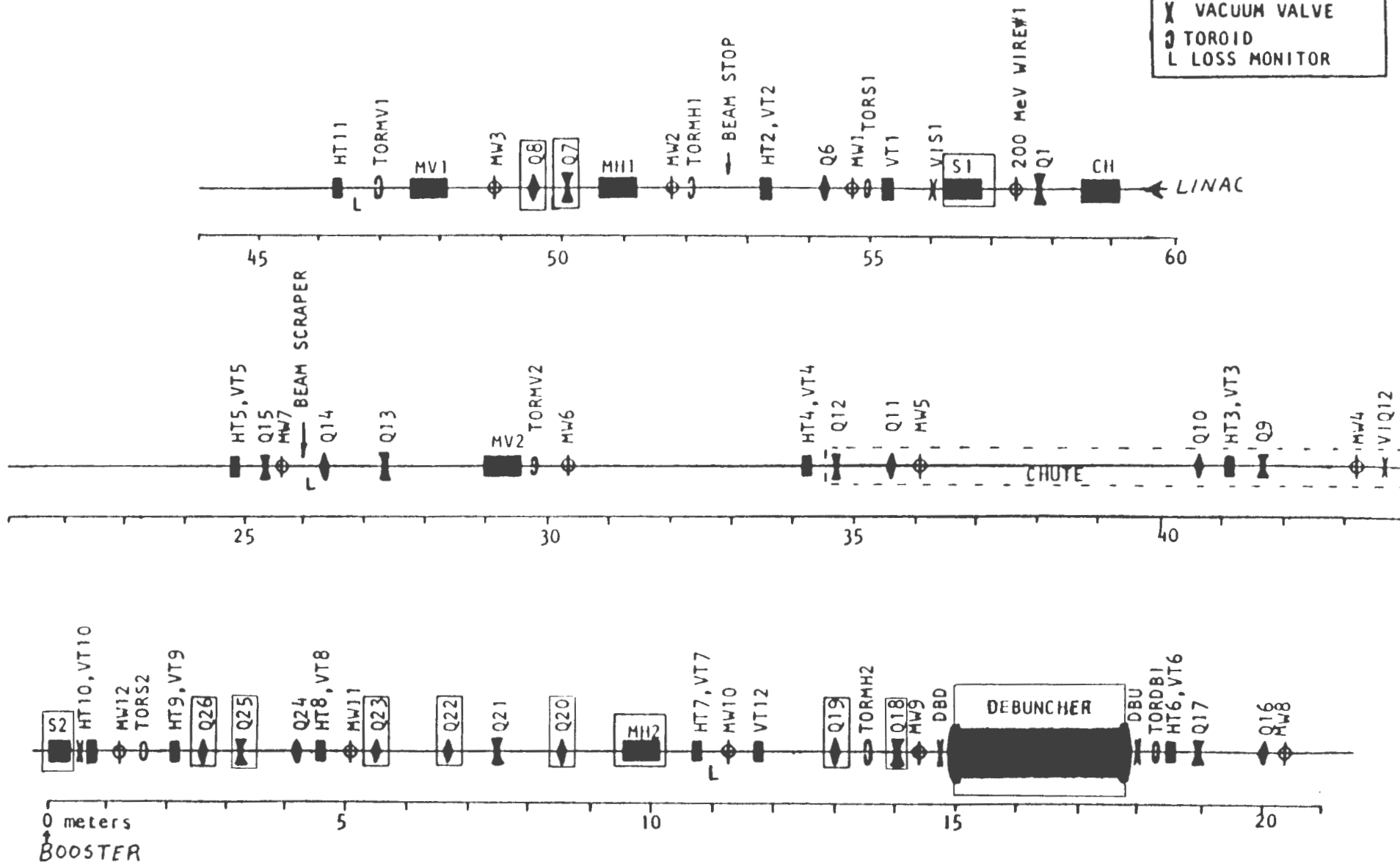
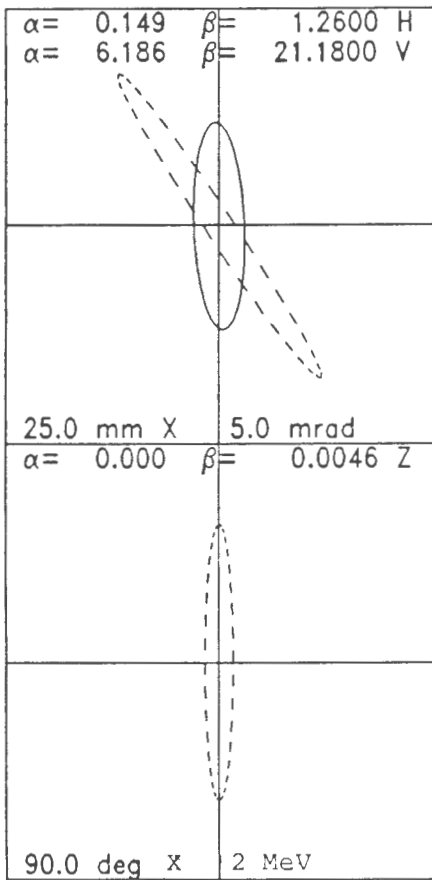


Figure 39

Debunching in 400 MeV Line 5-JUN-89 13:09:20



Beam Current= 200.0
 EMITI= 6.96 6.60 7450.00
 EMITO= 7.37 6.60 7747.33
 W= 401.500 401.500

 Phi= -90.0 deg, W=401.500 MeV
 DP= 62.3 deg, DW=124.401 keV
 DZ= 45.99 mm
 DP/P= 0.18 mrad
 EMITZ= 8.38 pi mm-mrad

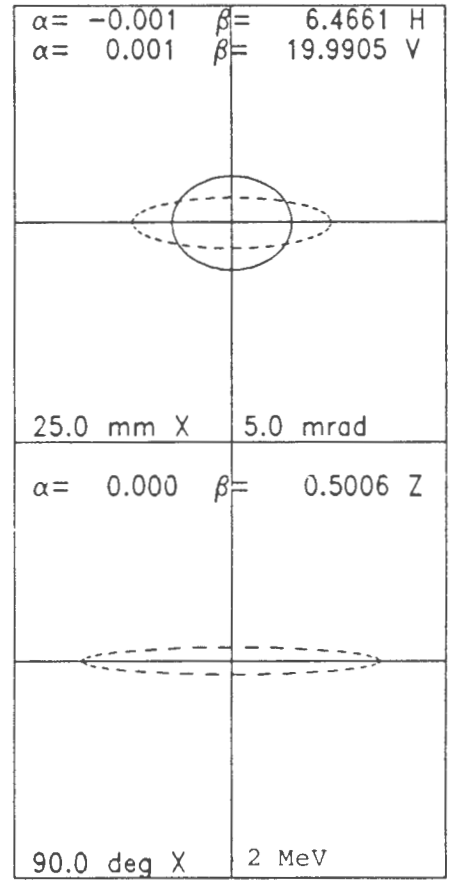


Figure 40

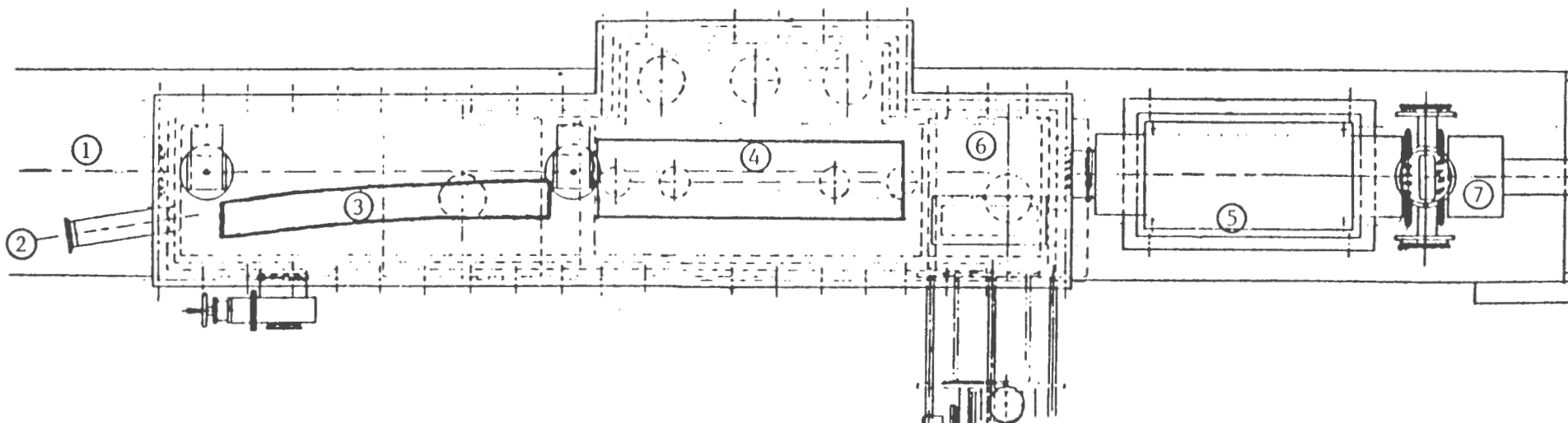


Figure 41 - The present H^- charge-exchange injection system in the Booster. The numbers in the figure correspond to:

- 1: Normal closed orbit
- 2: Incoming H^- beam
- 3: Current-sheet septum magnet
- 4,5: Orbit-bump magnets
- 6: Foil-changing mechanism
- 7: Beam position pickup and correction element package

DC SEPTUM MAGNET FIELDS

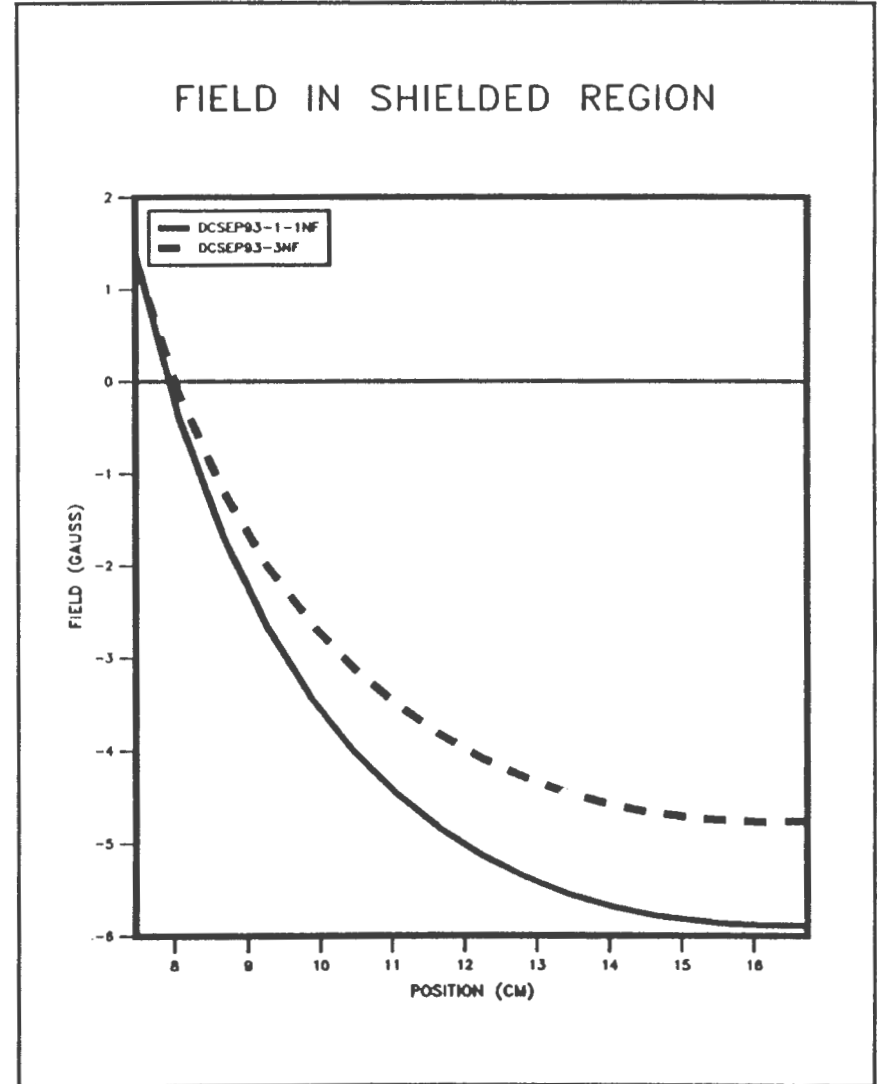
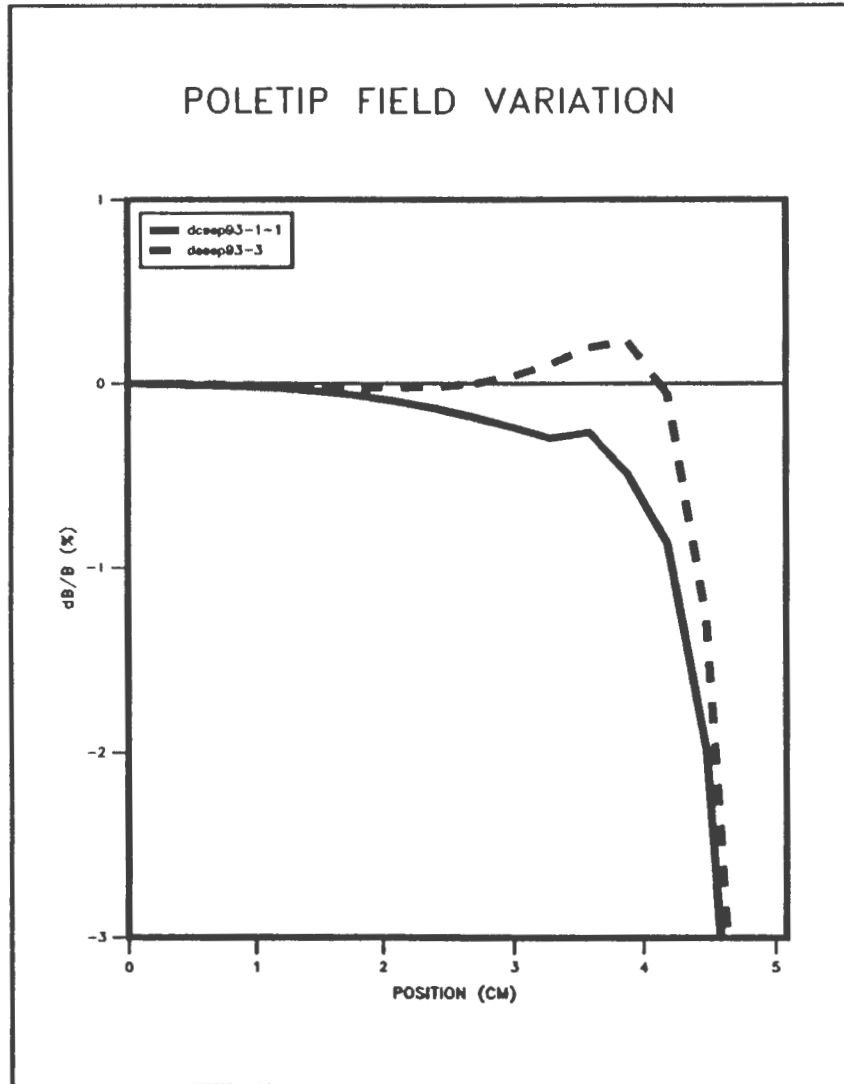


Figure 42

LONG STRAIGHT #1 INJECTION LAYOUT

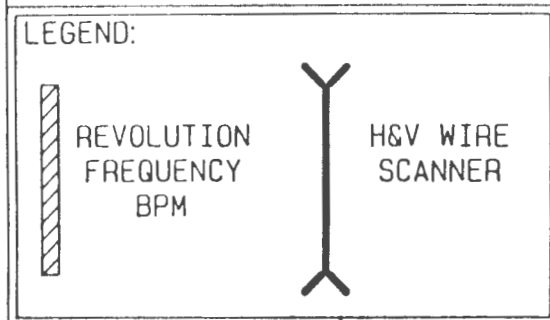
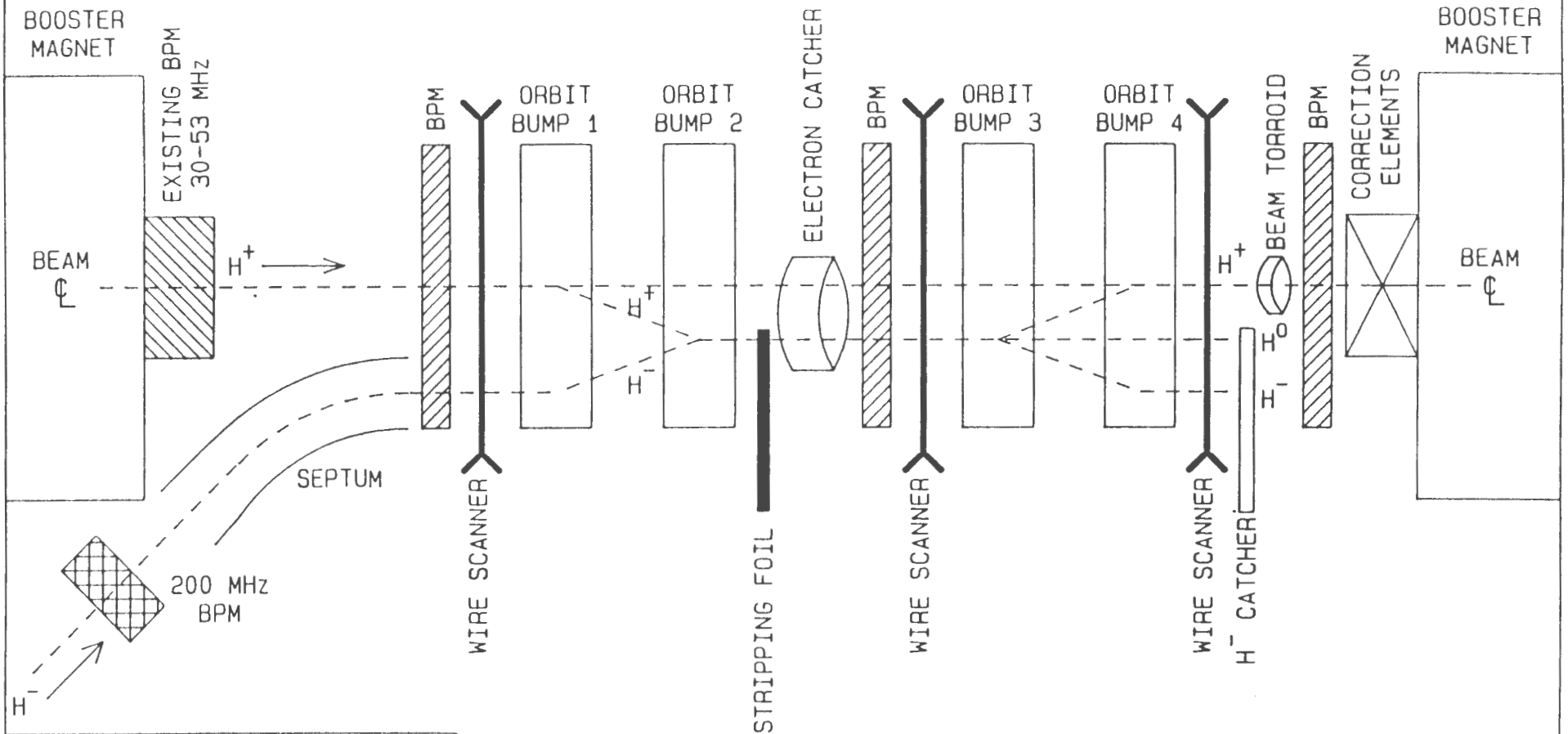


Figure 43

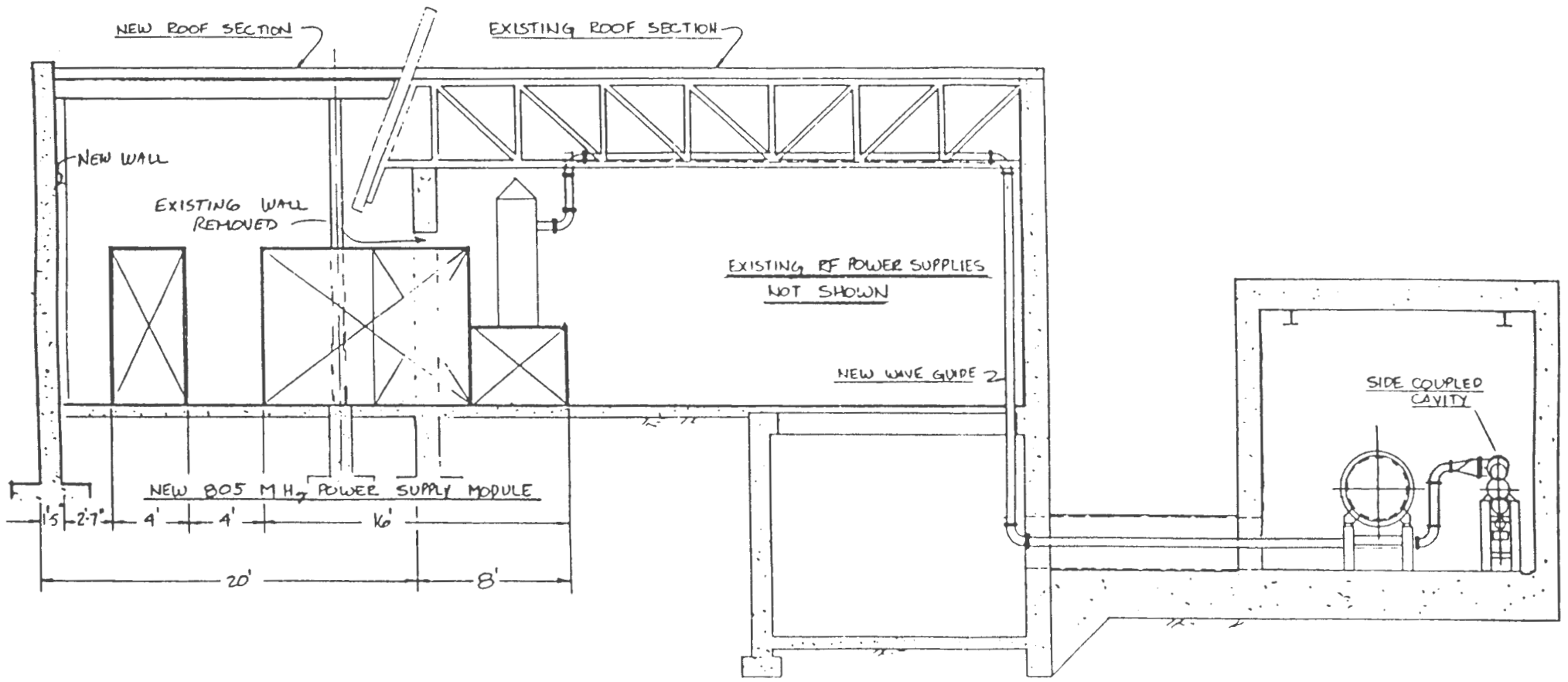


Figure 44

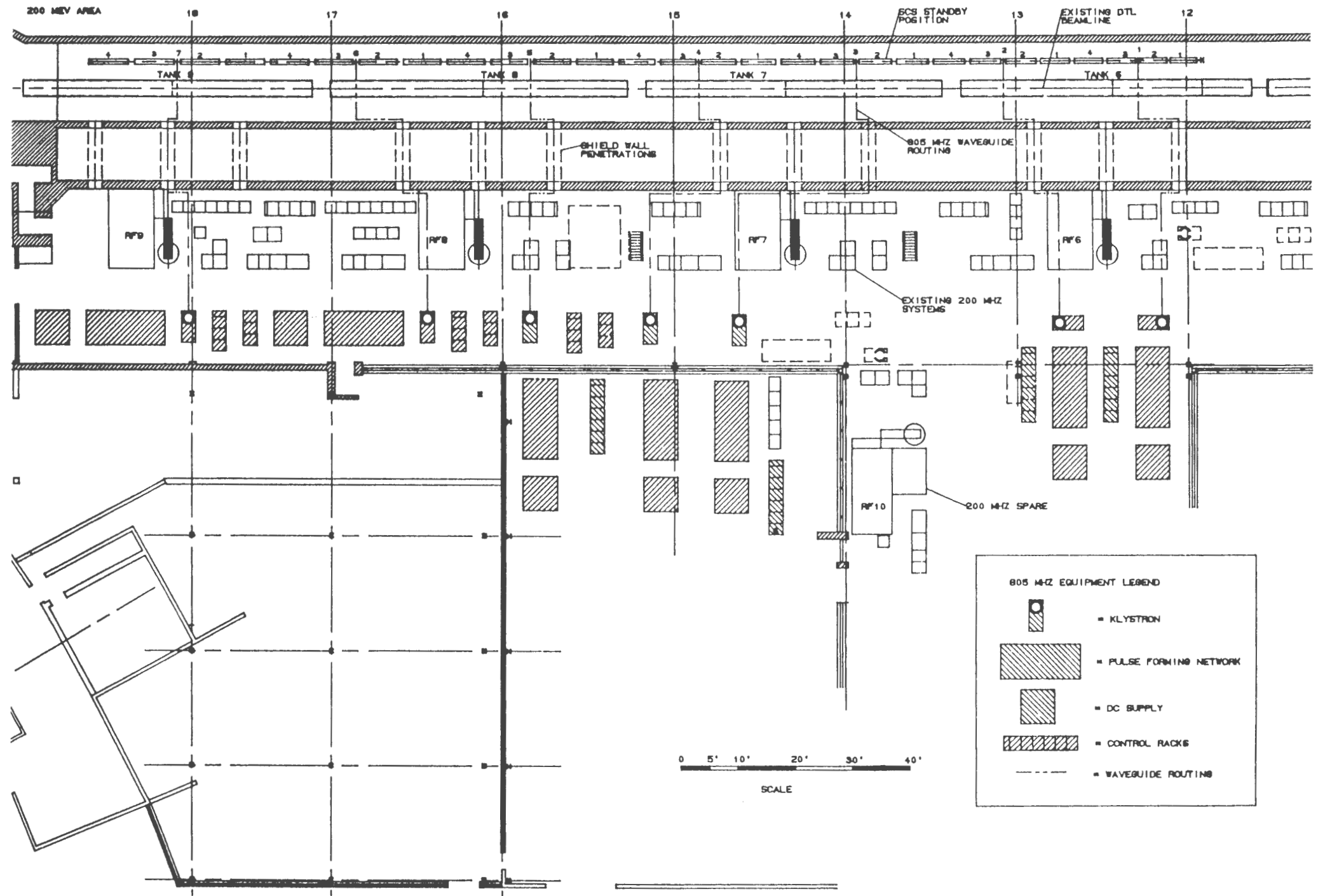


Figure 46

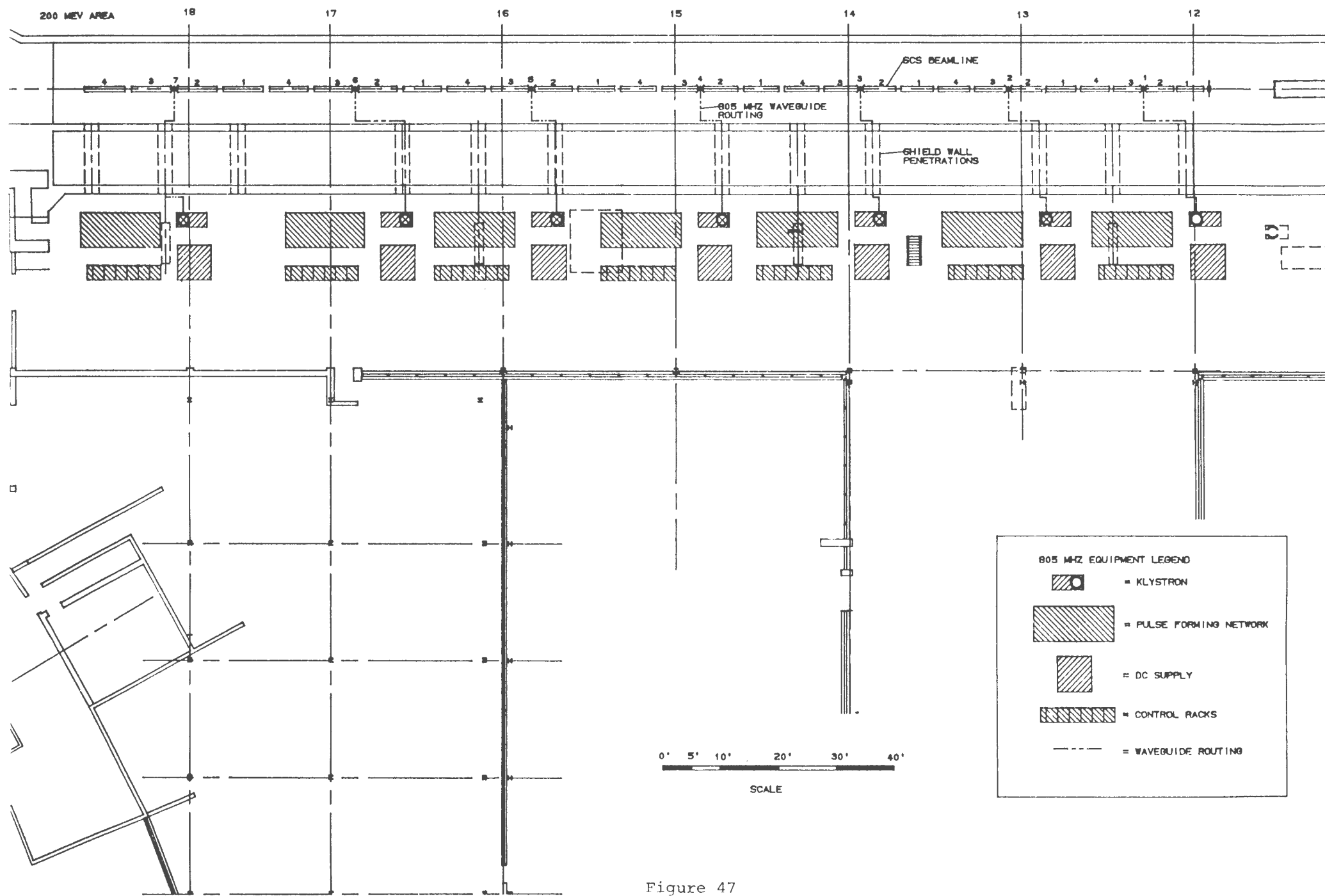


Figure 47